THE IDENTIFICATION AND DOWN SELECTION OF SUITABLE CATHODE MATERIALS FOR USE IN NEXT GENERATION THERMAL BATTERIES

Kyriakos Giagloglou

Supervised by Professor John T.S Irvine and Dr Paul A. Connor

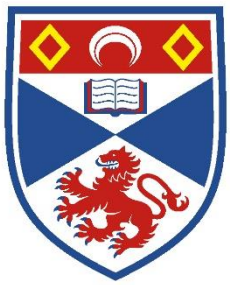

University of
St Andrews

This thesis is submitted in partial fulfilment for the degree of PhD

at the

University of St Andrews

March 2017

Declaration

1. Candidate's declarations:

I, Kyriakos Giagloglou hereby certify that this thesis, which is approximately 30000 words in length, has been written by me, and that it is the record of work carried out by me, or principally by myself in collaboration with others as acknowledged, and that it has not been submitted in any previous application for a higher degree.

I was admitted as a research student in [September, 2013] and as a candidate for the degree of PhD in [March, 2017]; the higher study for which this is a record was carried out in the University of St Andrews between [2013] and [2017].

(*If you received assistance in writing from anyone other than your supervisor/s*):

I, Kyriakos Giagloglou, received assistance in the writing of this thesis in respect of [language, grammar, spelling or syntax], which was provided by Dr Julia L. Payne

Date 27/03/2017 signature of candidate ……

2. Supervisor's declaration:

I hereby certify that the candidate has fulfilled the conditions of the Resolution and Regulations appropriate for the degree of PhD in the University of St Andrews and that the candidate is qualified to submit this thesis in application for that degree.

Date 27/03/2017 signature of supervisor ……

3. Permission for publication: (*to be signed by both candidate and supervisor*)

In submitting this thesis to the University of St Andrews I understand that I am giving permission for it to be made available for use in accordance with the regulations of the University Library for the time being in force, subject to any copyright vested in the work not being affected thereby. I also understand that the title and the abstract will be published, and that a copy of the work may be made and supplied to any bona fide library or research worker, that my thesis will be electronically accessible for personal or research use unless exempt by award of an embargo as requested below, and that the library has the right to migrate my thesis into new electronic forms as required to ensure continued access to the thesis. I have obtained any third-party copyright

permissions that may be required in order to allow such access and migration, or have requested the appropriate embargo below.

The following is an agreed request by candidate and supervisor regarding the publication of this thesis:

PRINTED COPY

a) No embargo on print copy
b) Embargo on all or part of print copy for a period of 1 year (maximum five) on the following ground(s):
    - Publication would be commercially damaging to the researcher, or to the supervisor, or the University
    - Publication would preclude future publication
    - Publication would be in breach of laws or ethics
c) Permanent or longer term embargo on all or part of print copy for a period of … years (the request will be referred to the Pro-Provost and permission will be granted only in exceptional circumstances).

Supporting statement for printed embargo request if greater than 2 years:

ELECTRONIC COPY

a) No embargo on electronic copy
b) Embargo on all or part of electronic copy for a period of 1 year (maximum five) on the following ground(s):
    - Publication would be commercially damaging to the researcher, or to the supervisor, or the University
    - Publication would preclude future publication
    - Publication would be in breach of law or ethics
c) Permanent or longer term embargo on all or part of electronic copy for a period of … years (the request will be referred to the Pro-Provost and permission will be granted only in exceptional circumstances).

Supporting statement for electronic embargo request if greater than 2 years:

ABSTRACT AND TITLE EMBARGOES

An embargo on the full text copy of your thesis in the electronic and printed formats will be granted automatically in the first instance. This embargo includes the abstract and title except that the title will be used in the graduation booklet.

If you have selected an embargo option indicate below if you wish to allow the thesis abstract and/or title to be published. If you do not complete the section below the title and abstract will remain embargoed along with the text of the thesis.

a) I agree to the title and abstract being published YES
b) I require an embargo on abstract NO
c) I require an embargo on title NO

Date 27/03/2017 signature of candidate …… signature of supervisor …….

Please note initial embargos can be requested for a maximum of five years. An embargo on a thesis submitted to the Faculty of Science or Medicine is rarely granted for more than two years in the first instance, without good justification. The Library will not lift an embargo before confirming with the student and supervisor that they do not intend to request a continuation. In the absence of an agreed response from both student and supervisor, the Head of School will be consulted. Please note that the total period of an embargo, including any continuation, is not expected to exceed ten years.

Where part of a thesis is to be embargoed, please specify the part and the reason.

Acknowledgments

I would like to thank my supervisors Professor John T.S Irvine and Dr Paul A. Connor for the opportunity to obtain a PhD within JTSI group in University of St Andrews, along with their supervision and guidance throughout my 3.5 years.

I would also like to take the opportunity to thank all my colleagues in JTSI group for their support, especially Dr Julia L. Payne for her patience and tuition.

Special thanks to Dr Richard K.B. Gover and Christina Crouch for their thoughts, discussions and suggestions.

Thanks to Ross Blackley for his help with Scanning Electron Microscopy and also to Dr Yuri Andreev and Mr Derek Waddell for their assistance with all my powder X-ray diffraction measurements.

Many thanks to the STFC for neutron diffraction beam-time and Dr. D. Fortes for his assistance on HRPD.

Finally, I would like to give thanks to AWE Plc. for funding of my PhD for 3.5 years.

Ευχαριστώ θερμά τους γονείς μου Θεοδώρα και Κωνσταντίνο, καθώς και τα αδέρφια μου Ευδοκία και Σάκη, για την υποστήριξη και συμπαράστασή τους σε όλες τις δύσκολες στιγμές των φοιτητικών μου χρόνων από το 2005 έως και σήμερα.

Abstract

In this work new novel cathode materials such as transition-metal sulfides, chlorides or fluorides were investigated and studied for their use in lithium ion thermal batteries. All cathodes were synthesized by a solid state reaction in sealed quartz tubes with a duration of firing for 1 week at high temperatures (> 500 °C).

All structures of compounds were probed by powder X-ray diffraction and the morphology and shape of crystallites of cathodes were characterized by scanning electron microscopy. The electrochemical properties of the batteries were investigated by galvanostatic discharge and galvanostatic intermittent titration technique at high temperatures (> 400 °C). All the batteries used as an anode $Li_{13}Si_4$, as an electrolyte LiCl-KCl eutectic and as separator MgO.

All the products of the discharge mechanism were confirmed using powder X-ray diffraction and EDX analysis.

$CoNi_2S_4$ and $NiCo_2S_4$ exhibit two voltage plateaux vs $Li_{13}Si_4$ at 500 °C, one at around 1.75 V and the second at 1.50 V. Capacities of 350 and 290 mA h g^{-1} were achieved, respectively. NiS, Co_3S_4 and Co_9S_8 were confirmed as the products of discharge mechanism.

ZrS_3 exhibits a single flat voltage plateau of 1.70 V at a current density of 11 mA/cm^2 and a capacity of 357 mA h g^{-1}, at 500 °C was obtained. A new material, $LiZr_2S_4$, was identified as the product of the electrochemical process, which can be indexed to a = 10.452(8) Å cubic unit cell.

$KNiCl_3$ was tested at different current densities from 15 mA/cm^2 to 75 mA/cm^2 and a high cell voltage, with a capacity of 262 mA h g^{-1} was achieved at 425 °C. Ni metal, KCl and LiCl were confirmed as the products of the discharge mechanism.

Li_2MnCl_4 was tested at the same current densities as $KNiCl_3$ at 400 °C and a capacity of 254 mA h g^{-1} was achieved. Mn metal and LiCl were confirmed as the products after discharge.

Li_6VCl_8 has a capacity of 145 mA h g^{-1} and a flat voltage plateau of 1.80 V at 500 °C.

$NiCl_2$ has also a capacity of 360 mA h g^{-1} and a high voltage profile of 2.25 V at 500 °C.

$CoCl_2$ exhibits a lower capacity of 332 mA h g^{-1} and lower voltage profile compared to $NiCl_2$ at 500 °C. CuF_2 and PbF_2 were tested at 500 °C. PbF_2 exhibits a single flat voltage plateau of 1.25 V and a capacity of 260 mA h g^{-1} was obtained. CuF_2 has a high voltage profile but a voltage plateau could not be obtained.

Table of Contents

List of Abbreviations

EDX	Energy Dispersive X-ray Spectroscopy
GITT	Galvanostatic Intermittent Titration Technique
GSAS	General Structure Analysis System
HRPD	High Resolution Powder Diffractometer
LAN	Liquid Anode
PXRD	Powder X-ray Diffraction
SEM	Scanning Electron Microscopy
VTXRD	Variable Temperature powder X-ray Diffraction

List of Figures

List of Tables

Chapter 1: Introduction

Chapter 1: Introduction

1.1 What is a Lithium ion Battery and why is it useful?

In the 20th century, the main power source was the combustion engine because of its high energy and power densities. Today the rate of global warming and the limited oil supply require a sustainable alternative.

Moreover, the human society and technology progress in electric vehicles, medical equipment, military applications and space technology require power systems with high energy, safety and long shelf – life characteristics. However, the energy conversion and the ability to store huge quantities of electrical energy, which are derived from wind, photovoltaics, fuel cells and engines, is one of the most important social challenges.

There are different kinds of power systems such as supercapacitors, fuel cells and batteries for this goal. Supercapacitors have a low specific energy but the highest specific power. The difference between fuel cells and batteries derives from the fact that fuel cells require a fuel from an outside source, while the batteries do not. However, fuel cells have a higher specific energy than other electrochemical conversion energy devices. Batteries have specific energy and power in a range between supercapacitors and fuel cells. Lastly, batteries provide a higher energy density than supercapacitors or ultracapacitors. However, supercapacitors provide higher power density and longer cyclic life than batteries [1, 2].

Since the SONY Corporation developed a rechargeable lithium - ion battery in 1990, the batteries have been used as power sources in a wide range of applications. Nowadays, batteries are part of our everyday life as they generate power for laptops, mobile phones, electric cars, cameras etc.

Batteries are electrochemical devices that offer a direct conversion of chemical energy to electrical energy by an electrochemical oxidation – reduction reaction as presented in Figure 1.1. During this electrochemical reaction the anode or else, the negative electrode, is oxidized and electrons flow to the external circuit. The cathode or

else, the positive electrode, is reduced and accepts electrons from the external circuit. Between these electrodes there is a high ionic conductor, which is called electrolyte, and provides the motivation of ions from the anode to the cathode. Another part of the battery is also the separator, which used to avoid the physical contact of the anode and the cathode electrode. Batteries need to be sealed to prevent leakage and dry-out.

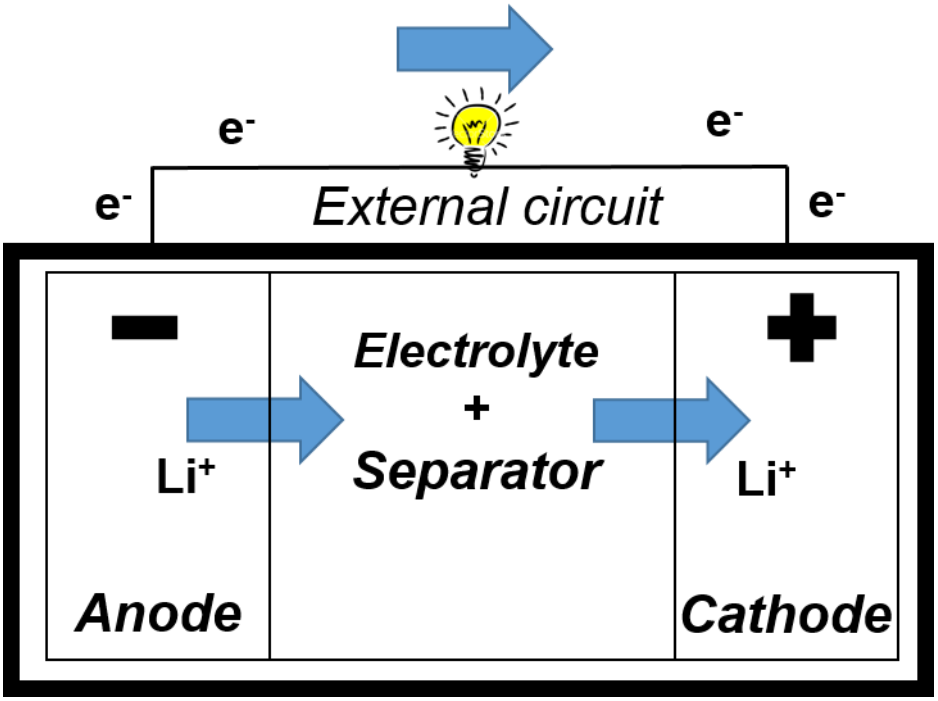

Figure 1.1. A simple illustration of a primary battery. Blue arrows represent the moving of lithium ions during the discharge process

The force that causes the electrons to flow from the anode to the cathode is the difference in the potential energy of the electrons at the anode compared to the one at the cathode. In other words, the potential energy of the electrons is higher at the anode than the one at the cathode. This potential difference is measured in Volts (V) and is called the cell voltage [3]. The theoretical standard cell voltage can be defined by using E^o values as:

$$E^o\,(\text{cathode}) - E^o\,(\text{anode}) = E^o\,(\text{cell}) \quad [1.1]$$

This standard theoretical cell voltage is modified by the Nernst equation [4] which relates the reduction potential of an electrochemical reaction (half - cell or full cell reaction) to the standard electrode potential of the chemical species undergoing reduction and oxidation. It is the most important equation in the field of electrochemistry.

The actual cell voltage will often be lower than the theoretical cell voltage due to the polarisation and the cell resistance losses (IR drop) of the battery and is dependent upon the applied current density. These factors are dependent upon electrode kinetics and thus, vary with temperature, state of cycling, and with the age of the battery. Moreover, the IR drop is a result of the change of internal resistance, including the resistance of the electrolyte, electrode materials, and other connectors or auxiliaries. The cell resistance (IR drop) can be decreased by the use of a conductive coating on the surface of the electrode materials [5]. The actual cell voltage needs to be sufficient for the intended application. Typical values of cell voltage range from 1.2 V for a Ni/Cd battery to 4.0 V for a Li ion battery.

There are two types of batteries, primary and secondary. Primary batteries cannot be recharged electrically and are discharged once and discarded. They are only for one use because the electrochemical reaction which occurs in primary batteries is not reversible. Primary batteries have a shelf - life 3 to 5 years.

Secondary batteries can be recharged electrically to their initial condition once they are discharged by passing current in the opposite direction. During discharge process, the ions from the anode pass through the electrolyte and are intercalated into the crystallographic structure of the cathode. As the electrochemical reaction is reversible, the opposite movement of ions takes place during charge process. Secondary batteries have a shelf – life of more years than primary batteries but it depends on their use.

1.1.1 **Characteristics of Lithium ion Battery**

Some characteristics of a lithium ion battery are the discharge curve, the capacity, the energy density, the power density and the operation temperature.

The discharge curve is a plot of cell voltage against time or capacity. A single flat voltage profile is desirable, because this means that the cell voltage remains constant as the battery is discharged. The cell voltage of a lithium ion battery is directly proportional to the reduction of Gibbs free energy when lithium ions are inserted into the cathode electrode, during the discharge process [6, 7].

Capacity of a lithium ion battery is the quantity of electricity involved in the electrochemical reaction between anode and cathode electrode. Capacity is given by Faraday's Law [8] as

$$\text{Capacity} = e^- * F * n \quad [1.2]$$

Where n = number of moles involved in the electrochemical reaction, e^- = number of electrons involved in the electrochemical reaction, F = Faraday's constant (1 mole of electrons, F = 96487 Coulombs) and is measured in units of Ampere - hours per gram (A h g^{-1}) or (mA h g^{-1}). The capacity in a lithium ion battery depends on (i) the capability of the electrodes to change the oxidation states, (ii) the capability of the electrodes to accommodate the lithium ions, and (iii) the reversibility of the electrochemical reactions [6, 7]. For example, the metal lithium and the lithium silicon alloy $Li_{22}Si_4$ anodes exhibit a theoretical capacity of 3850 and 4200 mA h g^{-1}, respectively [9, 10]. In the case of $LiCoO_2$ cathode, the theoretical capacity is 273 mA h g^{-1} if one Li ion is inserted into the host lattice. However, the experimental capacity is only 140 mA h g^{-1} as half of the Li ions can be reversibly inserted into or extracted from the $LiCoO_2$ host [11].

The energy density of a battery is a measure of how much energy the battery can store in a given size or mass and its units are (Wh/kg). This energy density is limited by the capacity of the battery and the cell voltage [12, 13].

Power density is a measure of how quickly the battery can deliver energy and its units are (W/kg). The power density of a battery can be improved by nanostructured

electrode materials, which have a large specific surface area and a short solid-state transport distance [14, 15].

The operation temperature of a lithium ion battery affects the internal resistance. For example, very low temperatures cause higher internal resistance; then, the electrolyte may freeze causing a lower cell voltage as ions are transferred more difficult. However, at very high temperatures the chemical components may decompose, or there may be enough thermal energy available to activate unwanted, reversible reactions, reducing the capacity of the battery.

1.1.2 **Types of Electrochemical Reactions in a Lithium ion Battery**

There are two different kinds of reaction that can take place in a lithium ion battery. These reactions can be an intercalation reaction or a conversion reaction. An intercalation reaction takes place in lithium ion batteries when the positive electrode is a solid host network that can store guest lithium ions. The lithium ions can be inserted into the structure, or can be removed from, during discharge and charge process. In a lithium ion battery, the guest ions are Li^+ and the host network compounds are metal chalcogenides, transition metal oxides, or poly-anion compounds. These compounds can be divided into several crystal structures, such as layered, spinel, olivine etc. The layered structure is the most known structure of intercalation compounds for use as cathode materials in lithium ion batteries. However, the most current research is focused on the spinel and olivine structures as these structures exhibit higher operating voltage and higher energy storage capability than the layered structure [16]. The most commercially used transition metal oxide is $LiCoO_2$, introduced by Goodenough and forms a layered structure [17]. $LiCoO_2$ is a very attractive intercalation cathode material until now, because it has a high theoretical specific capacity of 274 mA h g^{-1}, a low self-discharge, a high discharge voltage, and a good cycling performance [18, 19]. However, $LiCoO_2$ is expensive because of the high cost of Co. Another, intercalation cathode material (layered structure) is $LiNiO_2$ and is cheaper than $LiCoO_2$. $LiNiO_2$ has similar electrochemical properties with $LiCoO_2$ but is unattractive, because the Ni ions have a

tendency to occupy the lithium ion sites during the synthesis, or delithiation, and as a result they block the Li diffusion pathways [20]. $LiNiO_2$ is also less thermally stable than $LiCoO_2$, because Ni ions are more easily reduced than Co ions [21]. $LiMnO_2$ can also replace $LiCoO_2$ and $LiNiO_2$, because Mn is much cheaper and less toxic than Co and Ni [22]. However, the performance of $LiMnO_2$ needs to be improved because the layered structure has a tendency to change into spinel structure during lithium ion extraction [23]. $LiFePO_4$ and $LiMnPO_4$ are the most known materials for the olivine structure and exhibit good thermal stability and high power capability [24, 25]. The major disadvantage of the $LiFePO_4$ is the low electrical and ionic conductivity. Usually, the intercalation cathode materials exhibit capacities of 100 to 200 mA h g^{-1} and voltages 3 to 5 V vs. Li/Li^+.

A conversion reaction takes place in a lithium ion battery, when the cathode material undergoes a solid-state redox reaction during lithiation, or delithiation, in which the crystalline structure changes and is accompanied by the breaking and recombining of chemical bonds [16]. A single flat and long voltage plateau indicates good kinetics of the reaction between two solid phases. There are two types (Type 1 and 2) of a conversion reaction as presented:

$$\text{(Type 1) } MA_x + yLi \Rightarrow M + {}_xLi_{y/x}A \quad [1.3]$$

and

$$\text{(Type 2) } A + yLi \Rightarrow Li_yA \quad [1.4]$$

For example, Type 1 conversion reaction takes place for the FeF_2 and Type 2 conversion reaction takes place for sulfur (Li_2S). In the case of FeF_2, the fluorine ions have the higher mobility so they diffuse out of the FeF_2. LiF and Fe nanosized phases are formed [26]. Moreover, Type 1 conversion cathode materials form metal nanoparticles at their fully lithiated state. Sulfur was studied because it exhibits a high theoretical specific capacity (1675 mA h g^{-1}) and is cheap. In the conversion reaction of sulfur there are polysulfides, which are soluble in organic electrolytes [27]. Transition-metal fluoride and chloride compounds have recently been investigated due to their intermediate

operating voltages and their high theoretical specific or volumetric capacities. However, these compounds generally suffer from a poor conductivity, a large voltage hysteresis, a volume expansion, unwanted side reactions, and a dissolution of active material [16]. For example, FeF_3 and FeF_2 exhibit a poor electronic conductivity because of their large band gap induced by the highly ionic character of the metal-halogen bond. However, their structures can support a good ionic conduction [28, 29]. Transition-metal chlorides exhibit also a poor electronic conductivity for the same reason [30].

1.1.3 **Factors affecting the electrochemical properties of a Lithium ion Battery**

In general, there are some factors which affect the electrochemical properties (e.g. cell voltage) of the battery, such as the electronegativity of chemical elements, the structure of the electrodes and the electronic structure of the compounds [31].

It is known that chemical elements with a large atomic number and a large electronegativity lead to a high cell voltage [32]. Electronegativity describes the tendency of an atom to attract a bonding pair of electrons. The electronegativity increases as the atomic number increases in the same row on the periodic table. Different values of electronegativity determine the character of chemical bonds, which are formed between transition-metal ions and anions. Large differences in electronegativity between chemical elements lead to ionic bonds and small differences in electronegativity between chemical elements to covalent bonds. Compounds with ionic bonds are formed in denser structures than compounds with covalent bonds.

This structure density affects the specific site energy of lithium ions and this site energy affects the electrochemical properties of electrodes [31]. This site energy of lithium ions is the main factor of the Gibbs free energy. The Gibbs free energy describes the equilibrium voltage of the electrodes in lithium ion batteries. Moreover, the site energy is the contribution of the enthalpy change (H) to the process of lithium ion intercalation (dH/dn) [33].

For example, if the site energy in a crystal lattice is low then the external energy, which is consumed to transfer one lithium ion from the occupied site to a free site is high. Different positions in a crystal lattice exhibit different site energies and produce different voltages when lithium ions are inserted into, or extracted from, host electrodes.

The crystal structure of the electrodes affect the electrochemical properties of a lithium ion battery. The crystal structure describes the unique arrangement of the atoms in a crystal which minimises the total energy. The size of the structure can be divided into microstructure and nanostructure. The electrochemical properties of a lithium ion battery change as the size of the structure gets smaller. More specifically, nanostructured electrode materials, the smallest possible crystal structure, enhance these electrochemical properties. This happens because the reversibility of the lithium ions insertion and extraction reaction in nanostructured electrodes takes place without destroying the crystal structure. The reduced particle size affects also the path of lithium ion transfer and increases the rate capability [34]. Small-sized particles have a large specific surface area and therefore a high surface energy.

In addition, the use of defects and disorder of atomic arrangement in the crystal can also affect the cell voltage. Defects change the site energy and can be introduced through doping and control of conditions of the synthesis [35 - 37].

Moreover, electrodes with polyanionic groups, such as phosphates, silicates and sulfates, exhibit higher cell voltage than transition-metal oxides which contain lithium ions. For example, $LiCoPO_4$ exhibits a high voltage of 4.8 V compared to $LiCoO_2$ which exhibits a voltage of 4 V [38].

The electronic structure of electrode materials is one of the factors that affects the electrochemical properties of a lithium ion battery. For example, the atomic numbers of Mn and Fe are 25 and 26, respectively. Fe is more electronegative than Mn and attracts electrons more strongly than Mn. The energy state of the available electrons is also higher in Fe^{2+} than the one in Mn^{2+}. However, $LiMnPO_4$ exhibits a higher voltage of 4.13 V [39] compared to that one of $LiFePO_4$ of 3.43 V [40]. Both compounds are formed in the same crystal structure, as all the lithium ions occupy octahedral sites and are bonded

with six transition metal ions. The difference is that the Fe^{2+} ($3d^6$) requires the electron pairing energy to insert the sixth electron in the t_{2g} orbital and the Mn^{2+} ($3d^5$) does not [41]. This provides more energy that could be released or be consumed, in the electrochemical process of Mn phosphate [42, 43].

In general, during the electrochemical process, the lithium ions occupy the space between layers or the octahedral or tetrahedral sites in the host crystal. At the same time, an equal number of electrons occupy the free *d* orbitals of the transition-metal cations in the host crystal [31]. Moreover, if the energy, which is realised when the electrons are inserted into or extracted from *d* orbitals, is high then the cell voltage is high as well. In addition, the cell voltage of a battery increases as the number of electrons in *d* orbitals of the transition-metal elements of the same period in the periodic table increases. As a result, the cell voltage of a battery is directly correlated with the energy, which is required to add or remove lithium ions and to reduce or oxidize the transition-metal cations in the host crystal.

1.2 **Room temperature and high temperature (thermal) Lithium ion Battery**

Room temperature lithium ion batteries use liquid or polymer gels electrolytes, which are ionically conductive at room temperature and they have self-discharge issues during storage because of the transport of charged species through the electrolyte. Self - discharge decreases the available capacity of the batteries.

This practical problem is solved by using high-temperature lithium ion batteries. Thermal batteries are primary batteries and use molten salt electrolytes (in the separator between the anode and the cathode), which are solid and non – conductive at room temperature. These electrolytes are only ionically conductive when molten and the batteries remain active while the electrolyte stays molten. The electrolytes which are used typically melt > 300 °C. The electrodes (anode and cathode) and separator material remain solid during the operation of the battery.

This advantage of the frozen electrolyte, provides stable energy storage for decades [44]. The elevated temperature also enhances the electrochemical kinetics in order to provide higher power as they can be discharged at higher currents than the room temperature batteries. For example, the molten salt LiCl – KCl eutectic electrolyte has a value of ionic conductivity of 1850 mS cm^{-1} at 500 °C. Thermal batteries provide specific power of 8000 W kg^{-1} compared to room temperature batteries, for example, Ni/Cd battery, (175 W kg^{-1}) or Li-ion battery, (340 W kg^{-1}) [44, 45].

Thermal batteries, as all batteries, are hermetically sealed and can be stored for more than 25 years over a wide range of storage temperatures (typically, − 55 to + 75 °C) without degradation [44].

The most common applications of thermal batteries are those that need a long shelf-life and an instant high power like emergency power systems, such as in pilot ejector seats and sonobuoys.

1.3 **History of Lithium ion Thermal Battery**

The first time that thermal batteries were designed was by German scientists during World War II for V2 rockets as a military application; there, the electrolyte was melted by the rocket exhaust heat in the mission [46]. After World War II, the technology that was used was under the investigation of the United States in 1946. In 1947, Catalyst Research Corp. investigated different kinds of electrolytes and finally, chose the LiCl-KCl eutectic. In 1954, Eagle Picher Technologies, which is the largest US manufacturer of thermal batteries until now, and Sandia National Laboratories, started to develop thermal batteries for the Atomic Energy Commission [44].

The early technology of thermal batteries, the so-called 'cup and cover technology', used the molten salt electrolyte LiCl-KCl eutectic with a glass tape as separator material in a metal cup. The heat source was a mixture of $BaCrO_4$ and Zr powder; however, this material was very dangerous as it was sensitive to shock.

The later technology, the so-called 'pellet technology', used a powdered kaolin clay to immobilize the electrolyte [47]. Nowadays, ceramic materials are used as separators [48] and thermal batteries include a pyrotechnic material such as Fe-$KClO_4$ instead of the chromate, which is much safer.

In Chapter 2, there is more discussion and description about the history of the materials that have been used in lithium ion thermal batteries until these days.

1.4 **References**

[1] P. Simon *et al.*, *Science,* 343, (6176) (2014), 1210

[2] H.D. Abruna *et al*., *Physics Today*, 61, (12) (2008), 43

[3]http://www.mikeblaber.org/oldwine/chm1046/notes/Electro/CellEMF/CellEMF.htm

[4] Mary Virginia Orna *et al.*, *Electrochemistry past and present*, American Chemical Society, Columbus, Ohio, (1989)

[5] L. Su *et al.*, *Nanoscale*, 3, (10) (2011), 3967

[6] J.K. Park, *Principles and Applications of Lithium Secondary Batteries*, Wiley-VCH, Germany, (2012)

[7] M.S. Islam *et al.*, *Journal of Chemical Society Reviews,* 43, (1) (2014), 185

[8] Ehl Rosemary Gene *et al.*, *Journal of Chemical Education*, 31, (1954), 226-232

[9] M.N. Obrovac *et al*., *Chemical Reviews,* 114, (23) (2014), 11444

[10] B. Liang *et al.*, *Journal of Power Sources,* 267, (2014), 469

[11] S. Luo *et al.*, *Advanced Materials,* 24, (17) (2012), 2294

[12] D. Li *et al.*, *Materials Today,* 17, (9) (2014), 451

[13] A. Van der Ven *et al.*, *Accounts Chemical Research*, 46, (5) (2013), 1216

[14] R. Mukherjee *et al.*, *Nano Energy*, 1, (4) (2012), 518

[15] P. Roy *et al.*, *Journal of Materials Chemistry A,* 3, (6) (2015), 2454

[16] Naoki Nitta *et al.*, *Materials Today*, 18, (5) (2015), 252

[17] K. Mizushima *et al.*, *Materials Research Bulletin*, 15, (6) (1980), 783

[18] R. Yazami *et al.*, *Proceedings of the International Symposium*, The Electrochemical Society, 2003, (2003), 317

[19] A. Du Pasquier *et al.*, *Journal of Power Sources,* 115, (1) (2003), 171

[20] A. Rougier *et al.*, *Journal of the Electrochemical Society,* 143, (4) (1996), 1168

[21] H. Arai *et al.*, *Solid State Ionics*, 109, (3) (1998), 295

[22] A.R. Armstrong *et al.*, *Nature*, 381, (6582) (1996), 499

[23] M. Gu *et al.*, *ACS Nano,* 7, (1) (2012), 760

[24] D. Doughty *et al.*, *The Electrochemical Society Interface*, 21, (2) (2012), 35

[25] C. Delacourt *et al.*, *Journal of the Electrochemical Society,* 152, (5) (2005), A913

[26] F. Wang *et al.*, *Journal of the American Chemical Society,* 133, (46) (2011), 18828

[27] M.Q. Zhao *et al.*, *Nature Communications,* 5 (2014), 3410

[28] F. Badway *et al.*, *Journal of the Electrochemical Society,* 150, (10) (2003), A1318

[29] Y. Zheng *et al.*, *Solid State Communications,* 152, (17) (2012), 1703

[30] H.C. Yu *et al.*, *Energy Environmental Science*, 7, (5) (2014), 1760

[31] Chaofeng Liu *et al.*, *Materials Today*, 19, (2) (2016), 109

[32] B.C. Melot *et al.*, *Accounts Chemical Research*, 46, (5) (2013), 1226

[33] R. Yazami, *Nanomaterials for Lithium-Ion Batteries: Fundamentals and Applications*, CRC Press, Taylor & Francis Group, (2013)

[34] P.G. Bruce *et al.*, *Angewandte Chemie International Edition,* 47, (16) (2008), 2930

[35] Y.Z. Zheng *et al.*, *Journal of Materials Chemistry A*, 3, (5) (2015), 1979

[36] C. Zhang *et al.*, *Advanced Functional Materials*, 25, (23) (2015), 3497

[37] E. Uchaker *et al.*, *Journal of Materials Chemistry A,* 2, (43) (2014), 18208

[38] C. Masquelier *et al.*, *Chemical Reviews,* 113, (8) (2013), 6552

[39] D. Choi *et al.*, *Nano Letters,* 10, (8) (2010), 2799

[40] Z. Lu *et al.*, *Chemistry of Materials,* 23, (11) (2011), 2848

[41] A. Gutierrez *et al.*, *Chemistry of Materials,* 25, (20) (2013), 4010

[42] V. Aravindan *et al.*, *Journal of Materials Chemistry A,* 1, (11) (2013), 3518

[43] D. Jugovic *et al.*, *Journal of Power Sources,* 190, (2) (2009), 538

[44] R.A. Guidotti *et al.*, *Journal of Power Sources,* 161, (2006), 1443-1449

[45] Rechargeable Li-Ion OEM Battery Products, www.Panasonic.com.

[46] W.E. Kuper, *Proceedings of 36th Power Sources Conference*, (1994), 300

[47] D.M. Bush, *Sandia Report SC-TM-64-518*, April (1964)

[48] H. Goldsmith *et al.*, *Journal of the Electrochemical Society,* 6, (1–2) (1968), 16

Chapter 2: Materials for use in Li Thermal Batteries

Chapter 2: Materials for use in Li Thermal Batteries

2.1 **Anodes for Li thermal batteries**

A high number of different materials have been studied and investigated as anode electrodes for use in Li thermal batteries until recent days. These anode materials are listed and described below.

The materials that have been used as anodes in Li thermal batteries in the early stages of the thermal battery technology, were Ca (calcium) and Mg (magnesium) foils [1]. However, this technology has been replaced quickly by the $Ca/CaCrO_4$ system in the decade of 1950s. This anode/cathode system was the basic technology for the future of Li thermal batteries.

This basic technology did not use separators between the anode and the cathode. Therefore, there was a physical contact between Ca anode and $CaCrO_4$ cathode and the cathode was dissolved in the chosen molten salt electrolyte (LiCl-KCl). This reaction created a liquid phase Ca-Li anode, which was the major disadvantage of the system as a short circuit could be obtained. This constitutes the electrochemical issue of that technology. The chemical issue of it is the direct chemical reaction (exothermic) of the Ca-Li liquid anode with the dissolved cathode. This caused an uncontrolled extra heat to the battery and the battery failed [2].

The new technology replaced these materials with calcium, magnesium, aluminium, silicon, or lithium alloys as anode electrodes.

Magnesium alloys were used as anodes in the 1970s, such as Mg-Si, Mg-B, Li-Mg and the performance of the thermal batteries was much better than the previous $Ca/CaCrO_4$ [3,4]. As new alloys were considered as anodes for use in Li thermal batteries, the next step was the mechanical processing of these alloys [5].

A limited amount of research has been published for Al (aluminium) anodes in tetrachloroaluminate-based electrolytes [6-10] as the system exhibits low rate capabilities and there are temperature limitations (250 °C) imposed by the nature of the chosen electrolyte.

Thermal batteries did not use pure Li as anode as lithium melts at 180 °C, because there would be the same issue as in the case of Ca-Li liquid anode. Nevertheless, some researchers used the liquid Li as anode, the so-called 'LAN', using Fe powder as binder [11]. The amount of the Fe powder as binder was quite big (80% wt) and this reduced the energy density and the potential specific energy of the anode. Lastly, another issue was the chemical reaction of molten Li with potassium ions on the electrolyte (LiCl-KCl).

The later studies include the investigation of Li alloys such as Li-Al, Li-Si, Li-Sb, Li-Bi, Li-Sn, Li-B and Li-Ge for use as anode electrodes.

Several patents describe the preparation of Li-Al alloys [12-14] and many authors have studied the phase diagram of Li-Al [15-18]. However, only the phase β-LiAl is suitable for use as anode in Li thermal batteries as this phase is stable at high temperatures (melting point around 700 °C).

Li-Al alloys have been replaced by Li-Si alloys in the decade of 1980s, as Li-Si alloys have higher specific energies than Li-Al alloys [19] and also, the lithium diffusion in silicon (10^{-8} cm^{-2} s^{-1}) is greater than the one in aluminium (10^{-10} cm^{-2} s^{-1}) [20]. Additionally, Li-Si alloys have better rate capabilities and multiple phase transitions [21]. The less lithium content is in the Li-Si alloy, the less power the battery will have, because of the lower rate of lithium diffusion in the alloy under high currents. There are a number of compounds that form within the Li-Si system, and as the Li content increases the potential vs Li decreases.

$Li_{13}Si_4$ alloy has the highest Li content and the least oxidation under dry-room conditions. This alloy has also a lower potential (about 157 mV) vs Li at 415 °C compared to others alloys (Li-Al, 297 mV) and this is what makes it the preferred choice in most Li thermal batteries. The capacity of $Li_{13}Si_4$ alloy is 485 mA h g^{-1} and the discharge reaction is as it is described below [22]:

$$Li_{13}Si_4 \rightarrow 4/3\ Li_7Si_3 + 11/3\ Li^+ + 11/3\ e^- \quad [2.1].$$

Li-Sb, Li-Bi and Li-Sn alloys were not attractive as they have potential vs Li, 800 mV at 400 °C, 720 mV at 487 °C, and 450 mV at 415 °C respectively, and these values are much

higher than the potential of the $Li_{13}Si_4$ alloy [17, 23]. In addition, Li-Bi has a low melting point, especially Bi (271.3 °C), and this could lead to short-circuit problems in a battery. Li-Sn has also a lower capacity of 265 mA h g^{-1} compared to $Li_{13}Si_4$ [24].

Li-B alloys exhibit a higher capacity (2138 mA h g^{-1}) than the Li-Al or Li-Si alloys but there was a difficulty in scaling; more specifically, going from a small-sized laboratory batch to a larger commercial scale. As a result, they have not been used in thermal batteries [25, 26].

Furthermore, Li-Ge alloys were tested as anodes, but they exhibited a high potential of 420 mV vs Li at 400 °C. Lastly, the very high cost of Ge metal makes them also unattractive [27, 28].

To conclude, the preferred choice of this work is the $Li_{13}Si_4$ alloy as it has a lower specific energy and energy density than the Li-Al alloys. Calcium anodes have a very fast activation but a low capacity. Li-Al anodes have a low cost, but compared to Li-Si anodes, they have a lower capacity. LAN anodes have the highest energy and power of them all, but they are expensive and their high Fe content reduces the capacity [29].

Li–Sn and Li–Bi alloys have low melting points, therefore, they could cause short circuit in thermal batteries. Li–Ge alloys exhibit high potentials vs Li for thermal batteries and have the additional limitation of Ge being exorbitantly expensive.

2.2 **Molten salt electrolytes and separators for Li thermal batteries**

Molten salt electrolytes that are used in Li thermal batteries should have some specific characteristics that are described below.

The most important characteristic of molten salt electrolytes is that they exhibit an extremely low conductivity at room temperature, a very high ionic conductivity and a low electronic conductivity at operating temperatures of 500 - 600 °C range.

All chosen molten salt electrolytes should not be evaporated inside the battery and should have a large electrochemical window, because the chemical reactions between the electrodes and the electrolyte are not desirable. As an example, the fluorides are the most stable halides F >Cl >Br > I. The oxidation potential of iodide is 3.14 V versus Li^+/Li at 450 °C [30].

Moreover, electrolytes should not be oxidized by the cathode electrode or be reduced by the anode electrode. The electrolytes should be chemically, kinetically and thermodynamically stable to both electrodes, and should be thermally stable at the battery chosen operating temperature.

High stability towards moisture and oxygen is necessary as this prevents the production of oxides and hydroxides in the molten salt.

The melting point of chosen electrolytes must be lower than the temperature of thermal decomposition of electrodes. The ability to wet both the separator and the electrodes is also important as this minimises the resistance at the electrolyte/electrode interface [31].

The most commonly used electrolytes until now are lithium-halide electrolytes, such as LiCl-KCl and LiCl-LiBr-KBr, because of their low melting points (354°C and 310 °C, respectively) [32-35] and their high ionic conductivities (1.69 S cm^{-1} at 475 °C, and 1.70 S cm^{-1} at 475 °C, respectively) [36,37]. Lithium-based electrolytes exhibit the highest ionic conductivities due to the high mobility of the lithium ions compared to other alkali-based electrolytes.

Alkali halide electrolytes have lower melting points (< 300 °C) than lithium halides but they are more expensive (example Cs and Rb). They are, also, more sensitive to moisture and cause self-discharge reactions in the batteries [38].

Some nitrate–based and chlorate systems, such as $LiNO_3$-KNO_3-$CsNO_3$, LiCl-$LiNO_3$-$NaNO_2$ and $LiClO_3$ respectively, have been examined as electrolytes for their use in thermal batteries. However, they were unattractive candidates due to their exothermic reaction of the anode and the fact that they cause complete meltdown of the battery [39]. Tetrachloroaluminates such as $NaAlCl_4$ were also used as electrolytes, but they suffer from poor conductivity of 250 - 500 mS cm^{-1} at 200 °C [40].

In Li thermal batteries, due to the high level of mechanical stress (acceleration, shock, spin, vibration, etc.), the chosen molten salt electrolyte should be firmly immobilized by a separator. Usually, the separator consists of powders of metallic oxides such as silica, alumina or magnesia that are electrical insulators.

The first material which was used as separator was ceramic fibre felts and was developed by Argonne National Laboratory [41, 42].

Then, researchers at Sandia National Laboratories in the decade of 1970s developed alternative separators to the kaolin clay that were used for Ca/LiCl–KCl/$CaCrO_4$ system [43].

Later technology used fumed silica (SiO_2) and was found to be suitable for application, as it was cheap and the electrolyte required only a small amount of 10% w.t compared to the kaolin clay that needed 30 – 40% w.t. Some fumed silicas, fumed titania and alumina were also investigated for their use as separators. The only problem was that silica had a high reactivity with metallic lithium and Li-alloys anodes at high temperatures.

Y_2O_3, ZrO_2 oxides have also been tested but MgO is the most preferred choice as it has a high thermal stability in contact with high-activity electrodes at elevated temperatures. The lithium chloride–potassium chloride (LiCl-KCl) eutectic electrolyte has become established for use at high temperature batteries and requires a minimum of 35% wt MgO as separator [44].

The amount of mass of the separator compared to the mass of the electrolyte is critical. If the mass of separator (e.g. MgO) is too low, either a short circuit between the electrodes (anode/cathode) could be caused, or a leaking of the molten electrolyte could be obtained. If any of these two happen, the battery is out of order and fails. However, if the amount of mass of the separator is too high, there is no wetting of the electrodes by the molten salt electrolyte and therefore, the ionic conductivity will be decreased.

2.3 **Cathodes for Li thermal batteries**

Cathode materials for use in Li thermal batteries should have some specific characteristics that are described below.

The crucial point is that cathodes should exhibit a high thermal stability as the operation temperature of the battery is high and the products of their thermal decomposition could not cause self-discharge of the battery.

Cathode electrodes should have both high electronic and ionic conductivity.

Cathodes should be stable towards moisture and oxygen at ambient temperature. Good wetting by the electrolyte is also important and a minimum resistance at the electrolyte/cathode interface is required [45]. These materials need to be environmentally friendly and inexpensive.

MS_2 sulfides where M is Fe, Ni or Co are the most studied cathodes until now and they exhibit voltages vs $Li_{13}Si_4$ at around 1.70 V for their first electrochemical transition. Moreover, they have further electrochemical transitions, which eventually end in complete reduction to the metal (Fe, Ni, Co respectively) [46].

2.3.1 **Cathode CoS_2**

CoS_2 was studied for first time as a cathode material at Argonne National Laboratory (ANL) in the decade of 1970s [47]. CoS_2 is preferred as cathode due to the high thermal stability, starting its thermal decomposition above 650 °C. CoS_2 decomposes to Co_3S_4 and sulfur gas is released [48].

CoS_2 crystallises in a cubic pyrite structure with a unit cell parameter (a = 5.539 Å and space group $Pa\bar{3}$) as presented in Figure 2.1. This structure of CoS_2 is primitive cubic. The cobalt ions are octahedrally coordinated by sulfur, whose pairs form dimers. Each sulfur is shared by three different octahedra and a single dimer. The axes of the diatomic anions are ordered equally along the four <111> directions of the cube and the cation octahedra share common corners [49].

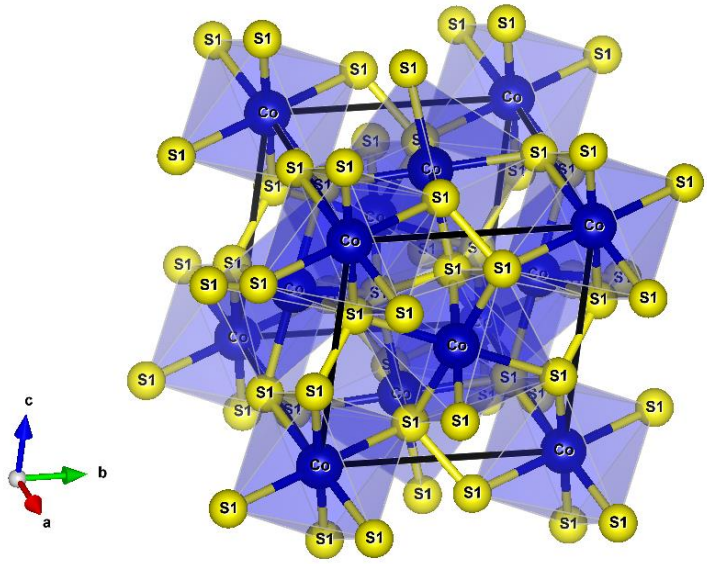

Figure 2.1. Crystal structure of CoS_2. Blue atoms are cobalt and yellow atoms are sulfur

In the discharge reactions of CoS_2 against Li-Al, as given below, no lithiated products are formed. The voltages of CoS_2 are against Li-Al at 400 °C and CoS_2 exhibits three voltage plateaus [46].

$$CoS_2 + 4/3\ Li \rightarrow 1/3\ Co_3S_4 + 2/3\ Li_2S\ \textit{(1.70 V)}\ [2.2]$$

$$Co_3S_4 + 8/3\ Li \rightarrow 1/3\ Co_9S_8 + 4/3\ Li_2S\ (\textit{1.64 V})\ [2.3]$$

$$Co_9S_8 + 16\ Li \rightarrow 9\ Co + 8\ Li_2S\ (\textit{1.37 V})\ [2.4]$$

The capacity of the first plateau (4/3 Li) is 290 mA h g^{-1} which is low as the reader could notice compared to the first plateau of FeS_2 below. However, the total capacity of CoS_2 is higher than FeS_2 with a value of 598 mA h g^{-1}.

The major advantage of CoS_2 against FeS_2 is that CoS_2 causes less self-discharge reactions in the thermal battery. As a result, the CoS_2 is an attractive material for long-life thermal batteries.

Nevertheless, CoS_2 has a major disadvantage, which is the high cost because it should only be synthesized in laboratories.

According to researchers, next studies of CoS_2 should be the way of synthesising the material with pure phase, low cost and scale up the production [47].

2.3.2 **Cathode NiS_2**

NiS_2 crystallises in a cubic pyrite structure with a unit cell parameter (a = 5.619 Å and space group $Pa\bar{3}$) as presented in Figure 2.2. NiS_2 exhibits the same structure as CoS_2 [50].

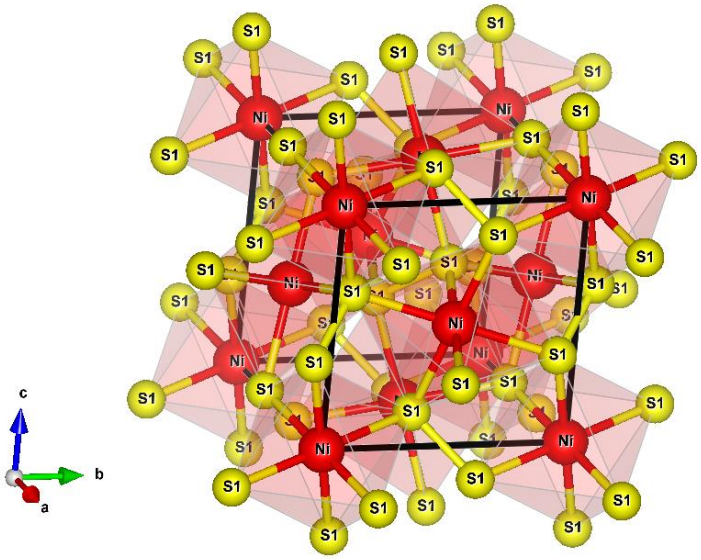

Figure 2.2. Crystal structure of NiS_2. Red atoms are nickel and yellow atoms are sulfur

NiS_2 decomposes to NiS and sulfur gas is released at the temperature of 600 °C [51]. In the discharge reactions of NiS_2 against Li-Al, as given below, no lithiated products are formed. The voltages of NiS_2 are against Li-Al at 400 °C and NiS_2 exhibits four voltage plateaus [46]. The total capacity of NiS_2 is 545 mA h g^{-1}, which is lower than both CoS_2 and FeS_2.

$$NiS_2 + 2\ Li \rightarrow NiS + Li_2S\ (\textit{1.74 V})\ [2.5]$$

$$7\ NiS + 2\ Li \rightarrow Ni_7S_6 + Li_2S\ (\textit{1.58 V})\ [2.6]$$

$$3\ Ni_7S_6 + 8\ Li \rightarrow 7\ Ni_3S_2 + 4\ Li_2S\ (\textit{1.55 V})\ [2.7]$$

$$Ni_3S_2 + 4\ Li \rightarrow 3\ Ni + 2\ Li_2S\ (\textit{1.36 V})\ [2.8]$$

Since the electrochemical performance of the NiS_2 as cathode is similar to the CoS_2 and the cost of the NiS_2 is much less than the one of CoS_2, all these characteristics make NiS_2 an attractive material for use in Li thermal batteries.

2.3.3 **Cathode FeS_2**

FeS_2 has long been used as a cathode in Li thermal batteries since 1978 [52]. FeS_2 exhibits two forms, the pyrite with a unit cell parameters (a = 5.428 Å and space group $Pa\bar{3}$) [53] and the marcasite with a unit cell parameters (a = 4.445 Å, b = 5.425 Å, c = 3.388 Å and space group Pnnm) [54] as presented in Figure 2.3 and 2.4, respectively. The pyrite structure is described above. The marcasite is an orthorhombic crystal structure. Both structures have the sulfur dimers in a short bonding distance between sulfur atoms. The structures differ only in how these dimers are arranged around the Fe atoms. In the orthorhombic marcasite structure linear chains of edge-shared octahedra run parallel to the orthorhombic *c*-axis.

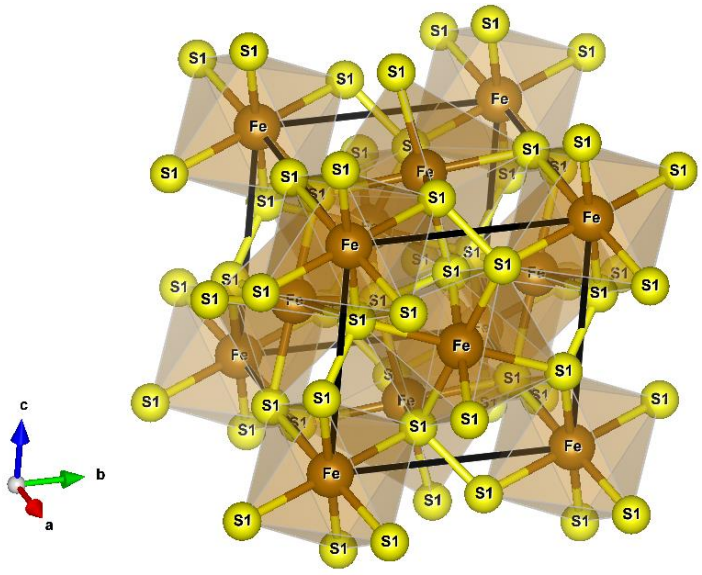

Figure 2.3. Crystal structure of pyrite FeS_2. Brown atoms are iron and yellow atoms are sulfur

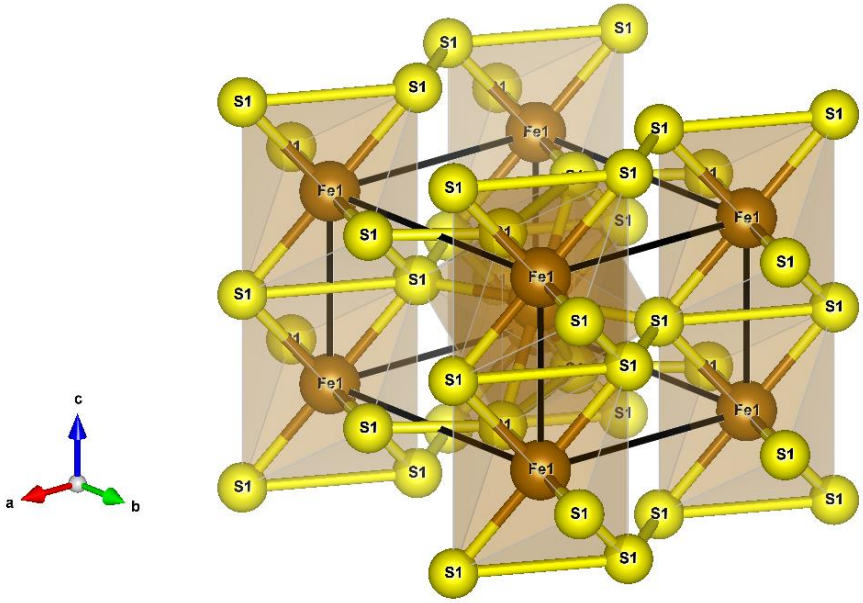

Figure 2.4. Crystal structure of marcasite FeS_2. Brown atoms are iron and yellow atoms are sulfur

FeS_2 decomposes to FeS and sulfur gas is released as well at the temperature of 580 °C in the form of pyrite. Sulfur gas reacts exothermically with the anode electrode or dissolved lithium in the chosen molten salt electrolyte [55, 56]. In the discharge reactions of FeS_2 against Li-Al, as given below, there are formed lithiated products $Li_3Fe_2S_4$ and Li_2FeS_2. The voltages of FeS_2 are against Li-Al at 400 °C and FeS_2 exhibits three voltage plateaus [46].

$$FeS_2 + 3/2\ Li \rightarrow \frac{1}{2}\ Li_3Fe_2S_4\ (1.75\ V)\ [2.9]$$

$$Li_3Fe_2S_4 + Li \rightarrow Li_2FeS_2 + FeS + Li_2S\ (1.64\ V)\ [2.10]$$

$$Li_2FeS_2 \rightarrow Fe + Li_2S + S\ (1.26\ V)\ [2.11]$$

In the first plateau (3/2 Li) the capacity of FeS_2 is 335 mA h g^{-1} which is higher than the capacity in the first plateau of CoS_2. However, the total capacity of FeS_2 is 558 mA h g^{-1} and less than the one of CoS_2.

2.4 **Aim of this project**

The improvement and the better performance of Li thermal batteries will come through the investigation of novel cathodes, as the materials which are used as anode and electrolyte/separator are standard and well-studied.

The best cathode material for use in Li thermal batteries should have a high voltage (ideally > 3 V) and a high capacity (> 614 mA h g^{-1}). It should be also a good electronic conductor and have a low solubility in the chosen molten salt electrolyte (LiCl-KCl).

The ideal circumstances will be if the cathode materials exhibit multiphase discharge (and not intercalation) as this enables better voltage control, providing a constant power for longer than the one in the case an intercalation compound was used [57, 58].

The aim of this project is to investigate, study, synthesise and characterise novel cathode materials for use in Li thermal batteries in order to improve their performance.

More specifically, this work studies some transition metal sulfides, chlorides or fluorides compositions, such as ($CoNi_2S_4$, $NiCo_2S_4$, ZrS_3, $KNiCl_3$, Li_2MnCl_4, Li_6VCl_8, $NiCl_2$, $CoCl_2$, CuF_2 and PbF_2).

The aim is, wherever is possible, to achieve spinel structure AB_2S_4 where A and B are transition metals with oxidation state A^{+2}, B^{+3}, and S^{-2}.

As a guide of this work, these cathodes should have a good thermal stability, be stable, exhibit a flat/single voltage plateau and a long shelf-life, as well as be environmentally friendly.

The characterisation of the novel cathode materials includes techniques such as powder X-ray Diffraction, Scanning Electron Microscopy, Galvanostatic discharge tests etc.

2.5 **References**

[1] H. Goldsmith *et al.*, *Journal of the Electrochemical Society,* 6, (1–2) (1968), 16

[2] R.A. Guidotti *et al.*, *Sandia National Laboratories report SAND83-2271*, September, (1985)

[3] D.M. Bush, *Sandia National Laboratories report SAND78-0084*, July, (1978)

[4] A. Isenberg, *U.S. Patent 4,054,729* (October 18, 1977)

[5] M. Sahoo *et al.*, *Journal of Materials Science,* 17, (1982), 3564

[6] N. Takami *et al.*, *Proceedings of Stationary Energy Storage Load Leveling and Remote Applications*, (88-11), The Electrochemical Society, Princeton, NJ, 1988, 106

[7] K. Koura, *Journal of the Electrochemical Society,* 127, (1980), 1529

[8] K. Koura, *Progress Batteries Solar Cells,* 3, (1980), 260

[9] N. Takami *et al.*, *Electrochimica Acta,* 33, (1) (1988), 69

[10] N. Takami *et al.*, *Denki Kagaku,* 56, (1) (1988), 28

[11] D.E. Harney, *U.S. Patent 4,221,849* (September 9, 1980)

[12] J.E. Battles *et al.*, *U.S. Patent 3,957,532* (May 18, 1976)

[13] J.E. Battles *et al.*, *U.S. Patent 4.011,372* (March 8, 1977)

[14] E.S. Buzzelli, *U.S. Patent 3,607,413* (September 21, 1971)

[15] B.M.L. Rao *et al.*, *Journal of the Electrochemical Society,* 124, (10) (1977), 1490

[16] J.R. Selman *et al.*, *Journal of the Electrochemical Society,* 124, (8) (1977), 1160

[17] T.B. Massalski *et al.*, *Binary Alloy Phase Diagrams*, 2nd edition, 1st Version, ASM International, Materials Park, OH.

[18] C.J. Wen *et al.*, *Journal of the Electrochemical Society*, 126, (12) (1979), 2258

[19] L. Redey *et al.*, *Extended Abstracts of the Spring Meeting of The Electrochemical Society*, (84-2), The Electrochemical Society, Princeton, NJ, (1984), 175

[20] R.A. Sharma *et al.*, *Journal of the Electrochemical Society,* 124, (8) (1977), 1207

[21] D.M. Bush, *Sandia National Laboratories report SAND77-0470*, June, (1979)

[22] C.J. Wen *et al., Journal of Solid State Chemistry,* 37, (1981), 271

[23] W. Weppner *et al.*, *Journal of the Electrochemical Society,* 124, (10) (1977), 1569

[24] C.J. Wen *et al.*, *Journal of the Electrochemical Society,* 128, (6) (1981), 1181

[25] S.D. James *et al.*, *Journal of the Electrochemical Society,* 123, (3) (1976), 321

[26] R.A. Sutula *et al.*, *U.S. Patent 4,162,352* (July 24, 1979)

[27] A.F. Sammells *et al.*, *U.S. Patent 4,346,152* (August 24, 1972)

[28] St.M.R. John *et al.*, *Journal of the Electrochemical Society,* 129, (2) (1982), 246

[29] http://www.atb-inc.com/technology.asp

[30] J.A. Plambeck, *Encyclopedia of Electrochemistry of Elements*, vol. X,
Ed. Marcel Dekker Inc., (1976)

[31] P. Masset *et al.*, *Journal of Power Sources,* 164, (2007), 397–414

[32] P. Masset, PhD Thesis, National Polytechnic Institute of Grenoble, Grenoble, 2002 (in French)

[33] T. Kaun, *Journal of the Electrochemical Society,* 132, (12) (1985), 3063

[34] T. Kaun, *Proceedings of the Joint International Symposium on Molten Salts*, (1987), 621

[35] D.R. Vissers *et al.*, *Journal of Power Sources*, 26, (1989), 37

[36] P. Masset *et al.*, *Journal of Power Sources,* 160, (1) (2006), 752

[37] G.J. Janz, NIST Standard Reference Database 27: *Properties of Molten Salts Database. Single Salts and Salt Mixtures Data; Density, Viscosity, Electrical Conductance, and Surface Tension*, version 20, New York, (1992)

[38] R.A. Guidotti *et al.*, *Proceedings of the Electrochemical Society 2002-19* (Molten Salts XIII), (2002), 63

[39] R.A. Guidotti, *Sandia National Laboratories*, unpublished data, (2002)

[40] J. Caja *et al.*, *Proceedings of the 17th International Power Sources Symposium on Power Sources*, (13), Bournemouth, April, (1991), 333

[41] R.B. Swaroop *et al.*, *Journal of the Electrochemical Society,* 128, (9) (1981), 1873

[42] G. Bandyopadhyay *et al.*, *Journal of the Electrochemical Society,* 129, (10) (1982), 2187

[43] D.M. Bush, *Sandia National Laboratories report SC-RR-66-202*, (1996)

[44] R.A. Guidotti *et al.*, *Sandia National Laboratories report SAND90-2104*, (1996)

[45] P.J. Masset *et al.*, *Journal of Power Sources*, 177, (2008), 595-609

[46] S.K. Preto *et al.*, *Journal of the Electrochemical Society,* 130, (1983), 264

[47] S.K. Preto *et al.*, *Journal of the Electrochemical Society,* 180, (2) (1983), 264

[48] H. Rau, *Journal of Physics and Chemistry Solids,* 37, (1976), 931

[49] Brown P.J. *et al.*, *Journal of Physics: Condensed Matter,* 17, (2005), 1583-1592

[50] Fujii T. *et al.*, *Mineralogical Journal (Japan),* 13, (1987), 448-454

[51] R.A. Guidotti *et al.*, *Proceedings of the 40th Power Sources Conference*, (2002), 250

[52] A.A. Schneider *et al.*, *US Patent 4,119,769* (October 10, 1978)

[53] Finklea S. *et al.*, *Acta Crystallographica A,* (24, 1968 - 38, 1982) 32, (1976), 529-537

[54] Buerger M.J., *Zeitschrift fuer Kristallographie, Kristallgeometrie, Kristallphysik, Kristallchemie,* (144, 1977) 97, (1937), 504-513

[55] M.C. Hash *et al.*, *Proceedings of the 8th International Symposium on Molten Salts*, (1992), 228

[56] I.C. Hoare *et al.*, *Journal of Chemical Society Faraday Transactions,* 184, (9) (1988), 3071

[57] R. A. Guidotti, *Thermal batteries: a technology review and future applications,* 27th International SAMPE Technical Conference, Abuquerque, NM October 9-12, (1995)

[58] R. A. Guidotti *et al.*, *Sandia National Laboratory, NM 87185-0614* (1996)

Chapter 3: Experimental procedure

Chapter 3: Experimental procedure

3.1 Solid State Synthesis

Solid State Synthesis is a stoichiometric reaction of powders (elements, binary compounds, ternary compounds, etc.) at high temperature in different conditions such as in air, under vacuum, or in inert or reactive gases.

The most important advantage of Solid State Synthesis is the fact that it is a very simple method and a high temperature direct reaction. However, it could become a complicated method if the synthesis requires different firing steps and atmosphere conditions to complete the reaction. Though, in consequence, a high temperature reaction usually leads to thermodynamically stable products. Another advantage of it is the selection of the atmosphere, as it is easy to use flowing gases. There are also more choices for the preparation of the samples, which needs evacuated quartz tube or any other sample holders under inert atmosphere. Moreover, the cooling step can be slow in a furnace under controlled conditions or fast in air, in water or in liquid nitrogen conditions.

The most important disadvantage of Solid State Synthesis is that it needs a long time of period in order to be completed and the reaction is limited by slow diffusion. Also, there are problems in case some reactants melt or form a vapour at the reaction temperature. Moreover, the reaction may be limited by phase diagram. Some other issues are the fact that the reaction may be incomplete or some loss of the reactants to take place. At this point, the products may not form the desired microstructure or be compositionally homogeneous. This method can be expensive as high temperatures are required for the diffusion or for bonds' break of the precursors. Additionally, the purification can be difficult with a big number of steps for the removal of impurities.

The standard Solid State Synthesis includes some key points such as the area of contact between reacting powders. It is significant to use starting reagents with large surface area in order to maximise the contact between reactants or to pelletize samples

to encourage intimate contact between crystallites. Another key point is the rate of diffusion. There are two ways to increase it: either by increasing the temperature or by introducing defects at the reagents that decompose prior or during reaction. Furthermore, the rate of nucleation of the product phase is critical as it can be maximised by using reactants with crystal structures similar to these of the product.

Solid State Synthesis starts with the selection of appropriate starting materials, which are fine grain powders and their surface area is the maximum. Also, reactive starting reagents are better than inert ones for the Solid State Synthesis and well defined compositions are required, too. The next step is to weigh out starting materials and mix them together. The mixing takes place in a mortar and pestle or in a ball mill. Following, the pressing of the mixture into pellets and the selection of the most suitable sample container have to be conducted, because the reactivity, the strength, the cost and the ductility are all important. Finally, when the sample is heated and after that cooled down, the product is ground and analysed by characterisation techniques [1].

3.1.1 **Synthesis of cathode materials**

All the cathode materials ZrS_3, $CoNi_2S_4$, $NiCo_2S_4$, $KNiCl_3$, Li_2MnCl_4 and Li_6VCl_8 were synthesised by a solid state reaction in sealed quartz tubes to prevent oxidation of starting materials during the synthesis.

$NiCl_2$ (Alfa Aesar, 99%), $CoCl_2$ (Alfa Aesar, 99.7%), CuF_2 (Alfa Aesar, 99.5%) and PbF_2 (BDH Chemicals, 99%) were used as commercial compounds.

0.966 g of zirconium (Aldrich,-100mesh) and 1.026 g of sulfur (Alfa Aesar,-100mesh, 99.5%) powders were used for the synthesis of ZrS_3 as shown in Figure 3.1 [2-5].

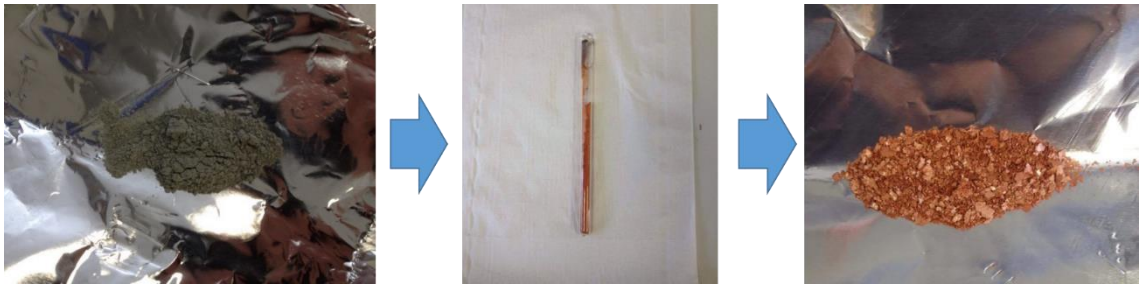

Figure 3.1 Synthesis of ZrS_3

0.77 g of nickel (Aldrich,-100mesh, 99%), 0.38 g of cobalt (Alfa Aesar,-325mesh, 99.5%) and 0.83 g of sulfur (Alfa Aesar,-100mesh, 99.5%) powders were used to synthesise $CoNi_2S_4$ [6-7].

The ratio between nickel and cobalt was changed for $NiCo_2S_4$ as 0.38 g of nickel (Aldrich,-100mesh, 99%) and 0.77 g of cobalt (Alfa Aesar,-325mesh, 99.5%).

0.73 g of KCl (Aldrich, 99%) and 1.27 g of $NiCl_2$ (Alfa Aesar, 99%) powders were used to synthesise $KNiCl_3$ [8-9].

0.81 g of LiCl (Alfa Aesar, 99%) and 1.19 g of $MnCl_2$ (Strem, 97%) powders were used to synthesise Li_2MnCl_4 [10].

1.18 g of VCl_2 (VCl_3, Aldrich, 97%) and 0.82 g of LiCl (Alfa Aesar, 99%) powders were used to synthesise Li_6VCl_8. VCl_2 was prepared through the decomposition of VCl_3 to VCl_2 under nitrogen flow at 797 °C. Following that, in order VCl_2 to be purified, it was heated at 827 °C in a quartz tube [11].

All the powders for the synthesis of transition metal sulfides were weighed out and mixed in a mortar and pestle in air and then sealed into an evacuated (10^{-3} mbar) quartz tubes before the reactions were carried out inside a tube furnace as shown in Figure 3.2. All the powders for the synthesis of transition metal chlorides were weighed out in the required stoichiometry and mixed in a mortar and pestle in an argon filled glove box and then sealed into evacuated quartz tubes (10^{-3} mbar).

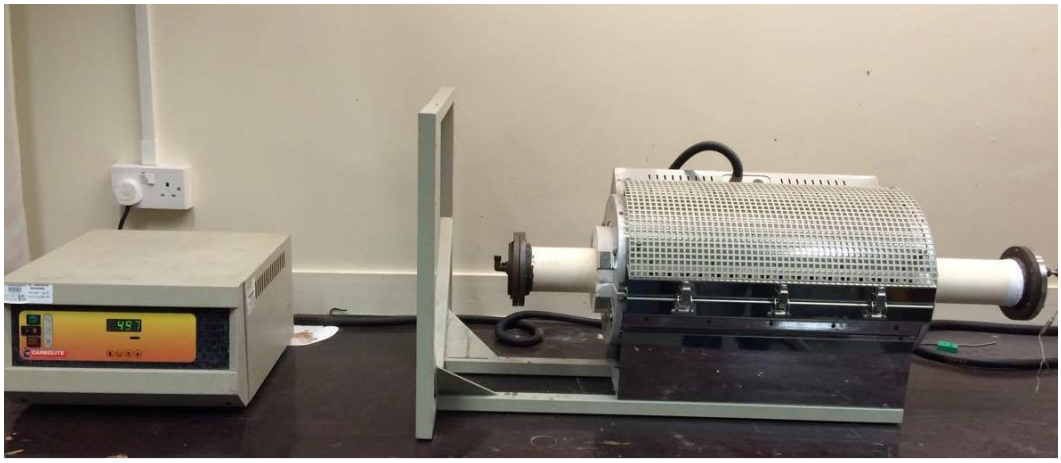

Figure 3.2. Tube furnace with the controller

ZrS_3 was fired at 730 °C for 1 week, with a heating and cooling rate of 1 °C min^{-1}. This heating and cooling rate was used for all the compounds. $CoNi_2S_4$ and $NiCo_2S_4$ were heated in a tube furnace with the duration, the temperature and the number of firings used in the synthesis as presented in Table 3.1. Between each firing the sample was ball milled under argon for 4 hours to achieve homogeneity. The duration and the temperatures of the syntheses of transition metal chlorides $KNiCl_3$, Li_2MnCl_4 and Li_6VCl_8 are presented in Table 3.2.

Table 3.1. Experimental conditions for the synthesis of $CoNi_2S_4$ and $NiCo_2S_4$

Compounds	**1st Firing**	**Ball milling**	**2nd Firing**
$CoNi_2S_4$	550 °C for 24 hours	4 hours in argon	550 °C for 156 hours
$NiCo_2S_4$	550 °C for 24 hours	4 hours in argon	550 °C for 156 hours

Table 3.2. Firings and temperatures of the syntheses of transition metal chlorides

Compounds	Firings
$KNiCl_3$	675 °C for 1 week
Li_6VCl_8	800 °C for 1 week
Li_2MnCl_4	600 °C for 1 week

3.2 **Characterisation techniques**

In this work, the characterisation of the novel cathode materials includes techniques such as Powder X-ray Diffraction or Powder Neutron Diffraction in order to identify phases and structures; Scanning Electron Microscopy–Energy Dispersive X-ray Spectroscopy in order to study phase morphology and elemental composition; and lastly, Galvanostatic Intermittent Titration Technique and Galvanostatic Discharge tests in order to investigate electrochemical performance.

3.2.1 **Powder X-ray Diffraction (PXRD)**

Powder X-ray Diffraction is a useful technique for studies of the crystallographic structure of materials. This method identifies phase purities/impurities, and lattice parameters of known/unknown phases, as well as analyses multi-phase systems [12].

This technique of X-ray diffraction has existed for over 1 century and its operation is based on the use of Bragg's Law. X-rays are electromagnetic waves with the exact same nature as light, but with wavelengths on the scale of Angstroms and with the same order

as the interatomic distances. Moreover, the incoming X-rays are scattered by the electrons of the atoms. So, the interference between the X-rays and the electrons of the atoms occurs at a certain angle from the sets of atomic planes and the scattering is unique to the crystal structure. The sample is scanned by a detector through a range of angles called 2θ so that all possible diffraction directions of the lattice can be attained due to the random orientation of the sample. At each angle where the X-rays are diffracted by these crystal planes, a 'peak' is observed by the detector. The pattern that is produced is used to analyse the structure, the cell parameters, the atom positions etc. [13].

Powder X-ray diffraction analysis was conducted in order to identify the crystalline phases. Room temperature powder X-ray diffraction data were collected for all the cathodes using a Panalytical Empyrean diffractometer in Bragg-Bretano geometry with a Ge (220) monochromator and Cu Kα1 radiation (λ=1.5406 Å) as shown in Figure 3.3.

Figure 3.3. Panalytical Empyrean diffractometer in Bragg-Bretano geometry with a Ge (220) monochromator and Cu $K\alpha_1$ radiation (λ=1.5406 Å)

For ZrS_3, $NiCo_2S_4$, $KNiCl_3$, Li_2MnCl_4, Li_6VCl_8, $NiCl_2$, $CoCl_2$, PbF_2, and CuF_2 data were collected from 5 ° to 70 ° 2θ for 1 hour with a step size of 0.017 ° and a time per step of 0.94 seconds. For $CoNi_2S_4$, data were collected in the 10 ° to 100 ° 2θ range for 1 hour, with a step size of 0.017 ° and a time per step of 0.68 seconds. All the samples are submitted in air-sensitive Si-substrate holders, covered with Kapton film for air protection.

Variable temperature powder X-ray diffraction (VTXRD) data for ZrS_3 were collected using a Panalytical Empyrean diffractometer with Mo $K\alpha_{1,2}$ radiation, ß-filter and an X'celerator RTMS detector, equipped with an Anton Paar HTK1200N furnace as shown in Figure 3.4. Data were collected from 4 ° to 40 ° 2θ for 6 hours with a step size of 0.008 ° and a time per step of 600 seconds. In this case the ZrS_3 sample was loaded into a quartz capillary and sealed for variable temperature data collection.

Crystallographica Search-Match software was used to identify known and unknown peaks and WinXPOW software was used for indexing and refining the unit cell parameters.

Figure 3.4. Panalytical Empyrean diffractometer with Mo $K\alpha_{1,2}$ radiation, ß-filter and an X'celerator RTMS detector, equipped with an Anton Paar HTK1200N furnace

3.2.2 **Powder Neutron Diffraction**

Powder neutron diffraction is a technique which is able to study both structure and dynamics; in specific, where atoms are and how atoms move. The neutrons have wavelengths which are comparable to atomic distances, therefore, they can study structures from Angstroms to the scale of microns. Also, they have energies similar to those of atomic and electronic processes enabling lattice vibrations, molecular motions, diffusion and tunnelling to be investigated. In this method, neutrons are scattered from the nucleus of an atom rather than the electrons (which X-rays are scattered from), so light atoms, such as hydrogen, lithium etc., can be seen in the presence of heavier atoms. Advantages of neutron diffraction compared to X-rays are that neighbouring elements in the periodic table can be distinguished and different isotopes of the same element can be used to label parts of molecules and enhance the technique's sensitivity. Neutrons have a relatively weak interaction with matter, so, complex sample environment can be used. Moreover, neutrons have a magnetic moment, which makes them suitable for studying magnetic materials.

Neutrons are produced by a heavy metal target when it is bombarded by an energetic proton beam from a circular, synchrotron accelerator. Then, the neutrons are slowed down by hydrogenous moderators around the target in order their energies (wavelengths) to be suitable for the materials under investigation. Finally, they are directed to some instruments, where each one of them is optimised to explore different atomic-level properties [14].

One of these instruments is the High Resolution Powder Diffractometer (HRPD), the highest resolution neutron diffractometer in the world. It is designed to achieve an optimal balance between the maximum practical resolutions attainable and reasonable counting times. All samples are loaded into cylindrical vanadium cans and are hermetically sealed before attached to sample tank of the instrument. In order to reduce air-scattering in all sample environments, the sample tank is evacuated before the data collection [15-16].

The diffracted neutron beam on HRPD can be detected in one of three fixed angle banks, at 168° (backscattering), at 90° and at low angles 30° as shown in Figure 3.5.

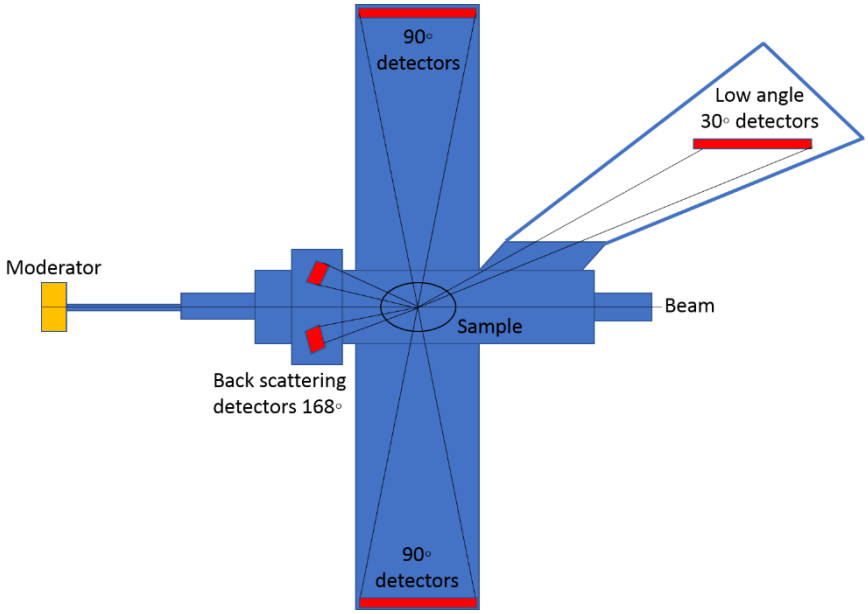

Figure 3.5. Schematic view of the HRPD detector

Powder neutron diffraction data for $CoNi_2S_4$ were collected with the High Resolution Powder Diffractometer (HRPD), using the backscattering detectors, at the ISIS neutron source, Rutherford Appleton Laboratory, UK. Rietveld refinement was carried out using the General Structure Analysis System (GSAS) [17-18].

3.2.3 **Scanning Electron Microscopy–Energy Dispersive X-ray spectroscopy (SEM-EDX)**

Scanning Electron Microscopy (SEM) is an important technique for the production of images of a solid sample's surface and also, for the analysis of the sample's elemental composition (EDX). The microscope uses a focussed electron beam from an electron gun which scans the surface of the sample and detects the secondary electrons that are returned to the detector and as a result, produces an image. If the sample is non-conductive, then it requires sputtering with gold or carbon to prevent charging of the sample and subsequent overexposure of the image. Usually, samples are placed into the

instrument as powders, which are spread on a graphite coated holder in order to study phase morphology [19].

In addition to the study of the morphology, SEM analyses the elemental composition by Energy Dispersive X-ray spectroscopy (EDX). In this method, the incoming electron beam passes through the sample and goes through inelastic scattering of the incident electrons. If the excited electron has sufficient energy, an electron may be ejected from the lower energy level of the atom. Then, a vacancy is created which is filled by an electron from the higher energy level and this results in the emission of an X-ray. The EDX method is based on energy levels of the transitions of electrons taking place in inner atomic orbitals. The energy of the X-rays emitted is exactly equal to the energy of the difference of the two electronic levels. The energy difference between each atomic orbital is unique to each element. However, EDX cannot analyse light elements such as lithium as it is difficult to identify the incident X-ray energy from other lighter elements. This means that it was impossible to study cathodes that consist of lithium such as Li_2MnCl_4 and Li_6VCl_8.

Scanning Electron Microscopy was carried out using a Jeol JSM-5600 microscope to study and identify the phase morphology. EDX on the Jeol JSM-5600 SEM was used to identify elemental composition in all synthesised cathode powders via mapping and point analysis as shown in Figure 3.6.

Figure 3.6. Jeol JSM-5600 SEM

3.2.4 **Galvanostatic Intermittent Titration Technique (GITT)**

Lithium ion thermal batteries are investigated as energy storage devices due to their relatively high power performances. During discharge of a Li thermal battery, lithium ions are transported from the anode electrode, through the electrolyte, to the cathode electrode and Li-ion diffusion occurs into the bulk material. In this respect, knowing the voltage and the current pulses, it is simple to calculate the cell resistance. Furthermore, this method can give a better understanding of thermal batteries' electrochemical behaviour. The galvanostatic intermittent titration technique (GITT) is a useful procedure for the retrieval of both thermodynamics and kinetics parameters that constitute the cell resistance.

GITT testing consists of galvanostatic discharge pulses, each 10 minutes long, followed by 5 minutes of relaxation time, with no current passing through the battery.

During a current pulse the voltage quickly decreases to a value proportional to IR and then, the voltage slowly decreases due to the galvanostatic discharge pulse. During the relaxation time, the voltage suddenly increases by a value proportional to IR and then, it slowly increases until the electrode is again in equilibrium and the open circuit voltage Voc of the battery is reached. Then, the following galvanostatic pulse is applied and this sequence of discharge pulse followed by a relaxation time is repeated until the battery is discharged [20-21].

The chemical diffusion coefficient can be calculated at each step, with the following equation

$$D = 4 / \pi t * (n_m V_m / S)^2 * (\Delta E_s / \Delta E_t)^2 \quad [3.1].$$

Where, t is the duration of the galvanostatic discharge pulse (t = 600 s), n_m is the number of moles (mol), V_m is the molar volume of the electrode (cm^3 / mol), S is the electrode/electrolyte contact area (S = 1.326 cm^2), ΔE_s is the steady-state voltage change, due to the galvanostatic discharge pulse and ΔE_t is the voltage change during the galvanostatic discharge pulse, eliminating the IR drop [20-21].

For the batteries under investigation, in order to have sufficiently slow voltage changes, a current density of 7.5 mA/cm^2 or 15 mA/cm^2 was chosen for discharge for the GITT measurements.

3.2.5 **Galvanostatic Discharge**

Galvanostatic Discharge is a technique where a current density is applied between the cathode (working) and the anode (counter) electrode and the voltage is measured. The current density is applied until the set lower voltage limit is reached or the battery is fully discharged. This technique is the main testing for the electrochemical investigation of thermal batteries of this work. In this project, different current densities were applied in a range from 7.5 mA/cm^2 to 75 mA/cm^2 in order to investigate the performance and the resulting discharge profiles.

3.3 **Preparation of Anode and Electrolyte materials**

3.3.1 **Anode material $Li_{13}Si_4$**

The anode material $Li_{13}Si_4$ (Lithium Rockwood) was selected in this work as it was described in Chapter 2.1. Therefore, the anode powder $Li_{13}Si_4$ was tested by PXRD as shown in Figure 3.7 to ensure no impurities are formed during storage. $Li_{13}Si_4$ crystallises in primitive orthorhombic *Pbam* space group with unit cell parameters (*a* = 7.9723 Å, *b* = 15.1426 Å and *c* = 4.4495 Å). There are no impurities and the resulting diffraction pattern with the red line corresponds to a single phase $Li_{13}Si_4$.

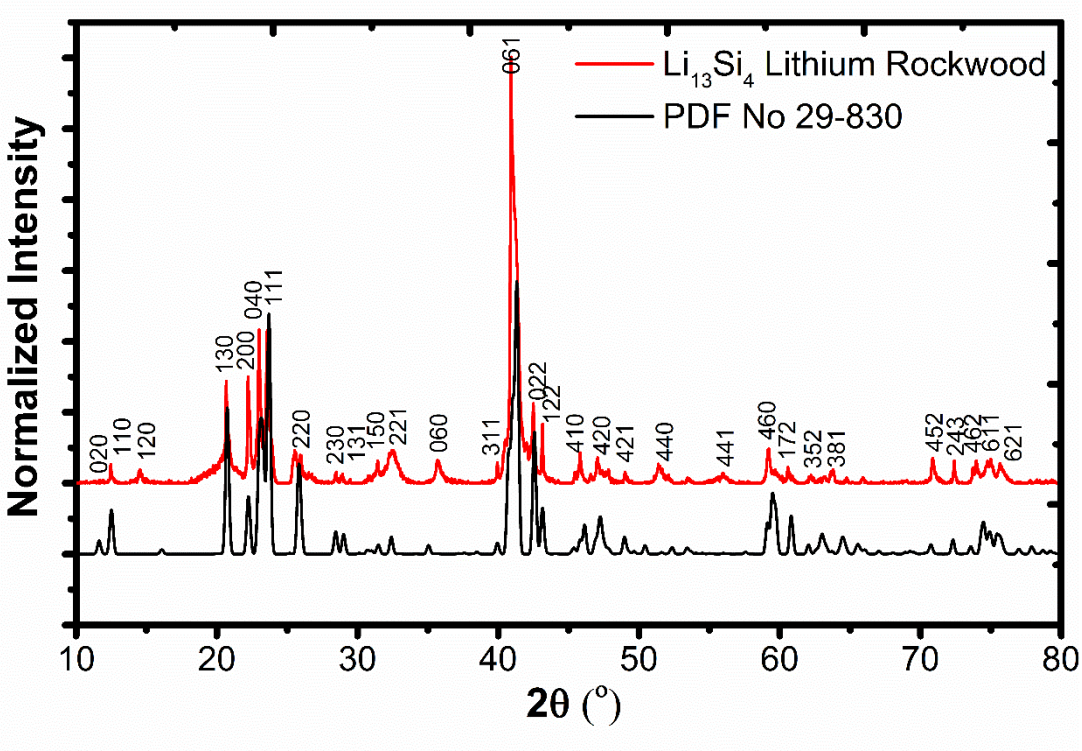

Figure 3.7. PXRD data of $Li_{13}Si_4$ compared to the simulated diffraction pattern of $Li_{13}Si_4$ using the published crystallographic model [22] (black line)

The anode electrode (75 wt % $Li_{13}Si_4$ – 25 wt % LiCl-KCl) was tested also by PXRD after discharge at 500 °C as shown in Figure 3.8 to investigate the products of the electrochemical mechanism. Figure 3.8 shows that the electrochemical result is a cubic phase *Fd*3*m* of Si with unit cell parameter (a = 5.423(8) Å). This means that Li ions are transferred to the cathode electrode and the electrochemical process is completed. There are also some peaks of SiO_2. The morphology and the elemental analysis of the anode electrode was tested by SEM/EDX as shown in Figure 3.9. The elemental analysis confirms Si 66 ±1 at % as the expected.

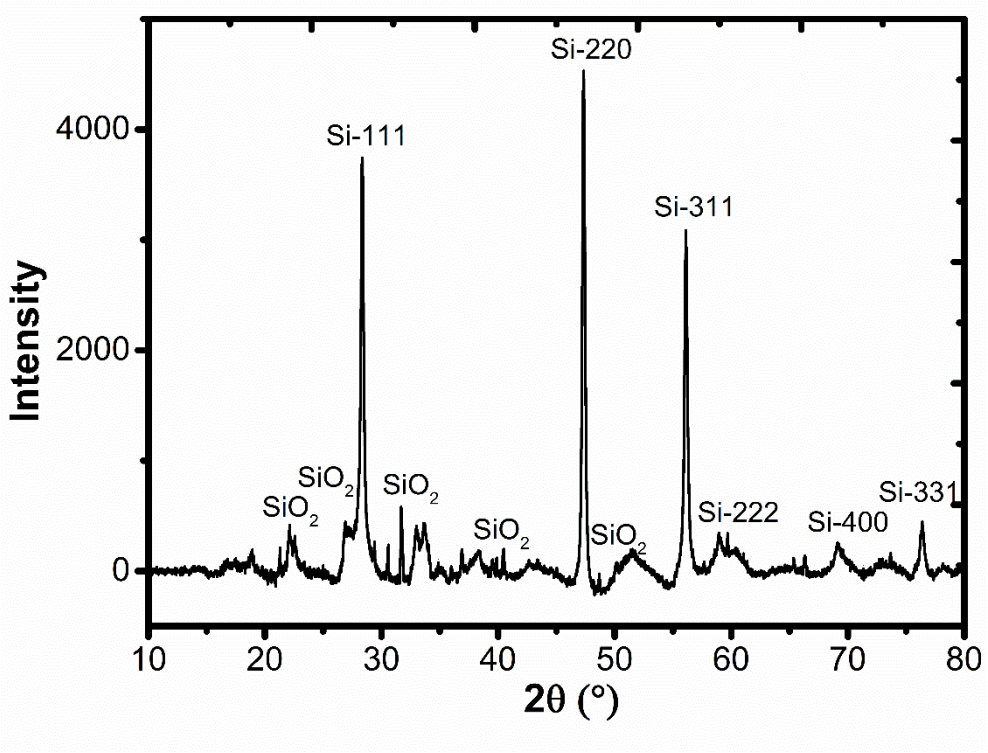

Figure 3.8. PXRD data of $Li_{13}Si_4$ (anode electrode) after discharge at 500 °C

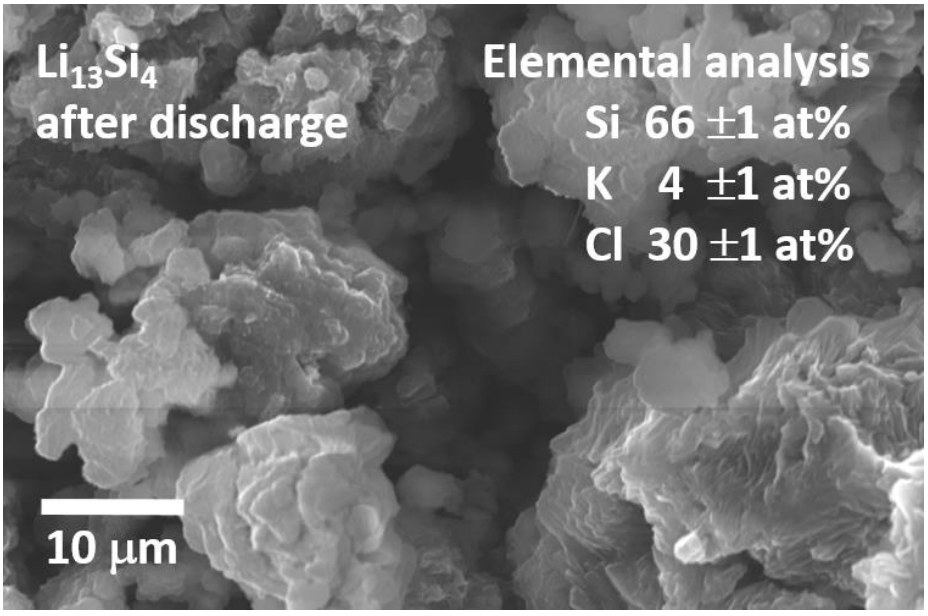

Figure 3.9. SEM image of $Li_{13}Si_4$ (anode electrode) after discharge at 500 °C

3.3.2 **Electrolyte material LiCl-KCl**

In our experiments the separator pellet between anode/cathode electrodes is a mixture of a halide eutectic, along with a binder. The electrolyte material LiCl-KCl eutectic (Sigma Aldrich, 99.99%, LiCl 44.8 wt% - 55.2 wt% KCl) and MgO as binder were selected as were described in Chapter 2.2. The MgO powder is heated up to 650 °C overnight in a muffle furnace to remove any moisture and is transferred immediately to an argon glove box to cool over another night. 11 g of LiCl - KCl eutectic and 9 g of MgO (45 wt% MgO - 55 wt% LiCl-KCl eutectic mixture) are placed into a zirconia milling pot along with zirconia milling balls (5 mm) for 4 hours at 300 rpm in order to create a homogeneous mixture of the separator. For the ball milling, a Fritcsh Pulverisette planetary ball mill was used. Figure 3.10 shows the PXRD data of 45 wt% MgO - 55 wt% LiCl-KCl eutectic mixture after milling.

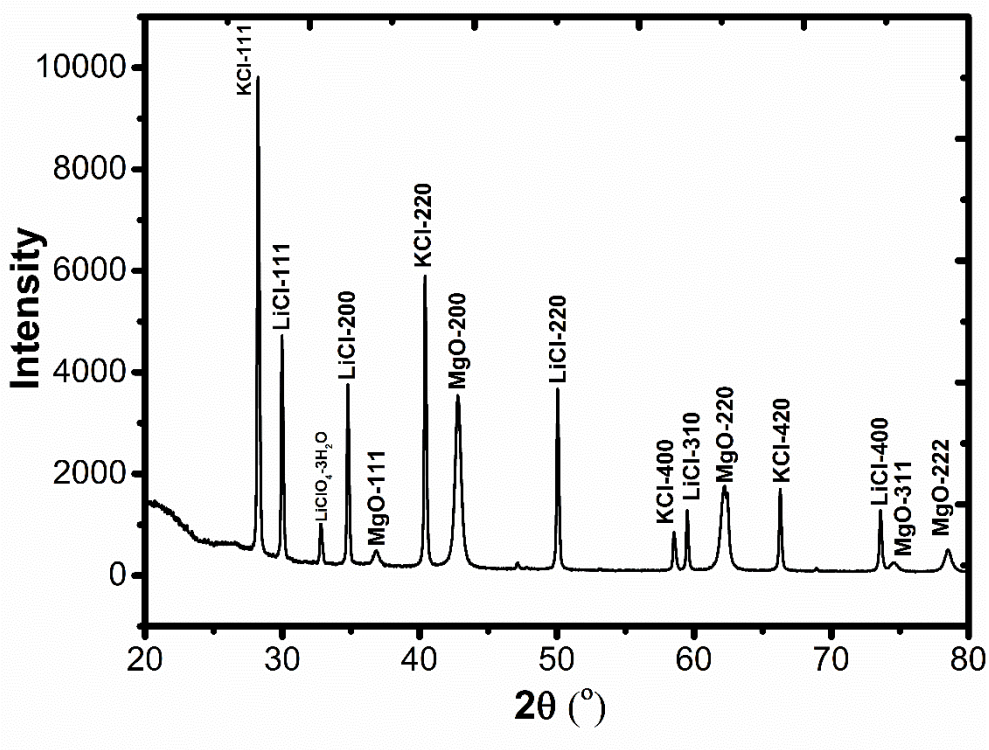

Figure 3.10. PXRD data at room temperature of 45 wt% MgO - 55 wt% LiCl-KCl eutectic

3.4 **Thermal cell fabrication and electrochemical testing**

The most important point for the testing of batteries is that batteries have to be completely free of moisture both during storage and electrochemical testing. “Swagelok” cells are used as they are the most flexible and efficient systems for electrochemical studies of batteries as shown in Figures 3.11 and 3.12. Another important issue is the mechanical pressure inside the “Swagelok” cell. In thermal batteries, the most suitable pressure for a LiCl-KCl electrolyte with a minimum 35 wt% MgO separator is 1.05 kg cm^{-2} [23]. This pressure is achieved in our “Swagelok” cells by springs that are manufactured from Inconel X750 by Skegness Springs ltd as shown in Figure 3.12.

Figure 3.11. External part of “Swagelok” cell for electrochemical measurements

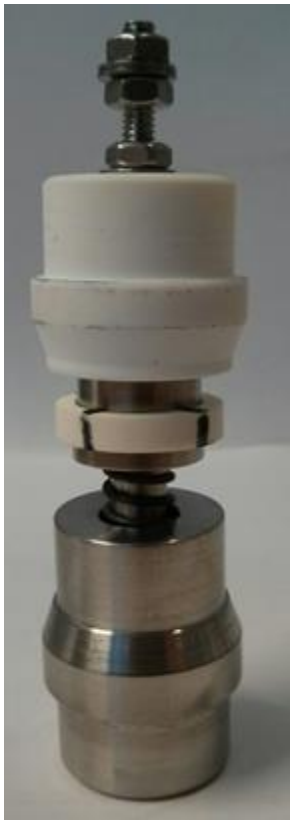

Figure 3.12. Internal parts of "Swagelok" cell for electrochemical measurements

All thermal batteries were assembled in an argon-filled glove box. Fabrication of the composite cathode pellets for high temperature electrochemical investigation was made by mixing 75 wt% ZrS_3, $CoNi_2S_4$, $NiCo_2S_4$, $KNiCl_3$, Li_2MnCl_4, Li_6VCl_8 , $NiCl_2$, $CoCl_2$, CuF_2 or PbF_2 and 25 wt% Super P Carbon. 45 wt% MgO and 55 wt% LiCl-KCl eutectic (Sigma Aldrich, 99.99%, LiCl 44.8 wt% - 55.2 wt% KCl) were ball milled under argon in order to make the separator/electrolyte. The anode was made by mixing 75 wt% $Li_{13}Si_4$ (Lithium Rockwood) and 25 wt% LiCl-KCl eutectic. The cathode, the anode and the electrolyte/separator mixtures were individually pressed into pellets of diameter 13 mm at 5 tonnes for 3 minutes using an Atlas T15 automated press. The anode, the separator/electrolyte and the cathode pellets were held in place using an alumina cup to prevent movement and graphite foil was used as current collectors top and bottom. The alumina cup was chosen as it has little interaction with the electrolyte and was ordered from Ants Ceramics (India). It is re-useable and it was cleaned using dilute nitric acid. The cell assembly was placed in a "Swagelok" fitting allowing the measurements to be carried out sealed and heated

(during this procedure the electrolyte melts and the voltage starts to rise) in an electric furnace. Cell testing was carried out at a higher temperature than the melting point of the LiCl-KCl molten salt electrolyte. The electrochemical cells were tested at elevated temperature (ZrS_3, $CoNi_2S_4$, $NiCo_2S_4$, Li_6VCl_8, $NiCl_2$, $CoCl_2$, CuF_2 and PbF_2 at 500 °C, $KNiCl_3$ at 425 °C, $LiMnCl_4$ at 400 °C) and were investigated electrochemically by a Maccor battery tester Model 5300 as shown in Figure 3.13, by galvanostatic discharge and lastly, by the galvanostatic intermittent titration technique (GITT).

Figure 3.13. Maccor battery tester Model 5300

The experimental capacity of cathodes was calculated using the Maccor software and then, this was converted to *x*, the moles of lithium ions per moles of formula unit.

For example, the experimental capacity of ZrS_3 by Maccor software was 0.03547 Ah. This number was multiplied by 3600 sec to convert in 127.692 Coulombs. Then 127.692 Coulombs were converted in 7.97×10^{20} electrons as it is known that 1 Coulomb is 6.24×10^{18} electrons. Then 7.97×10^{20} electrons were converted in 0.00132 moles of Li^+ by

being divided by Avogadro number 6.02×10^{23} mol^{-1}. Finally, the *x* number equals to 2.48, was calculated by dividing 0.00132 moles of Li^+ by 0.00534 moles of ZrS_3 active electrode.

All voltages are reported compared to the anode as a voltage reference *i.e.* all voltages are vs $Li_{13}Si_4$.

3.5 **The Effect of Super P Carbon in Li thermal batteries at 500 °C**

Super P Carbon is used in lithium ion batteries and mixed with active cathodes (20 – 25 wt %) to increase the electronic conductivity. Some other carbon materials, such as carbon nanotubes, graphene, and graphene oxide, are used electrodes as electrically conductive additives, structural stabilizers, reactive precursors, catalysts/promoters and provide a significant enhancement in the electrical energy storage performance of the batteries [24-27].

It is known that Super P Carbon exhibits a voltage plateau of 0.5 V against Li metal at room temperature [28] where the lithium ions insert into the structure. In order to investigate the electrochemical reaction of Super P Carbon in Li thermal batteries at 500 °C, a thermal cell consisted of 0.15 g of $Li_{13}Si_4$ and 0.05 g of LiCl - KCl electrolyte as an anode, 0.2 g of 45 wt% MgO - 55 wt% LiCl - KCl eutectic mixture as an electrolyte and 0.2 g of Super P Carbon as a cathode, was discharged at a current density of 15 mA/cm^2 at 500 °C as shown in Figure 3.14. According to the electrochemical results, Super P Carbon exhibits a capacity of around 90 mA h g^{-1} equivalent to 0.04 Li per mole of Super P Carbon. Also, a voltage plateau of 0.5 V against $Li_{13}Si_4$ is obtained. In this work the amount of Super P Carbon that is mixed with all the active cathodes is 0.05 g (25 wt %). This amount of Super P Carbon corresponds to around 20 mA h g^{-1} of all capacities in our experiments. In all the experiments, Super P Carbon does not look like it reacts with the LiCl-KCl electrolyte during discharge mechanism or that it is oxidized. However, as shown in Figure 3.14, when the cut–off voltage is set to a value of 0.5 V, then a short plateau for Super P Carbon against $Li_{13}Si_4$ is obtained.

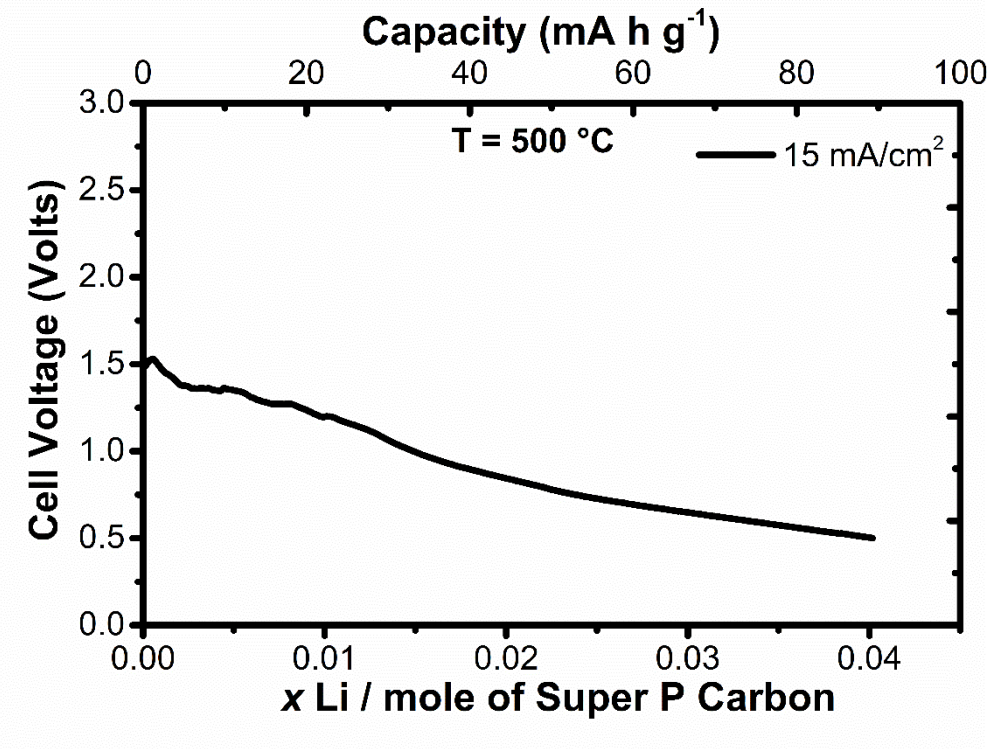

Figure 3.14. Galvanostatic discharge curve of Super P Carbon at a current density of 15 mA/cm^2 at 500 °C

3.6 **References**

[1] A.K. Cheetham *et al.*, *Solid-State Chemistry: Techniques*, (1988)

[2] Furuseth S. *et al.*, *Acta Chemica Scandinavica Series A,* (28, 1974), (29, 1975), 623-631

[3] S.G. Patel *et al.*, *Physica Status Solidi,* A, 140 (1993), 207

[4] W. Schairer *et al.*, *Physica Status Solidi,* A, 17 (1973), 181

[5] F. Levy *et al.*, *Journal of Crystal Growth*, 61, (1983), 61

[6] R.J. Bouchard *et al.*, *Inorganic Chemistry*, 4, (5) (1965) 685

[7] Huang Chunghis *et al.*, *Canadian Journal of Chemistry,* 49, (1971), 598-602

[8] Visser D. *et al.*, *Acta Crystallographica B*, (24, 1968-38, 1982), 36, (1980), 28-34

[9] D. Visser *et al.*, *Physica B*, 276, 278 (2000), 300-301

[10] Van Loon *et al.*, *Acta Crystallographica B,* (24, 1968-38, 1982), 31, (1975), 2549-2550

[11] Hanebali L. *et al.*, *Materials Research Bulletin,* 16, (1981), 887-901

[12] B.D. Cullity, *Elements of X-ray Diffraction*, Addison Wesley Mass, (1978)

[13] V.K. Pecharsky *et al.*, *Fundamentals of Powder Diffraction and Structural Characterization of Materials*, (2009)

[14] Lovesey S.W., *Theory of Neutron Scattering from Condensed Matter,* Volume 2, Condensed Matter, Oxford, Clarendon Press, (1984)

[15] Taylor A.D, *Moderated neutron pulse shapes,* Argonne National Laboratory Report 82-80, (1982)

[16] Taylor A.D, *Moderator performance predictions,* Rutherford Appleton Laboratory Report 84-120, (1984)

[17] A.C. Larson *et al.*, "General Structure Analysis System (GSAS)", Los Alamos National Laboratory Report LAUR 86-748, (1994)

[18] B.H. Toby, *Journal of Applied Crystallography,* 34, (2001), 210-213

[19] Y. Leng, *Materials Characterization: Introduction to Microscopic and Spectroscopic Methods*, (2013), 127–159

[20] C.J. Wen *et al.*, *Journal of the Electrochemical Society,* 126, (12) (1979), 2258

[21] W. Weppner *et al.*, *Journal of the Electrochemical Society,* 124, (10) (1977), 1569

[22] Frank U. *et al.*, *Zeitschrift fuer Naturforschung, Teil B. Anorganische Chemie, Organische Chemie*, 30, (1975), 10-13

[23] R.A. Guidotti *et al.*, *Sandia Report SAND90-2318*, (1995)

[24] I. Lahiri *et al.*, *Critical Reviews Solid State*, 38, (2) (2013), 128

[25] A.L.M. Reddy *et al.*, *Advanced Materials,* 24, (37) (2012), 5045

[26] N. Brun *et al.*, *Journal of Physical Chemistry C*, 116, (1) (2012), 1408

[27] M. Srivastava *et al.*, *Nanoscale*, 7, (11) (2015), 4820

[28] RM. Gnanamuthu *et al.*, *Materials Chemistry and Physics,* 130, (2011), 831-834

Chapter 4: Transition-Metal Sulfide Cathodes based on Nickel and Cobalt

Chapter 4: Transition Metal Sulfide Cathodes based on Nickel and Cobalt

4.1 Material Characterisation of $CoNi_2S_4$ and $NiCo_2S_4$

The synthesis of $CoNi_2S_4$ has previously been reported by Knop and Huang and their solid state synthesis involves multiple firings at temperatures from 500 °C to 600 °C for a total of two months. The long duration of this reaction is not practical, so it was necessary to explore a variety of synthetic conditions with the aim to synthesise this material in a shorter time frame. The synthetic conditions explored are given in Table 4.1 and corresponding diffraction patterns are shown in Figure 4.1 [1].

Table 4.1. Experimental conditions for the synthesis of $CoNi_2S_4$ [1]

Experiment Number	1st Firing	Ball milling	2nd Firing	Ball milling	3rd Firing	Single phase
Experiment 1	400 °C for 24 hours	1 hour in air with acetone	400 °C for 168 hours	1 hour in air with acetone	400 °C for 24 hours	No
Experiment 2	480 °C for 24 hours	1 hour in argon	480 °C for 168 hours	1 hour in argon	480 °C for 24 hours	No
Experiment 3	480 °C for 24 hours	Grinding in mortar and pestle in glove box	480 °C for 168 hours	Grinding in mortar and pestle in glove box	480 °C for 24 hours	No
Experiment 4	500 °C for 24 hours	1 hour in air with acetone	500 °C for 168 hours	1 hour in air with acetone	500 °C for 24 hours	No
Experiment 5	550 °C for 34 hours	4 hours in argon	550 °C for 156 hours	No	No	Yes

The first experiment was carried out at 400 °C. This involved three firing steps and two ball milling steps as outlined in Table 4.1 but this did not yield a phase pure sample. Impurities were an amount of NiS and NiS_2 as marked in Figure 4.1. NiS impurity crystallises in a hexagonal structure with cell parameters (a = 3.396 Å, c = 5.412 Å) and space group $P6_3/mmc$ compared to literature values (a = 3.451 Å, c = 5.394 Å) [2]. NiS_2 impurity crystallises in a cubic structure with a cell parameter (a = 5.641 Å) and space group $Pa\bar{3}$ compared to literature value (a = 5.669 Å) [3].

The second experiment was carried out at 480 °C. $CoNi_2S_4$ was fired three times and ball milled twice in argon and was still not a single phase. A further reaction was carried out at 480 °C replacing the ball milling step. $CoNi_2S_4$ was fired three times with hand grinding in a mortar and pestle in an argon glove box but the product was still not single phase.

The fourth experiment was carried out at 500 °C, $CoNi_2S_4$ was fired three times and ball milled twice and the phase purity was comparable to the reaction carried out at 480 °C. Increasing the temperature to 550 °C resulted in a phase pure sample. The final conditions were explored, the best synthetic conditions for the synthesis of $CoNi_2S_4$ were found to be synthesizing the sample in 8 days with 2 firing steps (at temperature of 550 °C) by using ball milling in argon as an intermediate step.

The reader can notice that the reactions carried out at 480 °C show an improved phase purity with respect to the reactions carried out at 400 °C as shown in Figure 4.1. All peaks in the diffraction pattern (red line) could be assigned to $CoNi_2S_4$ as a single phase with a cell parameter (a = 9.4239(8) Å) and space group $Fd\bar{3}m$ [1].

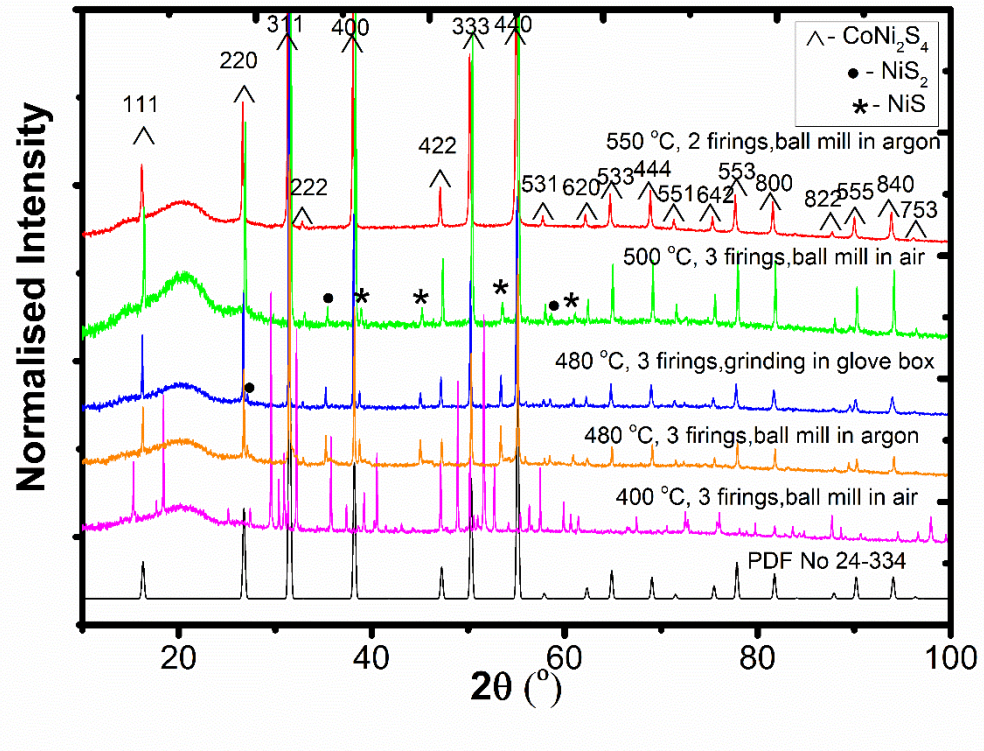

Figure 4.1. PXRD data of $CoNi_2S_4$ (using different synthetic conditions) compared to the simulated diffraction pattern using the published crystallographic model [4] (black line). The broad peak at around 20 ° is from the protective air sensitive film which is used during data collection. NiS and NiS_2 impurities are marked [1]

Once the best conditions were found for the synthesis of $CoNi_2S_4$, $NiCo_2S_4$ was synthesised using the same conditions. The PXRD pattern is shown in Figure 4.2. The experimental pattern (red line) in Figure 4.2 shows that the main phase is $NiCo_2S_4$ with cell parameter (a = 9.3883(8) Å) and space group $Fd\bar{3}m$. A small amount of Co_9S_8 impurity with cell parameter (a = 9.962(8) Å) and space group $Fm\bar{3}m$ was present in the diffraction pattern. Further optimisation of the synthetic conditions should be explored for the synthesis of pure $NiCo_2S_4$.

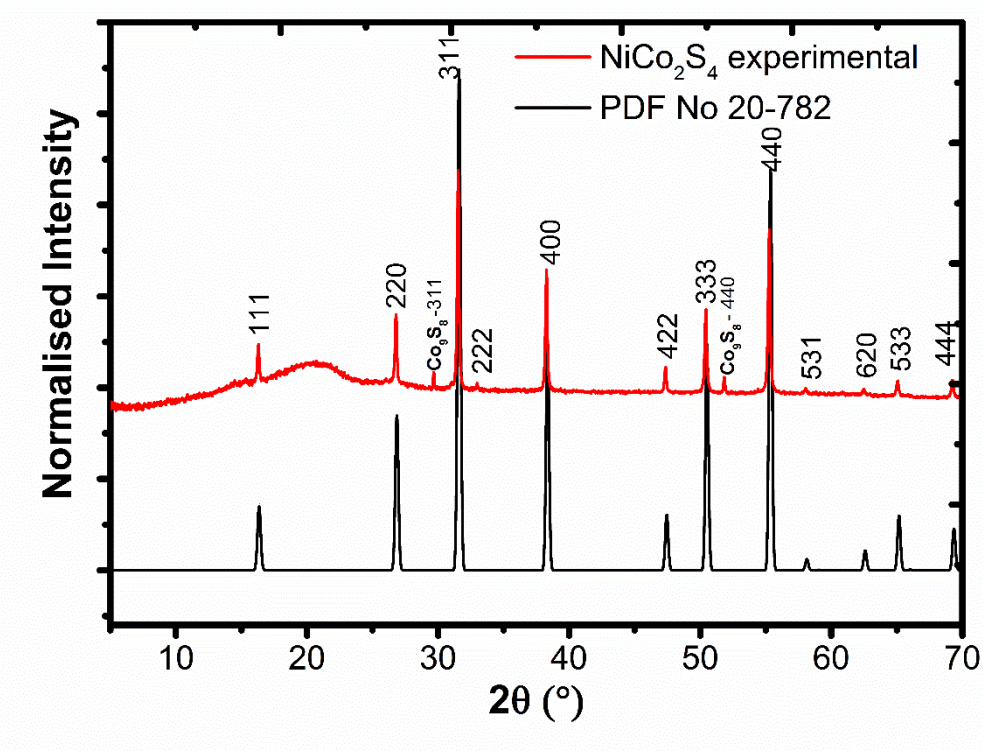

Figure 4.2. PXRD data of $NiCo_2S_4$ (red line) compared to the simulated diffraction pattern using the published crystallographic model [5] (black line). A Co_9S_8 impurity is marked

The morphology and the shape of the crystallites of $CoNi_2S_4$ and $NiCo_2S_4$ were investigated by SEM and are shown in Figures 4.3 and 4.4. The elemental composition was also analyzed by EDX. The size of the particles ranges from 1 to 10 μm and the shape of crystallites corresponds to the shape of the spinel structure which forms octahedra [6, 7].

EDX analysis confirms the elemental composition of $CoNi_2S_4$ and of $NiCo_2S_4$ as the expected and the data, compared with theoretical values, are given in Table 4.2.

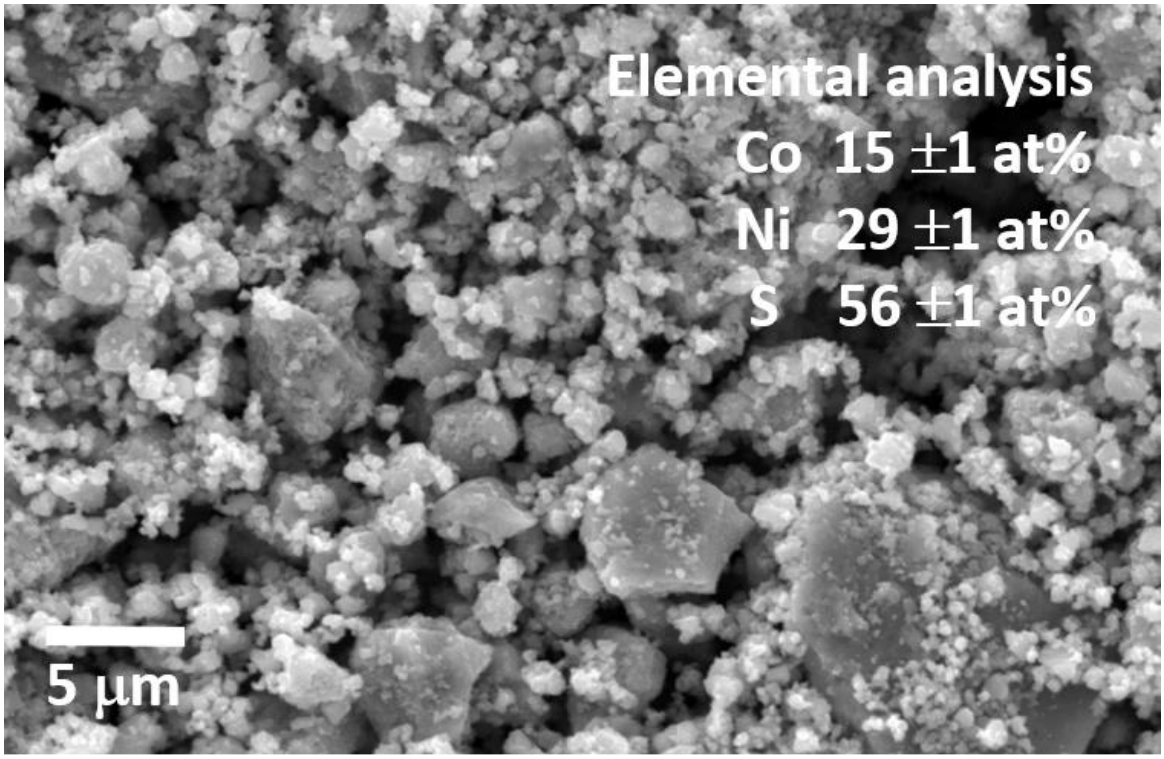

Figure 4.3. SEM image of $CoNi_2S_4$ [1]

Table 4.2. EDX analysis of $CoNi_2S_4$ and $NiCo_2S_4$

Elements	Experimental	Theoretical
$CoNi_2S_4$		
Co	15 ±1 at%	14 at%
Ni	29 ±1 at%	29 at%
S	56 ±1 at%	57 at%
$NiCo_2S_4$		
Ni	16 ±2 at%	14 at%
Co	31 ±2 at%	29 at%
S	53 ±2 at%	57 at%

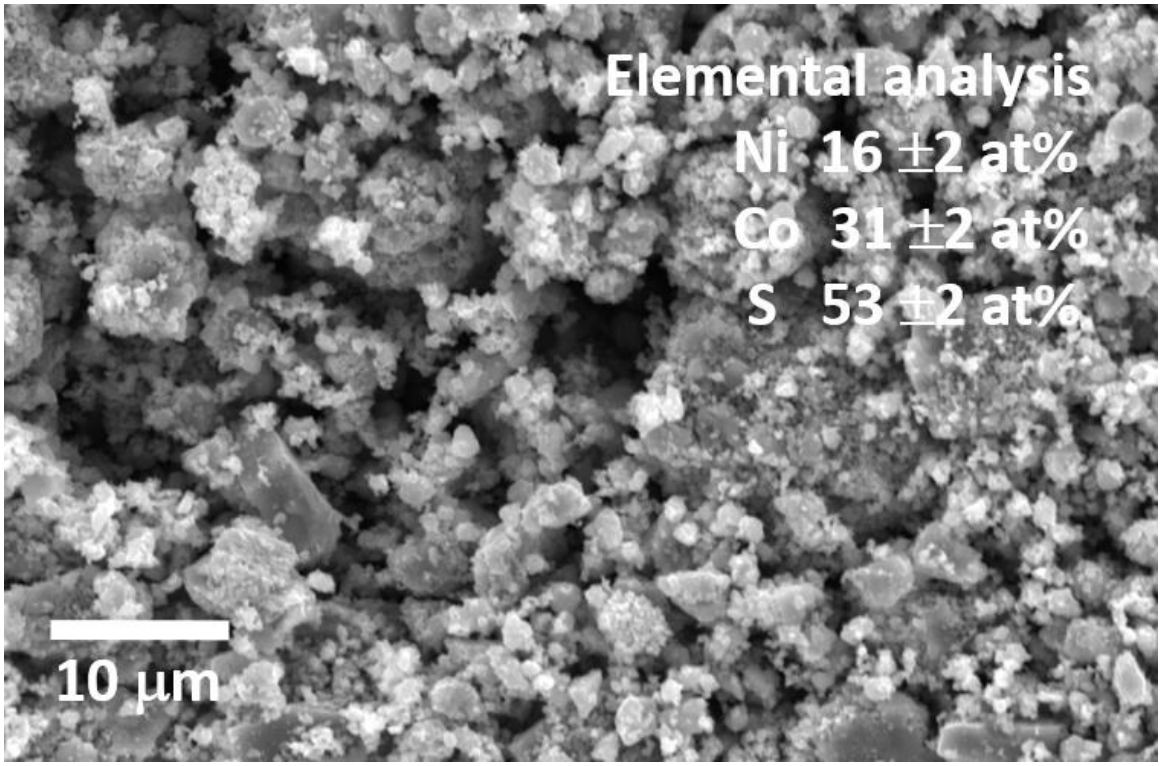

Figure 4.4. SEM image of $NiCo_2S_4$

As Co^{2+} and Ni^{3+} are isoelectronic, it is not possible to distinguish between the possible Co and Ni ordering using powder X-ray diffraction. Powder neutron diffraction is the ideal tool to study such a material given the difference in neutron scattering lengths of Co and Ni (2.49 and 10.30 fm, respectively) [8]. In order to explore the thermal stability of $CoNi_2S_4$ at elevated temperature and to probe cation (dis)ordering, variable temperature powder neutron diffraction data were collected at temperatures in the range from 25 °C - 500 °C. The Rietveld fits to powder neutron diffraction data, at 25 °C, 300 °C and 500 °C, are shown in Figure 4.5 [1].

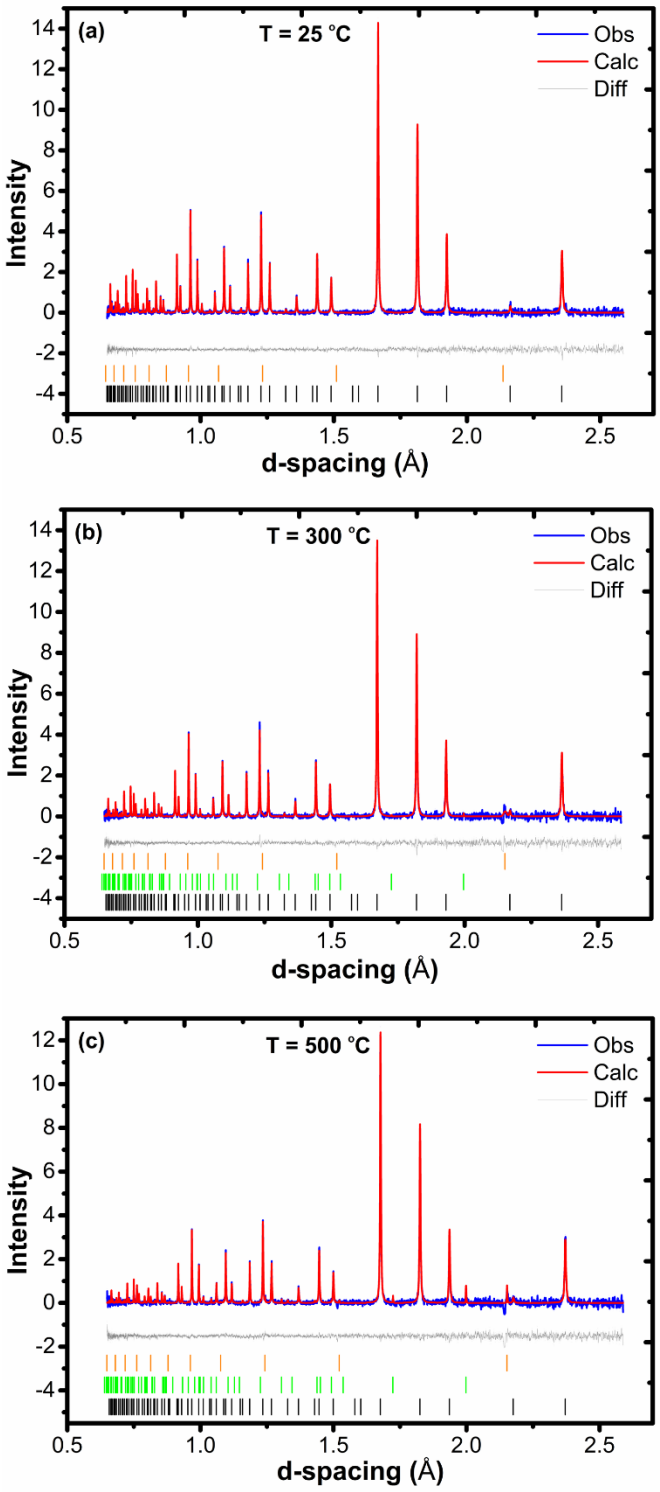

Figure 4.5. Rietveld fit to powder neutron diffraction data using an inverse spinel model for $CoNi_2S_4$ at 25 °C (a), at 300 °C (b) and at 500 °C (c). (Black tick marks are $CoNi_2S_4$, green tick marks are vanadium and orange tick marks are $Ni_{1-x}Co_xS$) [1]

Refinement of the $CoNi_2S_4$ structural model was carried out in the 25 °C to 500 °C, range. Cell parameters, atomic coordinates for sulfur, cation occupancies, an overall isotropic temperature parameter for the cation sites, an isotropic temperature parameter for the sulfur site, 18 background parameters and a scale factor were refined.

In initial refinements, cation ordering on the both the 8a and 16d sites was tested across the full temperature range. Refinements of the occupancy of the 8a site found that this site was site fully occupied by nickel and in subsequent refinements the occupancy of the 8a site was fixed to 100 % nickel. At room temperature, Rietveld refinement confirms that $CoNi_2S_4$ adopts an inverse spinel structure as shown in Figure 4.6.

Thio-spinels with the general formula $A^{2+}B^{3+}{}_2S^{2-}{}_4$ have the sulfur anions arranged in a cubic close-packed lattice and the A^{2+} and B^{3+} cations occupy the octahedral and tetrahedral sites in the lattice. In the $NiCo_2S_4$ structure, the Co^{3+} cations occupy half of the octahedral holes, while the Ni^{2+} cations occupy one-eighth of the tetrahedral holes. In the $CoNi_2S_4$ structure, the Co cations and half of the Ni cations occupy octahedral sites, while the remaining Ni cations occupy tetrahedral sites as shown in Figure 4.6 [1].

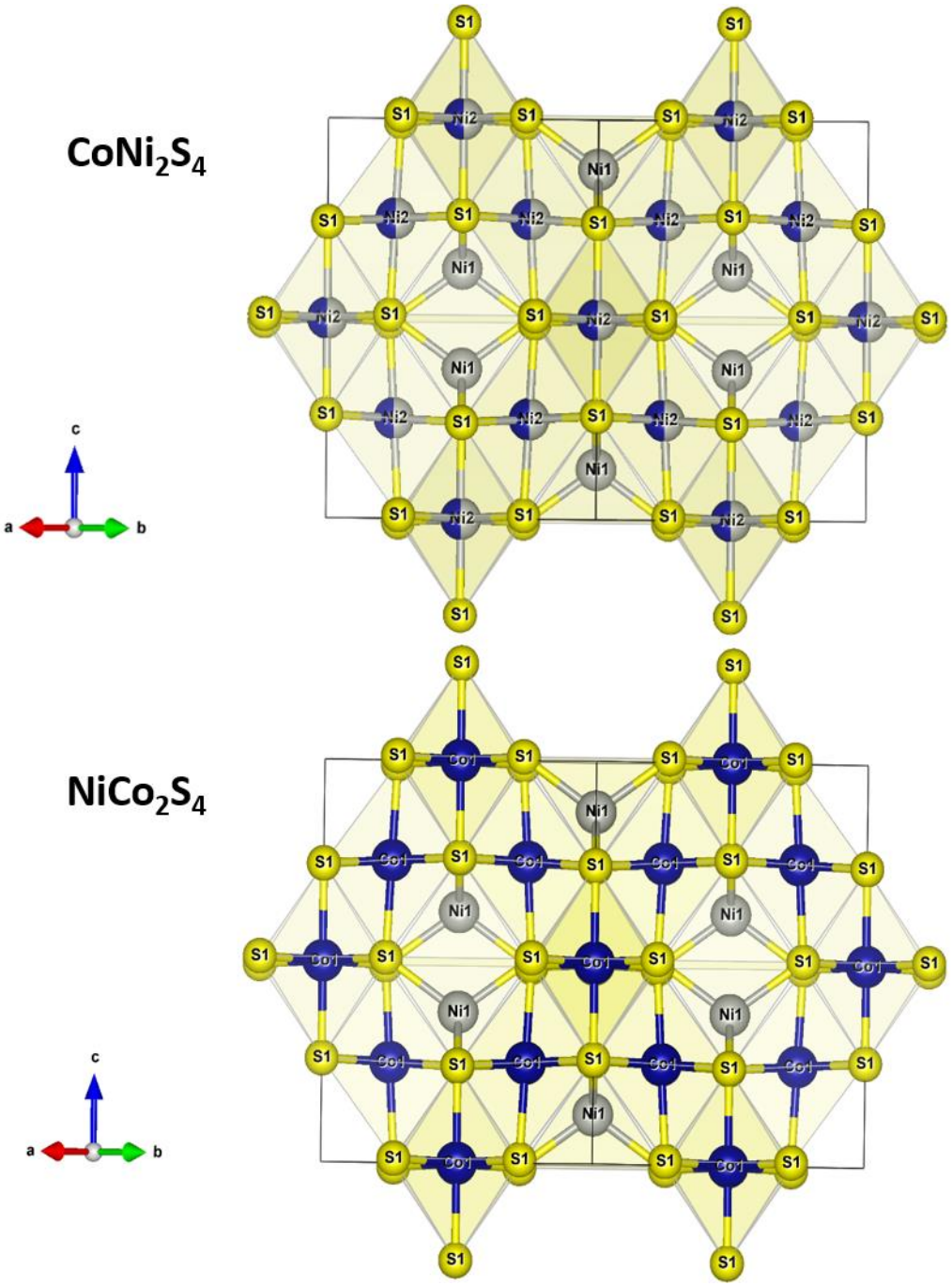

Figure 4.6. Crystal structure of an inverse spinel $CoNi_2S_4$ compared to normal spinel $NiCo_2S_4$. Yellow atoms are sulfur, gray atoms are nickel and blue atoms are cobalt

Refinement of cation occupancies retains an essentially ordered distribution of cobalt and nickel with no evidence of cation anti-site disorder or non-stoichiometry on the 16d site. This ordering pattern is retained up to 200 °C, but above this temperature, there is a gradual increase of nickel on the 16d site with increasing temperature, as shown in Figure 4.7. This was accompanied by a small decrease in the atomic coordinates of sulfur as these moved closer to ideal 0.25 value. As the S atom is on a 32e site (all the three coordinates are equal to x) then we need to specify only one parameter for the sulfur coordinate. At 500 °C, a small amount of secondary phase can be observed in the diffraction pattern (Figure 4.5) and this can be attributed to a "$Ni_{1-x}Co_xS$" $P6_3/mmc$ phase (a = 3.4468(2) Å, c = 5.3787(6) Å). This suggests some sulfur loss under the vacuum conditions of this experiment. The cell parameter of the unit cell increases as the temperature increases as shown in Figure 4.7. All the refined structural parameters of $CoNi_2S_4$ are presented in Table 4.3 [1].

Table 4.3. Selected structural parameters of $CoNi_2S_4$ [1]

Temperature	**25 °C**	**300 °C**	**500 °C**
R_{wp} %	2.25	2.15	2.01
Chi^2	2.114	1.834	1.737
Unit cell *a* / (Å)	9.42448(3)	9.45626(4)	9.48343(4)
Ni occupancy on 16d site	0.511(5)	0.527(6)	0.578(6)
***(x,x,x)* 32e site (for sulfur)**	0.2589(13)	0.2582(15)	0.2580(17)
Ni (8a)-S (Å)	2.186(2)	2.183(2)	2.185(3)
Ni/Co (16d)-S (Å)	2.2752(11)	2.2884(13)	2.2971(16)

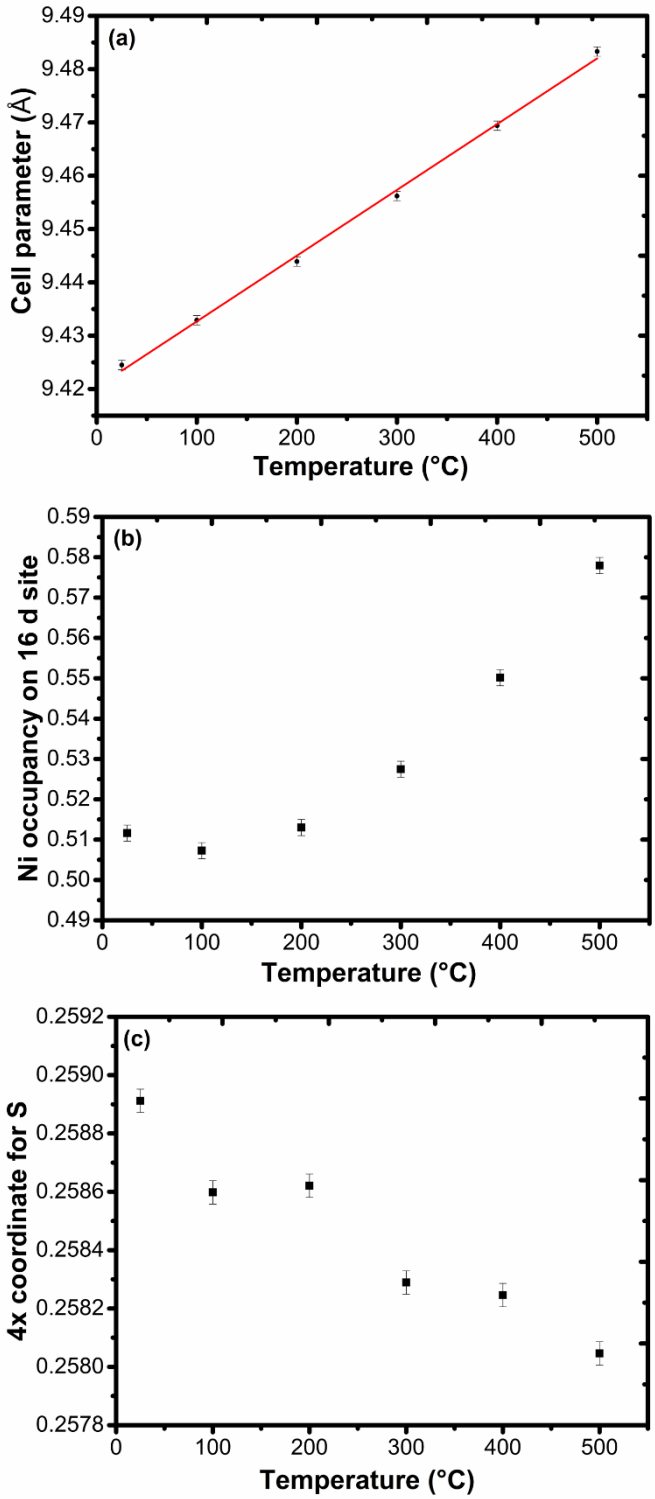

Figure 4.7. Unit cell parameter of $CoNi_2S_4$ *vs* temperature from 25 °C up to 500 °C (a), Ni occupancy *vs* temperature (b) and '4*x*' coordinate (for sulfur) *vs* temperature (c) [1]

All the spinels Ni_3S_4 (a = 9.489 Å) [9], $CoNi_2S_4$ (a = 9.4239(8) Å), $NiCo_2S_4$ (a = 9.3883(8) Å) and Co_3S_4 (a = 9.401 Å) [10] crystallise in a cubic structure with space group $Fd\bar{3}m$. However the unit cell differs as the amount of cobalt (Co) metal is increasing as shown in Figure 4.8. The atomic radius of Co metal is higher (152 pm) compared to the atomic radius of Ni metal (149 pm) [11].

However in Ni_3S_4, low spin Ni^{3+} cations occupy octahedral sites with ionic radius 56 pm and high spin Ni^{2+} cations occupy tetrahedral sites with ionic radius 55 pm [12]. The M – S distance (where M is transition metal) in octahedral sites is 2.289(5) Å and in tetrahedral sites is 2.204(5) Å. This results to the largest unit cell of all the other spinels. In $CoNi_2S_4$, high spin Ni^{2+} cations occupy tetrahedral sites with ionic radius 55 pm and low spin Ni^{3+} cations occupy octahedral sites with ionic radius 56 pm. The low spin Co^{3+} cations occupy octahedral sites with ionic radius 54.5 pm [12]. The M – S distance in octahedral sites is 2.273(3) Å and in tetrahedral sites is 2.189(3) Å. This results to a smaller unit cell than Ni_3S_4. In $NiCo_2S_4$, low spin Co^{3+} cations occupy octahedral sites with ionic radius 54.5 pm and high spin Ni^{2+} cations occupy tetrahedral sites with ionic radius 55 pm. M – S distance in octahedral sites is 2.265(3) Å and in tetrahedral sites is 2.181(3) Å. This results to a smaller unit cell than $CoNi_2S_4$. Finally, in Co_3S_4, low spin Co^{3+} cations occupy octahedral sites with ionic radius 54.5 pm and high spin Co^{2+} cations occupy tetrahedral sites with ionic radius 58 pm [12]. M – S distance in octahedral sites is also 2.268(5) Å and in tetrahedral sites is 2.184(5) Å. This corresponds to a larger unit cell than $NiCo_2S_4$.

Experimental values M – S distances in both $CoNi_2S_4$ and $NiCo_2S_4$ are in agreement with the literature [4]. The low spin cation has a high preference to the octahedral sites and the high spin prefers the tetrahedral sites [4]. So as the low spin of Ni^{3+} cations exhibits higher ionic radius than the low spin of Co^{3+} cations in octahedral sites this suggests a bigger unit cell.

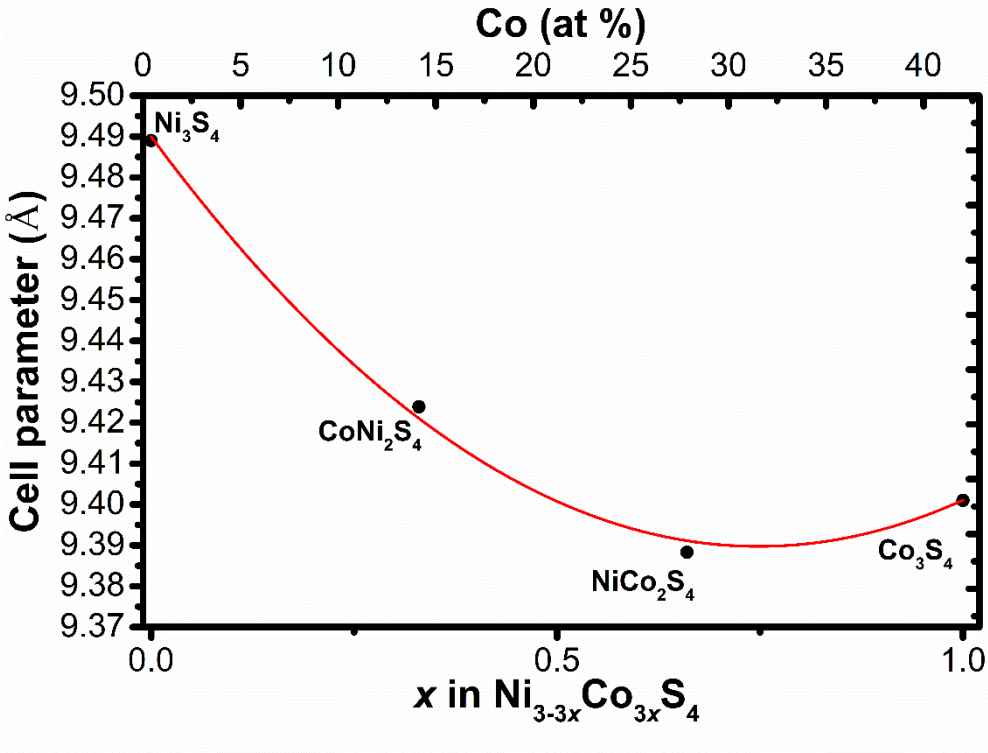

Figure 4.8. Unit cell parameters of the spinels Ni_3S_4, $CoNi_2S_4$, $NiCo_2S_4$ and Co_3S_4 *vs* cobalt (at %) or *x* in $Ni_{3-3x}Co_{3x}S_4$ formula

4.2 Electrochemical Investigation of $CoNi_2S_4$ and $NiCo_2S_4$

$CoNi_2S_4$ and $NiCo_2S_4$ were investigated electrochemically by galvanostatic discharge and galvanostatic intermittent titration technique.

Galvanostatic discharging of $CoNi_2S_4$ was performed at current densities from 15 to 60 mA/cm^2 at 500 °C and the results are presented in Figure 4.9. The lower voltage cut-off for the measurement was 1 Volt. At current densities of 15 and 19 mA/cm^2, $CoNi_2S_4$ exhibits a flat voltage plateau at 1.75 V for x = 1.33 Li, and then a second plateau at 1.50 V for x = 2.66 Li. A total capacity of 350 mA h g^{-1} was achieved at both current densities. At higher current densities of 30, 45, and 60 mA/cm^2 the voltages of these plateau are lower by 50 mV and this is probably due to a higher cell resistance.

The amount of active anode (0.15 g) corresponds to 73 mA h for the discharge plateau from $Li_{13}Si_4$ to Li_7Si_3 which is 0.157 V vs Li metal. The measured capacity of $CoNi_2S_4$ of the first discharge plateau is 17.50 mA h and of the second discharge plateau is 35 mA h. Total 52.5 mA h, which keeps the discharge as being performed against the 0.157 V vs Li metal plateau [1].

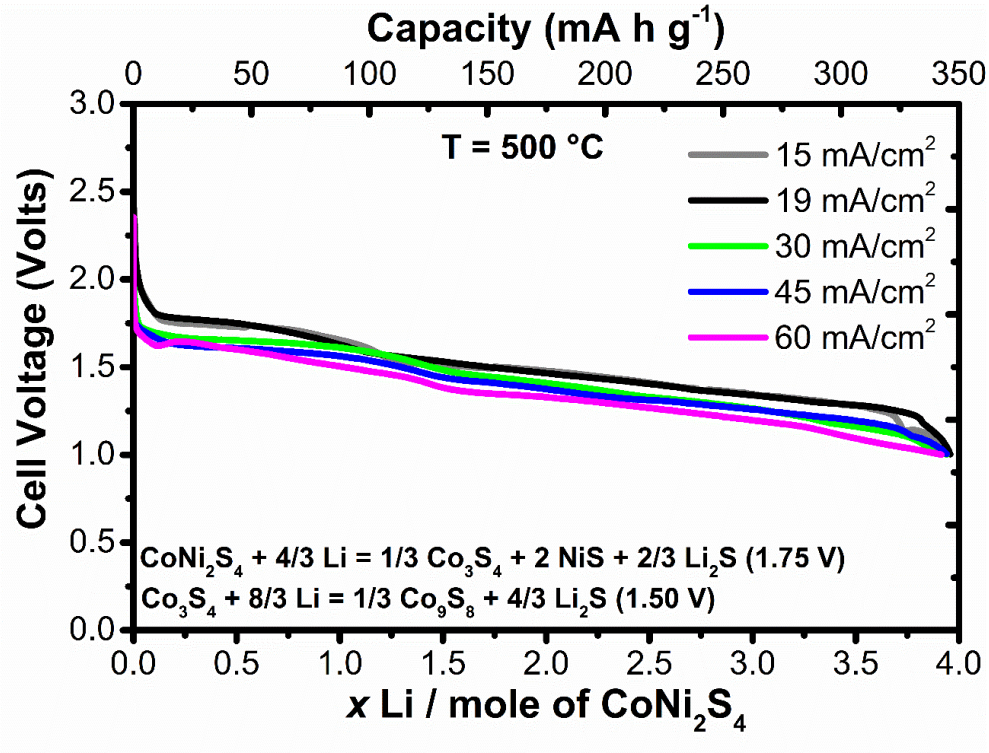

Figure 4.9. Galvanostatic discharge of $CoNi_2S_4$ at current densities from 15 to 60 mA/cm^2 at 500 °C [1]

The galvanostatic intermittent titration technique of $CoNi_2S_4$ was performed at a current density of 7.5 mA/cm^2 at 500 °C and the results are presented in Figure 4.10. In this method the voltage of $CoNi_2S_4$ drops between the pulse of current and the relaxation period until a voltage of 0.5 V is reached. The IR drop is 100 mV at the beginning of discharge and 175 mV at the end of the measurement, which indicates that the cell resistance is increasing during the reduction of the cathode, from a resistance of around 13 Ω at the beginning of the measurement to around 23 Ω after the cell discharge, which suggests that it is getting increasingly difficult to insert lithium ions into the structure of the cathode electrode.

The chemical diffusion coefficient D = 9.18 10^{-7} cm^2 s^{-1} for $CoNi_2S_4$ can be calculated from equation [3.1] where n_m = 0.000656 (mol), V_m = 63.06 (cm^3 / mol), ΔE_s = 0.050 (V) and ΔE_t = 0.075 (V).

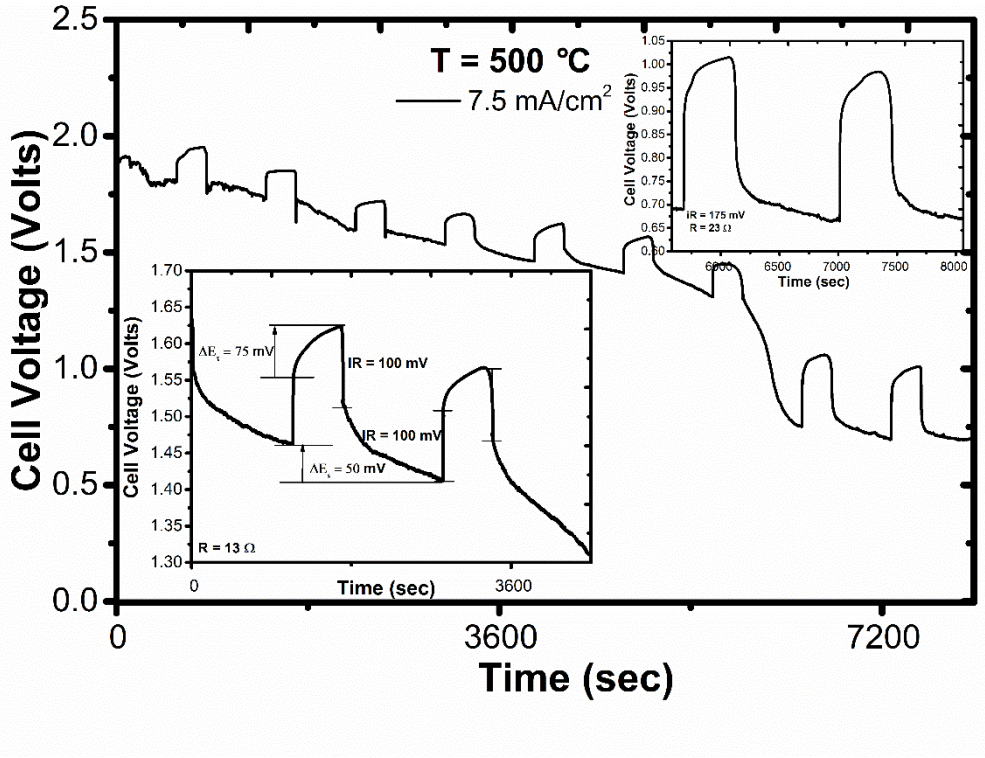

Figure 4.10. Galvanostatic intermittent titration technique of $CoNi_2S_4$ at a current density of 7.5 mA/cm^2 at 500 °C

Galvanostatic discharging of $NiCo_2S_4$ was performed at current densities from 7.5 to 60 mA/cm^2 at 500 °C and the results are presented in Figure 4.11. The voltage cut off for this measurement was 1 Volt. At a current density of 7.5 mA/cm^2, $NiCo_2S_4$ exhibits a flat voltage plateau at 1.70 V for x = 0.66 Li, and then a second plateau at 1.50 V for x = 2.66 Li. A total capacity of 290 mA h g^{-1} was achieved. At higher current densities of 15, 30, 45 and 60 mA/cm^2 the voltage of the second plateau is 50 mV lower and this is probably due to a higher cell resistance. The amount of active anode (0.15 g) corresponds to 73 mA h for the discharge plateau from $Li_{13}Si_4$ to Li_7Si_3 which is 0.157 V vs Li metal. The measured capacity of $NiCo_2S_4$ of the first discharge plateau is 9 mA h and of the second discharge plateau is 35 mA h. Total 44 mA h, which keeps the discharge as being performed against the 0.157 V Li metal plateau.

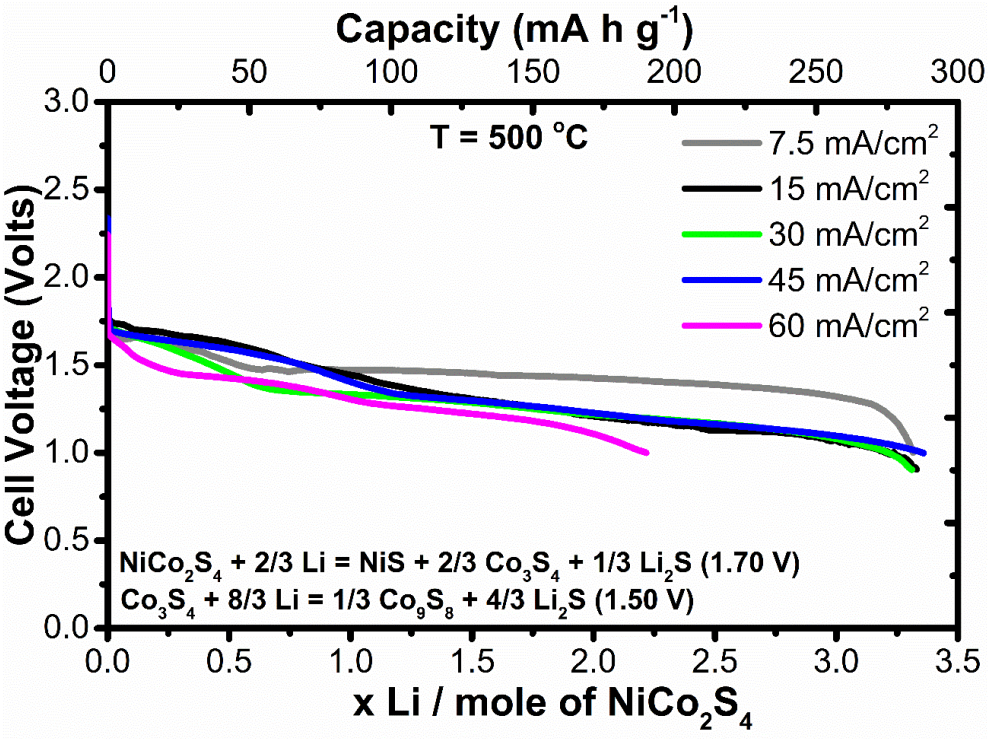

Figure 4.11. Galvanostatic discharge of $NiCo_2S_4$ at current densities from 7.5 to 60 mA/cm^2 at 500 °C

The galvanostatic intermittent titration technique of $NiCo_2S_4$ was performed at a current density of 7.5 mA/cm^2 at 500 °C and data are shown in Figure 4.12. During discharge the voltage of $NiCo_2S_4$ drops between the current pulses and the relaxation period until a voltage of 0.5 V is reached. The IR drop is 100 mV at the beginning of discharge and 150 mV at the end of the measurement, which indicates that the cell resistance is increasing from a resistance of around 13 Ω at the beginning of the measurement to around 20 Ω after the cell discharge.

The chemical diffusion coefficient D = 7.00 10^{-6} cm^2 s^{-1} for $NiCo_2S_4$ can be calculated from equation [3.1] where n_m = 0.000656 (mol), V_m = 62.20 (cm^3 / mol), ΔE_s = 0.140 (V) and ΔE_t = 0.075 (V).

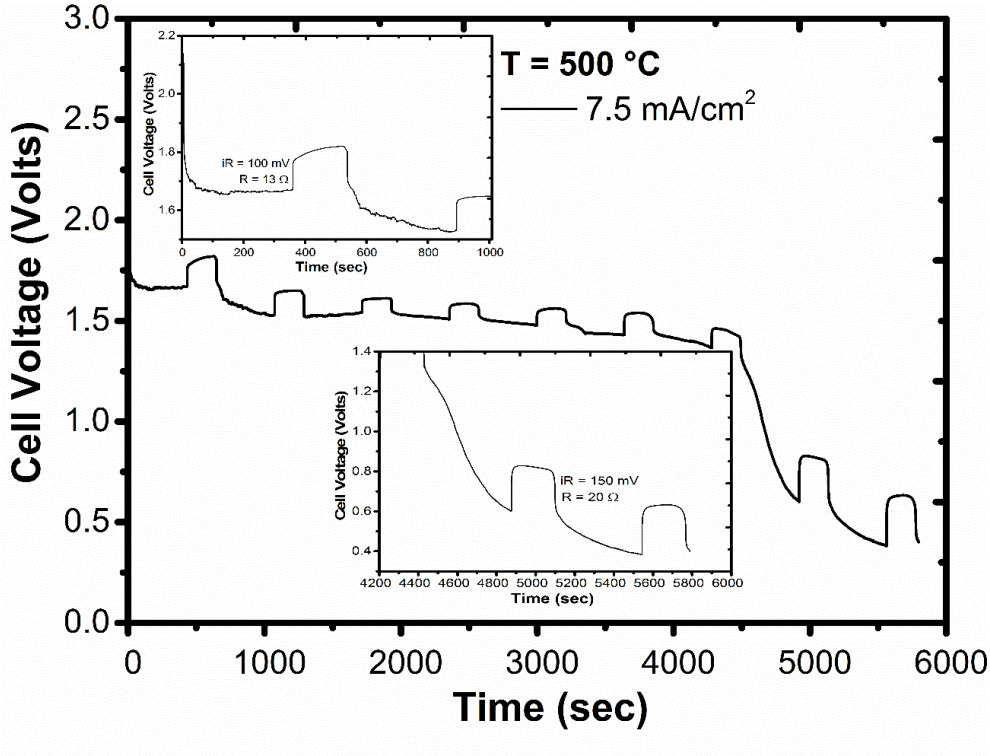

Figure 4.12. Galvanostatic intermittent titration technique applied to study of $NiCo_2S_4$ at a current density of 7.5 mA/cm^2 at 500 °C

For further understanding of the electrochemical processes occurring during discharge, the crystalline phases involved in the discharge process of $CoNi_2S_4$ and $NiCo_2S_4$ were probed using PXRD. PXRD data were collected from both the $CoNi_2S_4$ and $NiCo_2S_4$ cathodes after testing and are shown in Figures 4.13 and 4.14 [1].

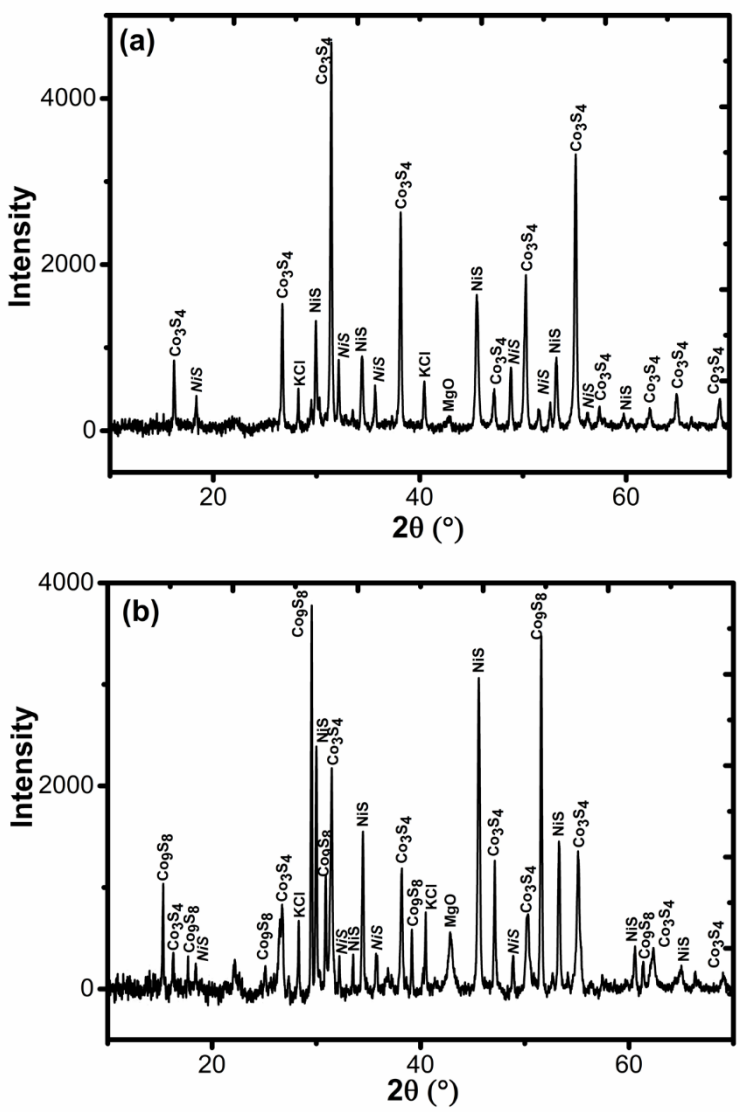

Figure 4.13. PXRD data collected at room temperature of the $CoNi_2S_4$ cathode following galvanostatic discharge at 500 °C (a) after stopping the discharge between the first and second plateaus and (b) at the end of the galvanostatic discharge. The crystalline phases have been labelled [1]

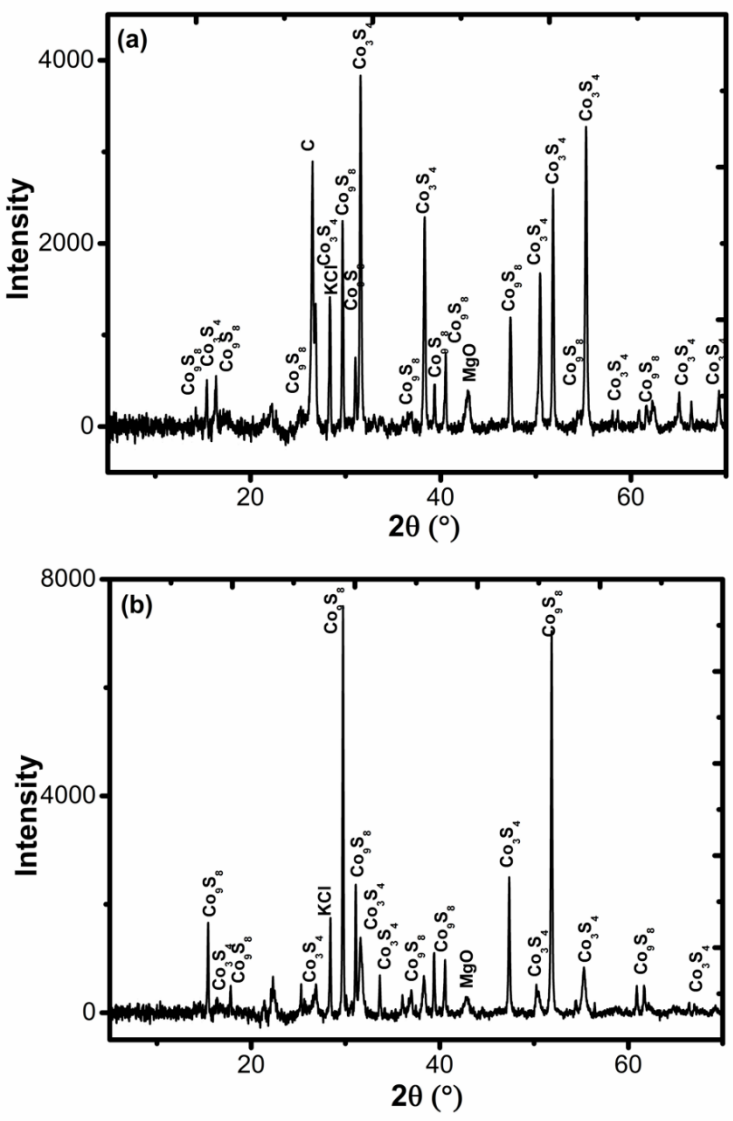

Figure 4.14. PXRD data collected at room temperature of the $NiCo_2S_4$ cathode following galvanostatic discharge at 500 °C (a) after stopping the discharge between the first and second plateaus and (b) at the end of the galvanostatic discharge. The crystalline phases have been labelled

As the electrochemical investigation of $CoNi_2S_4$ suggests that the first plateau corresponds to the electrochemical reaction

$$CoNi_2S_4 + 4/3\ Li \Rightarrow 1/3\ Co_3S_4 + 2\ NiS + 2/3\ Li_2S \quad [4.1]$$

and the second plateau of $CoNi_2S_4$ corresponds to the electrochemical reaction

$$Co_3S_4 + 8/3\ Li \Rightarrow 1/3\ Co_9S_8 + 4/3\ Li_2S \quad [4.2]$$

this could be confirmed by PXRD results after testing, as PXRD would allow the crystalline phases to be identified.

The PXRD data of $CoNi_2S_4$ between the first and the second plateaus (Figure 4.13a) show that there are several crystalline phases present which can be assigned to known crystalline phases in the PDF database. The following crystalline phases could be assigned to a hexagonal unit cell, with cell parameters (a = 3.47(4) Å, c = 5.35(4) Å), and space group $P6_3/mmc$ and suggests a NiS phase and not a CoS phase or other phases, as the values of unit cell are closer to the literature. Also some other peaks could be indexed to a rhombohedral unit cell, with cell parameters (a = 9.607(3) Å, c = 3.142(10) Å) and space group $R3m$ and suggests a *NiS* phase as well.

NiS exists in two phases, a high temperature hexagonal phase NiS and a low temperature rhombohedral phase *NiS*. This phase transformation takes place at 379 °C and is accompanied by a 4% volume change [13].

A cubic phase with space group $Fd\bar{3}m$ and unit cell (a = 9.402(20) Å) suggests a Co_3S_4 phase.

Therefore PXRD data indicate the formation of NiS and Co_3S_4 as the product of the electrochemical process after the first plateau in the discharge curve of $CoNi_2S_4$ [1].

PXRD data were also collected at the end of discharge of $CoNi_2S_4$ (Figure 4.13b) and data show a hexagonal NiS phase (a = 3.43(7) Å, c = 5.34(11) Å), a rhombohedral *NiS* phase (a = 9.615(8) Å, c = 3.147(4) Å) and also a cubic Co_9S_8 phase (a = 10.01(9) Å). The main phase present is Co_9S_8. However there are also peaks of Co_3S_4 and peaks of the KCl from the electrolyte and MgO from the separator. Although Li_2S is an expected product of the discharge process but PXRD data do not show Li_2S.

Therefore the formation of Co_9S_8 is the product of the electrochemical process at the end of the second plateau.

This PXRD data is in agreement with proposed equations [4.1] and [4.2] based on galvanostatic discharge [1].

In the case of $NiCo_2S_4$, the first plateau corresponds to the electrochemical reaction

$$NiCo_2S_4 + 2/3\ Li \Rightarrow 2/3\ Co_3S_4 + NiS + 1/3\ Li_2S \quad [4.3]$$

and the second plateau of $NiCo_2S_4$ corresponds to the electrochemical reaction

$$Co_3S_4 + 8/3\ Li \Rightarrow 1/3\ Co_9S_8 + 4/3\ Li_2S \quad [4.4]$$

The PXRD data of $NiCo_2S_4$ between the first and the second plateaus (Figure 4.14a) show that Co_3S_4 (a = 9.3914(18) Å, space group $Fd\bar{3}m$) and Co_9S_8 (a = 9.9714(14) Å, space group $Fm\bar{3}m$) were identified as crystalline products present after the first plateau of the electrochemical discharge.

PXRD did not show NiS or Li_2S. This could be due to overlap the Co_3S_4 and Co_9S_8 peaks with peaks of NiS. Therefore the PXRD data indicate the formation of Co_3S_4 as the product of the electrochemical process after the first plateau in the discharge curve of $NiCo_2S_4$.

PXRD data of $NiCo_2S_4$ were also collected at the end of discharge (Figure 4.14b) and show a cubic Co_9S_8 phase (a = 9.963(7) Å) and a cubic Co_3S_4 phase (a = 9.389(4) Å). Therefore the formation of Co_9S_8 is the product of the electrochemical process at the end of the second plateau of $NiCo_2S_4$.

This PXRD data is in agreement with proposed equations [4.3] and [4.4] based on the electrochemical reactions of $NiCo_2S_4$.

GITT results of $CoNi_2S_4$ and $NiCo_2S_4$ show that both cathodes have similar cell resistances at the beginning of the measurement (13 Ω) to the end of the measurement (20-23 Ω). GITT data of both cathodes also show in Figure 4.15 that the shape of the voltage ‘‘steps’’ (shown by red arrows) during the relaxation period differs during discharge and that could be explained by unique thermodynamics and kinetics procedures as phase formation or decomposition rather than a phase transformation take place during discharge as different phases have different equilibrium procedures [14].

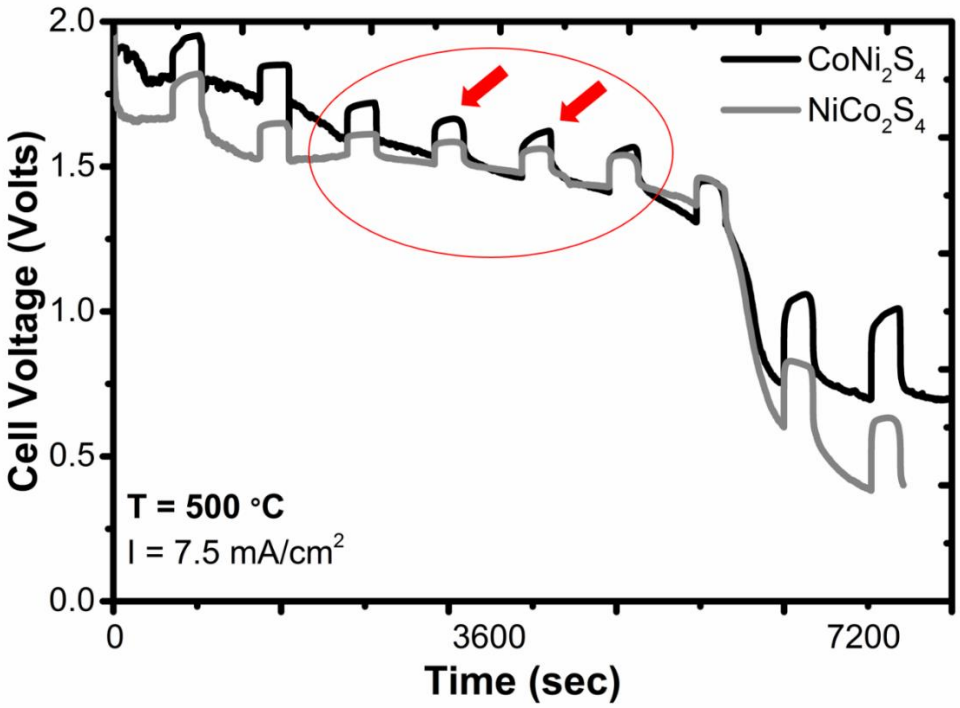

Figure 4.15. GITT data of both $CoNi_2S_4$ and $NiCo_2S_4$ at 500 °C at a current density of 7.5 mA/cm^2. Red arrows show the different shape of voltage ‘‘steps’’

4.3 **Summary**

$CoNi_2S_4$ and $NiCo_2S_4$ exhibit two electrochemical steps with capacities of 350 mA h g^{-1} and 290 mA h g^{-1} respectively. This is comparable to the capacities for the most commonly used sulfide based cathodes such as FeS_2, CoS_2 and NiS_2 which exhibit capacities of 558, 598 and 545 mA h g^{-1} respectively. However CoS_2 still exhibits a higher capacity as presented in Table 4.4.

$NiCo_2S_4$ has a lower voltage (1.70 V and 1.50 V) than $CoNi_2S_4$ (1.75 V and 1.50 V) against $Li_{13}Si_4$ at 500 °C and this might be explained by the different nickel/cobalt ratio or structure (normal spinel/inverse spinel) to the compounds. It is known that the voltage of a battery ranges of compounds consisting of transition metal ions [15]. There is a relationship between battery voltage and the number of electrons in the *d* orbitals of transition-metal ions. Moreover the voltage of the battery increases with increasing number of electrons in the *d* orbitals. Ni metal exhibits more electrons in the *d* orbitals than Co (d^8 and d^7, respectively). As a result the compound $CoNi_2S_4$ has higher voltage than $NiCo_2S_4$. However, $NiCo_2S_4$ has a greater lithium diffusion coefficient than $CoNi_2S_4$.

Also both have similar voltages with FeS_2, CoS_2 and NiS_2 vs Li-Al at 400 °C [16 -18] as shown in Table 4.5.

$CoNi_2S_4$ and $NiCo_2S_4$ have a similar behaviour (two electrochemical steps, similar voltage plateaus) to the most studied industrial cathodes so they are promising candidates for novel materials in Li thermal batteries. Further investigation of $CoNi_2S_4$ and $NiCo_2S_4$ may enable further enhancement of properties. For example the influence of particle size on the electrochemical process.

The work in Chapter 4 has been published titled as: *Synthesis and Electrochemical Study of $CoNi_2S_4$ as a Novel Cathode Material in a Primary Li Thermal Battery* at Journal of The Electrochemical Society [1].

Table 4.4. Capacities of $CoNi_2S_4$ and $NiCo_2S_4$ compared to FeS_2, CoS_2 and NiS_2

Sulfides	**Capacity (mA h g^{-1})**
FeS_2	558 [16]
CoS_2	598 [16] ~ 1.70 times more capacity than $CoNi_2S_4$
NiS_2	545 [16]
$CoNi_2S_4$	350
$NiCo_2S_4$	290

Table 4.5. Electrochemical reactions and voltages of $CoNi_2S_4$ and $NiCo_2S_4$ compared to FeS_2, CoS_2 and NiS_2. All FeS_2/CoS_2/NiS_2 voltages are versus Li-Al, $CoNi_2S_4$/$NiCo_2S_4$ voltages are versus Li-Si

Sulfides	**Voltage at 400 °C vs Li-Al (1st plateau)**	**Voltage at 400 °C vs Li-Al (2nd plateau)**	**Voltage at 400 °C vs Li-Al (3rd plateau)**	**Voltage at 400 °C vs Li-Al (4th plateau)**
FeS_2	$FeS_2 + 3/2\ Li \rightarrow ½\ Li_3Fe_2S_4$ (*1.75 V)*	$Li_3Fe_2S_4 + Li \rightarrow Li_2FeS_2 + FeS + Li_2S$ (*1.64 V)*	$Li_2FeS_2 \rightarrow Fe + Li_2S + S$ (*1.26 V)*	-
CoS_2	$CoS_2 + 4/3\ Li \rightarrow 1/3\ Co_3S_4 + 2/3\ Li_2S$ (*1.70 V)*	$Co_3S_4 + 8/3\ Li \rightarrow 1/3\ Co_9S_8 + 4/3\ Li_2S$ (*1.64 V)*	$Co_9S_8 + 16\ Li \rightarrow 9\ Co + 8\ Li_2S$ (*1.37 V)*	-
NiS_2	$NiS_2 + 2\ Li \rightarrow NiS + Li_2S$ (*1.74 V)*	$7\ NiS + 2\ Li \rightarrow Ni_7S_6 + Li_2S$ (*1.58 V)*	$3\ Ni_7S_6 + 8\ Li \rightarrow 7\ Ni_3S_2 + 4\ Li_2S$ (*1.55 V)*	$Ni_3S_2 + 4\ Li \rightarrow 3\ Ni + 2\ Li_2S$ (*1.36 V)*
	Voltage at 500 °C vs Li-Si (1st plateau)	**Voltage at 500 °C vs Li-Si (2nd plateau)**	**Voltage at 500 °C vs Li-Si (3rd plateau)**	**Voltage at 500 °C vs Li-Si (4th plateau)**
$CoNi_2S_4$	$CoNi_2S_4 + 4/3\ Li \rightarrow 1/3\ Co_3S_4 + 2\ NiS + 2/3\ Li_2S$ (*1.75 V)*	$Co_3S_4 + 8/3\ Li \rightarrow 1/3\ Co_9S_8 + 4/3\ Li_2S$ (*1.50 V)*	-	-
$NiCo_2S_4$	$NiCo_2S_4 + 2/3\ Li \rightarrow 2/3\ Co_3S_4 + NiS + 1/3\ Li_2S$ (*1.70 V)*	$Co_3S_4 + 8/3\ Li \rightarrow 1/3\ Co_9S_8 + 4/3\ Li_2S$ (*1.50 V)*	-	-

4.4 **References**

[1] Kyriakos Giagloglou *et al.*, *Journal of the Electrochemical Society,* 164, (9) (2017), A1-A5

[2] Sowa H. *et al.*, *Physics and Chemistry of Minerals,* 31, (2004), 321-327

[3] Shang Fei *et al.*, *Rengong Jingti Xuebao,* 37, (4) (2008), 936-941

[4] Huang Chunghis *et al.*, *Canadian Journal of Chemistry,* 49, (1971), 598-602

[5] Knop O. *et al.*, *Canadian Journal of Chemistry*, 46, (1968), 3463-3476

[6] L. Mancic *et al.*, *Nanophased Powder, Sensors,* 3, (2003), 415-423

[7] K. Matsuda *et al.*, *Materials Transactions,* 47, (7) (2006), 1815-1820

[8] Varley F.S., *Neutron News,* 3, (3) (1992), 29-37

[9] Vaughan D.J. *et al.*, *American Mineralogist,* 70, (9) (1985), 1036-1043

[10] Lundqvist D. *et al.*, *Zeitschrift fuer Anorganische und Allgemeine Chemie,* (1950) (DE) 239 (1938), 85-88

[11] *https://www.webelements.com*

[12] R.D. Shannon, *Acta Crystallographica A,* 32, (1976), 751-767

[13] Sparks J.T. *et al.*, *Journal of Applied Physics,* 39, (1968), 715

[14] Yujie Zhu *et al.*, *Journal of Physical Chemistry C,* 114 (2010), 2830-2841

[15] J.K. Park, *Principles and Applications of Lithium Secondary Batteries*, Wiley-VCH Germany, (2012)

[16] S.K. Preto *et al., Journal of the Electrochemical Society,* 130, (1983), 264

[17] P.J. Masset *et al., Journal of Power Sources,* 177, (2008), 595-609

[18] P.J. Masset *et al.*, *Journal of Power Sources,* 178, (2008), 456-466

Chapter 5: Zirconium Sulfide Cathodes

Chapter 5: Zirconium Sulfide Cathodes

5.1 Material Characterisation of Zirconium Sulfides

5.1.1 ZrS_3

ZrS_3 has a pseudo one-dimensional structure as shown in Figure 5.1 and Zr atoms occupy the center of a trigonal prism with sulfur atoms at the corners and two of those S atoms bond to each other. Neighboring atoms create an infinite chain along the *b*-axis of the crystal [1]. These chains stack to form corrugated layers perpendicular to *c*-axis.

The synthesis of ZrS_3 has previously been reported by many authors [2-5] and their solid state synthesis involves multiple firings at temperatures from 600 °C to 1000 °C for almost 1 month. This work improved the synthesis of ZrS_3, in synthesizing the sample in shorter time using only one firing step for 1 week.

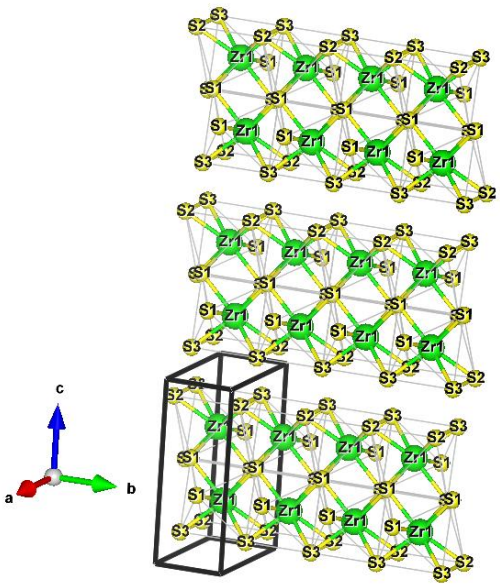

Figure 5.1. Crystal structure of ZrS_3. Yellow atoms are sulfur, green atoms are zirconium [6]

Zirconium trisulfide was studied by powder X-ray diffraction in both reflection and transmission geometry and results are presented in Figures 5.2 and 5.3. ZrS_3 was identified as a single phase and could be indexed to the $P2_1/m$ unit cell reported by Furuseth *et al.* Cell parameters are given in Table 5.1.

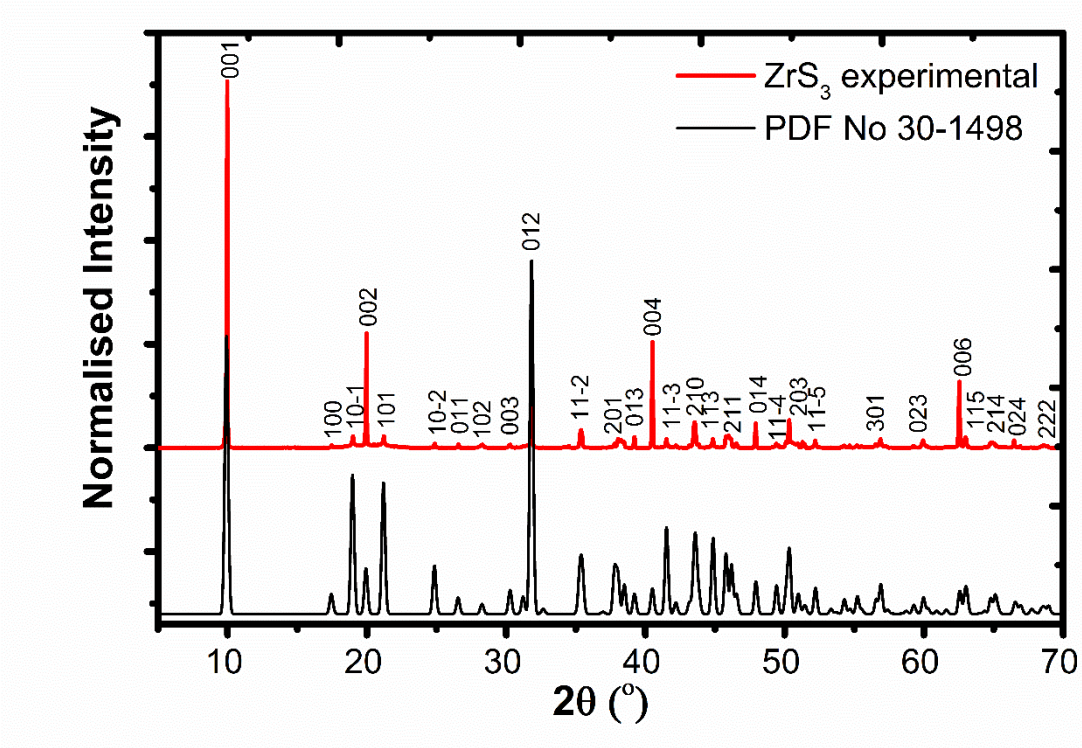

Figure 5.2. PXRD data (Cu radiation) of ZrS_3 (reflection) (red line) [6] compared to the simulated diffraction pattern using the published crystallographic model [2] (black line)

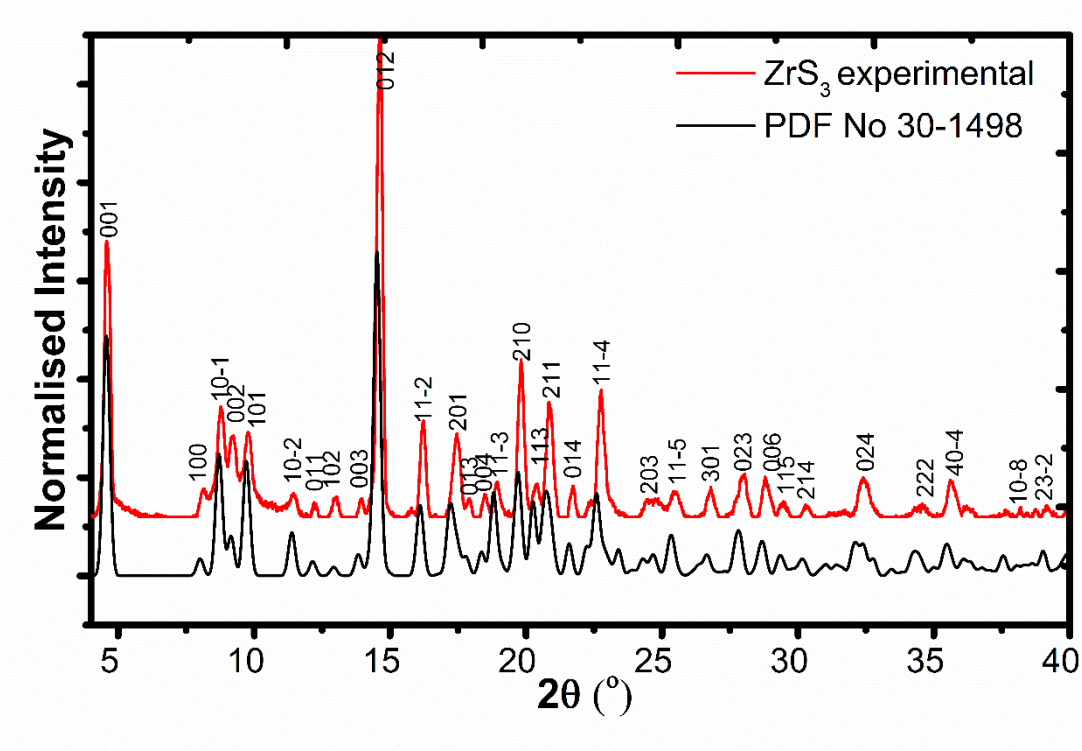

Figure 5.3. PXRD data (Mo radiation) of ZrS_3 (transmission geometry in a capillary) (red line) [6] compared to the simulated diffraction pattern using the published crystallographic model [2] (black line)

Table 5.1. Refined unit cell parameters of ZrS_3

Unit cell [Å]	**Experimental [6]**	**Literature [2]**
α	5.125(5)	5.124
b	3.625(4)	3.624
c	8.981(10)	8.980
β [°]	97.29(8)	97.28
Cell Volume [Å^3]	165.53(21)	165.44

The experimental intensity of ZrS_3 on the diffraction pattern from reflection, as the sample was pressed into a bulk flat plate sample holder, is different from the intensities in the simulated diffraction pattern in Figure 5.2. However, the collection of data in a quartz capillary from orientation allow much better sampling of intensities as shown in Figure 5.3. As a result the needle-like shape of the ZrS_3 crystals results in a large effect on the diffraction pattern from preferred orientation. The shape also of the ZrS_3 crystals means a high surface area which could enable lithium ion diffusion in the thermal battery at high temperatures and this could be confirmed at a later stage by the high capacity of 357 mA h g^{-1} [6].

In order to explore the thermal stability of ZrS_3 at elevated temperature, PXRD data were collected *in situ* at temperatures in the range from 25 °C to 500 °C as shown in Figure 5.4. Throughout this temperature range ZrS_3 is stable and there are no phase transformations or apparent degradation. The volume of the unit cell and the thermal expansion coefficient increase as the temperature increases as shown in Figure 5.5 [6].

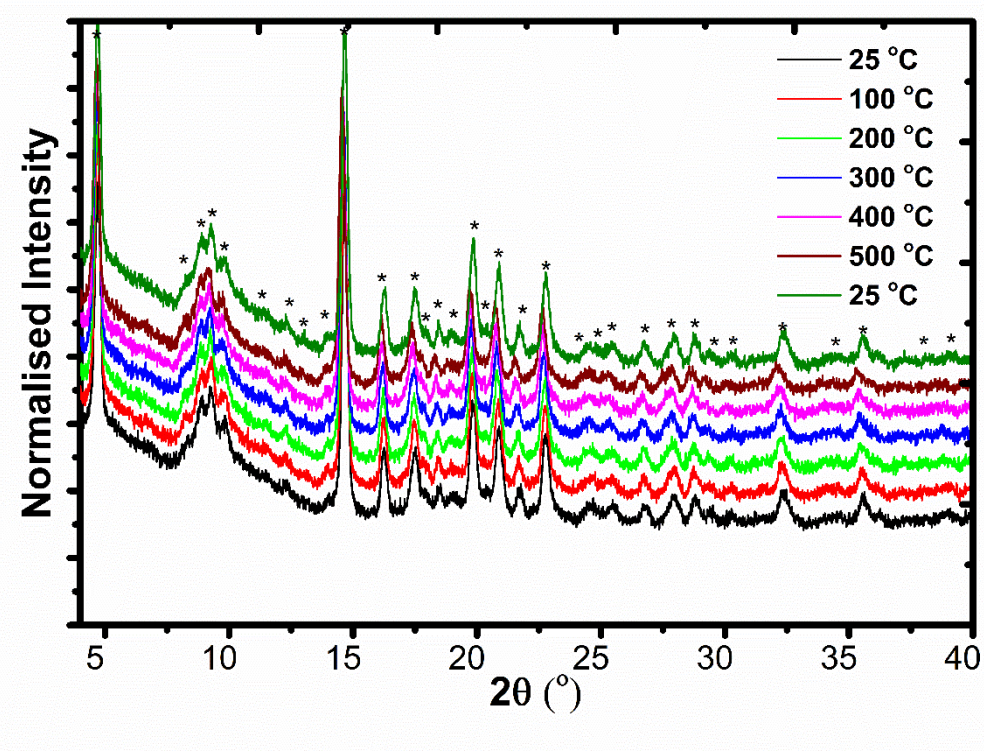

Figure 5.4. Variable temperature PXRD data (Mo radiation) of ZrS_3 at temperatures from 25 °C up to 500 °C [6]

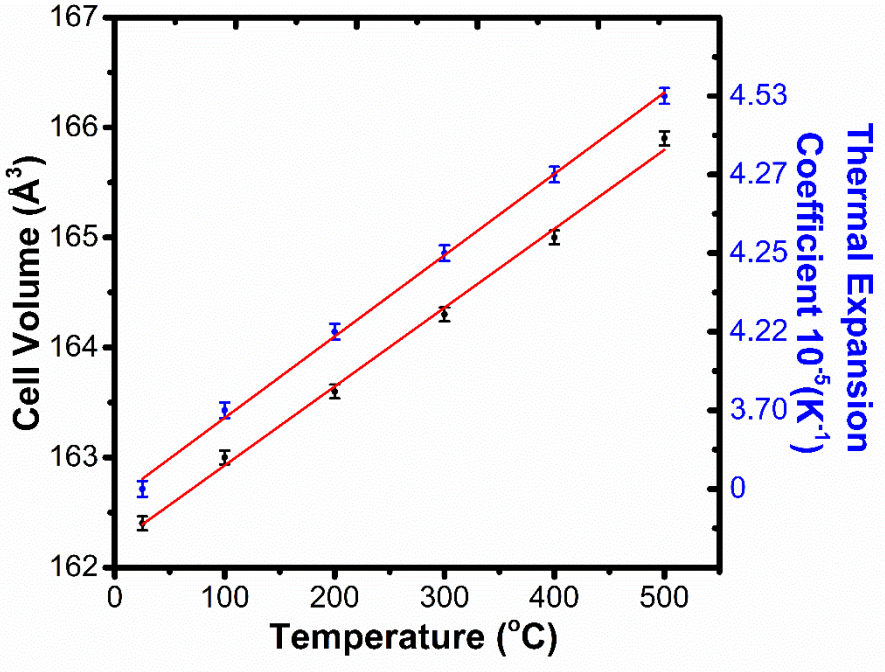

Figure 5.5. Cell volume and thermal expansion coefficient of ZrS_3 vs temperature from 25 °C up to 500 °C [6]

The morphology and the shape of crystallites of ZrS_3 was investigated by SEM and are presented in Figure 5.6. Crystallites of ZrS_3 have a uniform morphology, which is consistent with a single phase sample and the crystallites are needles. EDX analysis confirms the average elemental composition of ZrS_3 with zirconium 25 $\pm$3 at% and sulfur 75 $\pm$3 at% [6]. This elemental analysis is in agreement with the phase diagram of Zr - S system as shown in Figure 5.7. The melting point of ZrS_3 is 1150 °C [7].

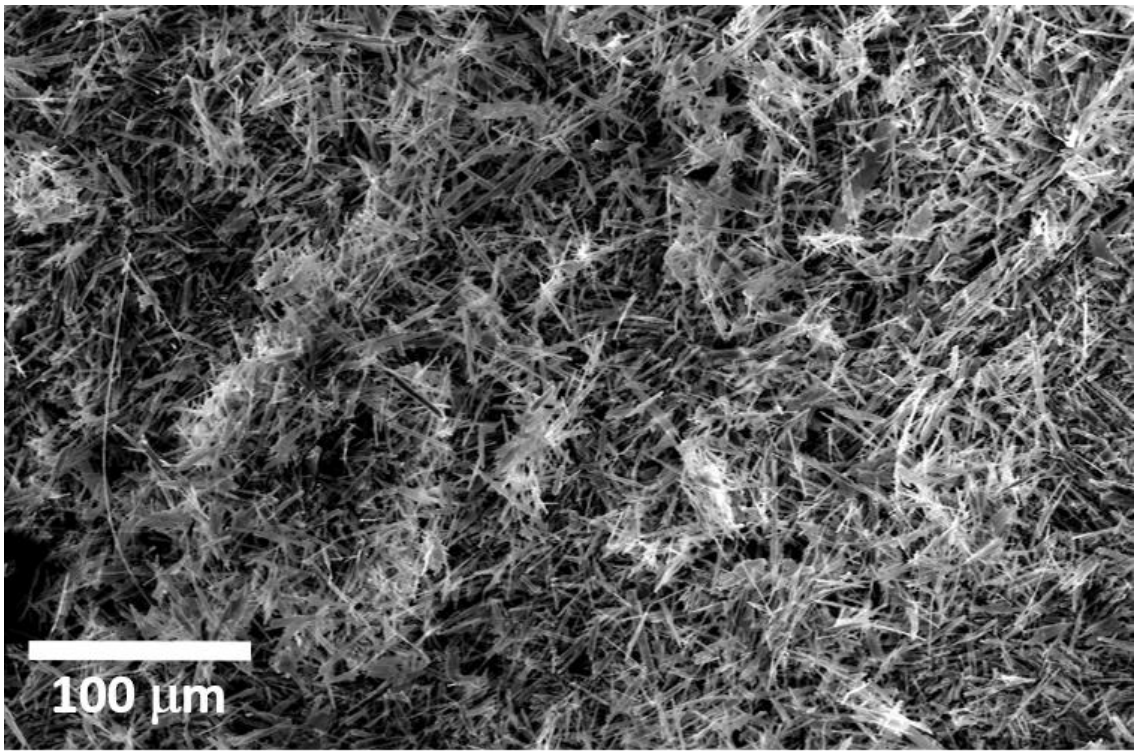

Figure 5.6. SEM image of ZrS_3 [6]

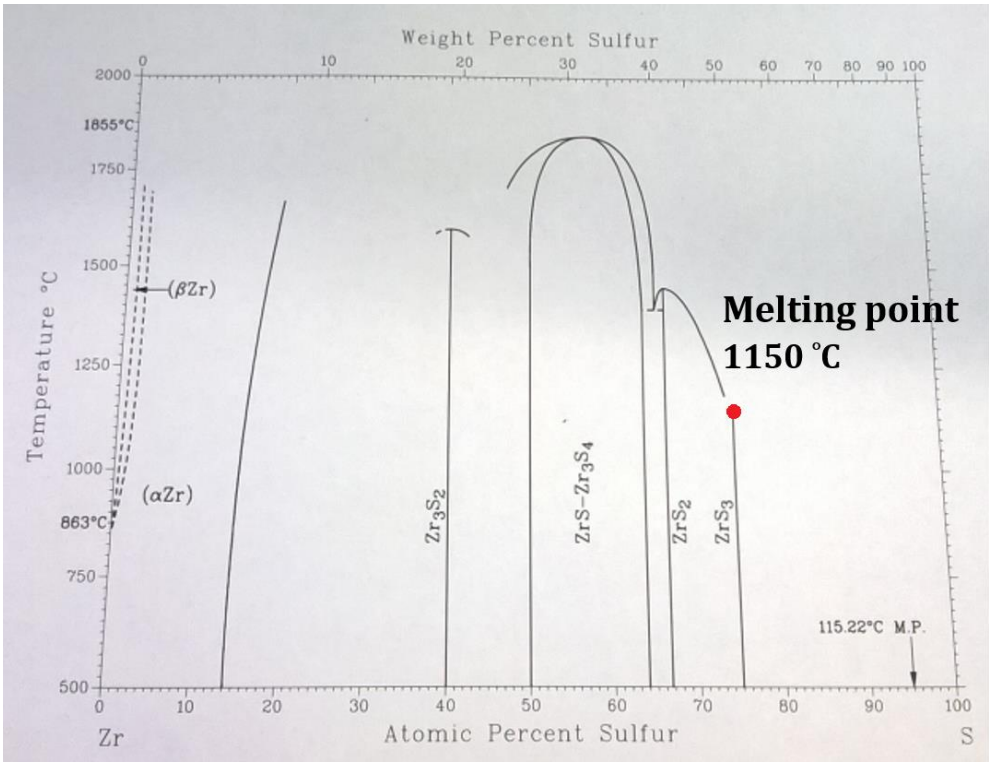

Figure 5.7. Phase diagram of Zr - S system

(permission by J. Rasneur and F. Marion) [7]

To investigate the thermal stability of ZrS_3 even further, a quantity of ZrS_3 was heated to 700 °C at 6 °C min^{-1} and was held at this temperature for 1 hour under flowing argon. Then the sample was cooled to room temperature at 6 °C min^{-1}. The resulting diffraction pattern is presented in Figure 5.8 and the PXRD data shows that ZrS_3 had decomposed to ZrS_2.

ZrS_2 crystallises in space group $P\bar{3}m1$ with refined unit cell parameters $a = b =$ 3.6631(4) Å, c = 5.8331(5) Å and this is in agreement with Fotouhi [8]. The mass of ZrS_3 before heating was 159 mg and it lost a mass of 43 mg after heating to 700 °C. This mass loss of 27 % is consistent with the thermal decomposition of ZrS_3 to ZrS_2 and gaseous sulfur at high temperatures [6].

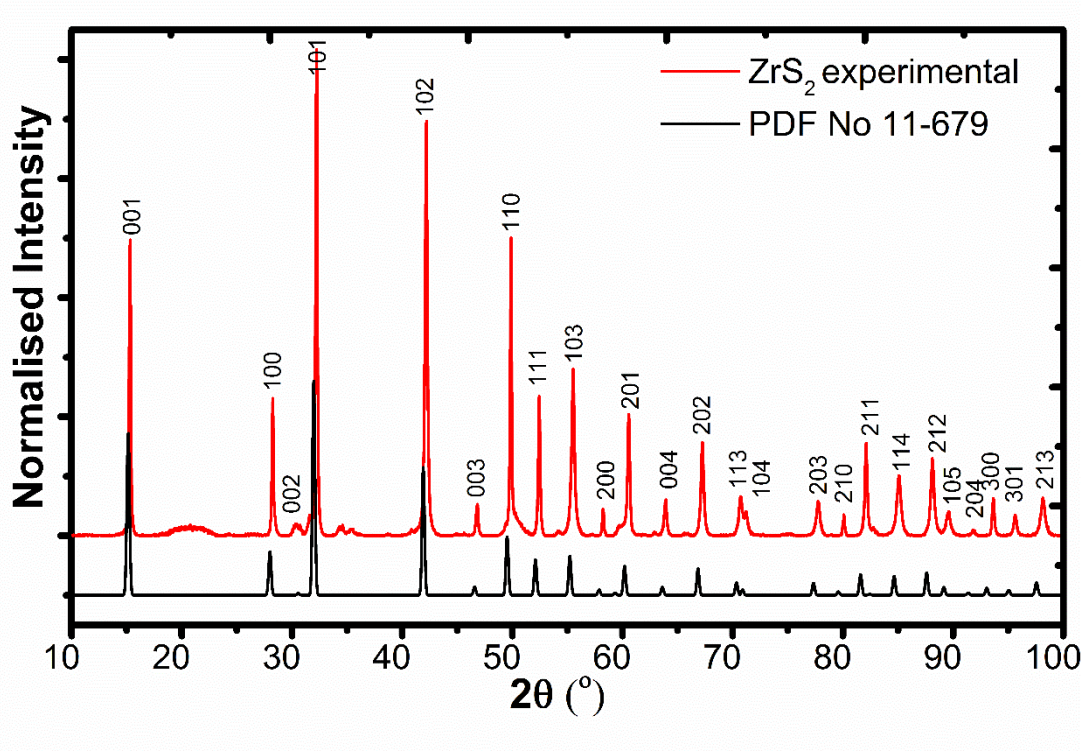

Figure 5.8. PXRD data (Cu radiation) of thermal decomposition of ZrS_3 to ZrS_2 (red line) [6] compared to the simulated diffraction pattern using the published crystallographic model [8] (black line)

5.2 **Electrochemical Investigation of Zirconium Sulfides**

5.2.1 **ZrS_3**

ZrS_3 was characterised electrochemically by galvanostatic discharge and galvanostatic intermittent titration technique.

The galvanostatic discharging of ZrS_3 at 500 °C is presented in Figure 5.9. ZrS_3 was discharged at different current densities from 7.5 to 75 mA/cm^2 to investigate the performance and the resulting discharge profiles. The voltage cut-off for this measurement was 1 Volt.

At both current densities of 7.5 and 11 mA/cm^2 there was a single flat voltage plateau at around 1.70 V and a capacity of 357 mA h g^{-1} was achieved (x = 2.5 Li) [6].

At current densities of 15, 19 and 23 mA/cm^2, the single flat voltage plateau is lower than 1.70 V as the cell resistance might be higher, however the capacity is still high (over 300 mA h g^{-1}) and x = 2.25 Li.

At a current density of 75 mA/cm^2 the single plateau is around 1.25 V and a capacity of around 200 mA h g^{-1} was achieved, (x = 1.5 Li).

The amount of active anode (0.15 g) corresponds to 73 mA h for the discharge plateau from $Li_{13}Si_4$ to Li_7Si_3 which is 0.157 V vs Li. The measured capacity of the cathode is 54 mA h which keeps the discharge as being performed against the 0.157 V Li plateau.

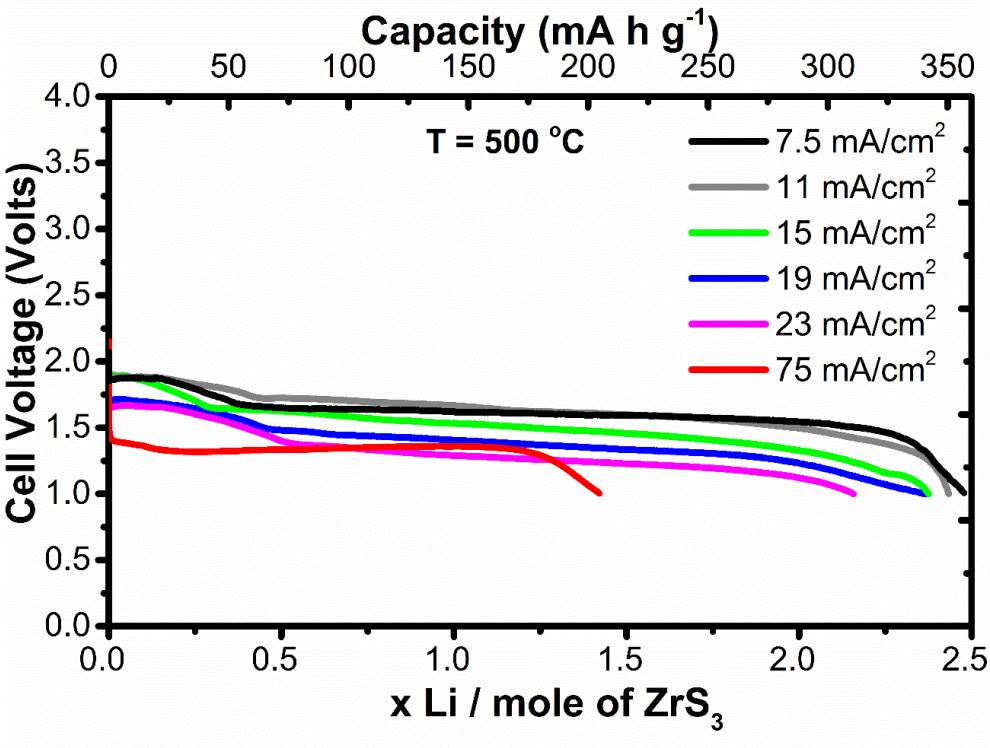

Figure 5.9. Galvanostatic discharge of ZrS_3 at current densities of 7.5 to 75 mA/cm^2 at 500 °C [6]

GITT results of ZrS_3 at a current density of 7.5 mA/cm^2 at 500 °C are presented in Figure 5.10. The voltage drops between the current pulses and the relaxation time until a voltage of 1 V is reached. The IR drop is 50 mV at the beginning of discharge and 125 mV at the end of the measurement, which indicates that the cell resistance is increasing during the reduction of the cathode, from a resistance of around 6 Ω at the beginning of the measurement to around 16 Ω after the cell discharge [6].

The chemical diffusion coefficient D = 4.12 10^{-5} cm^2 s^{-1} for ZrS_3 can be calculated from equation [3.1] where n_m = 0.00106 (mol), V_m = 49.84 (cm^3 / mol), ΔE_s = 0.070 (V) and ΔE_t = 0.020 (V).

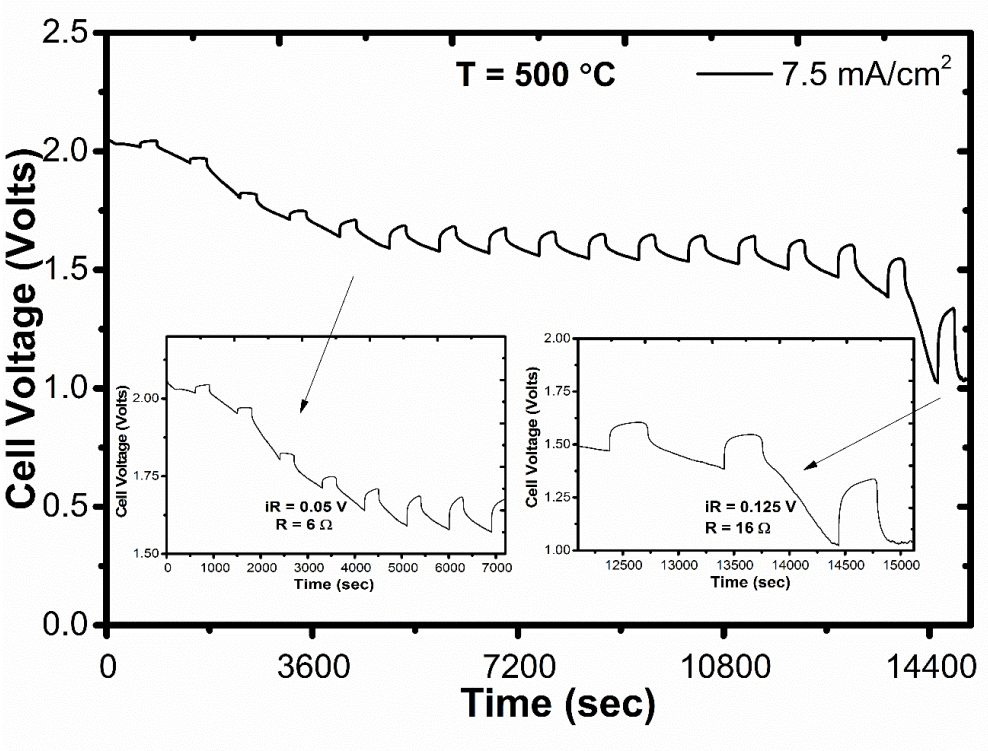

Figure 5.10. Galvanostatic intermittent titration technique of ZrS_3 at current density of 7.5 mA/cm^2 at 500 °C [6]

For further understanding to electrochemical investigation of ZrS_3, PXRD data and EDX analysis was carried out as shown in Figures 5.11 and 5.12.

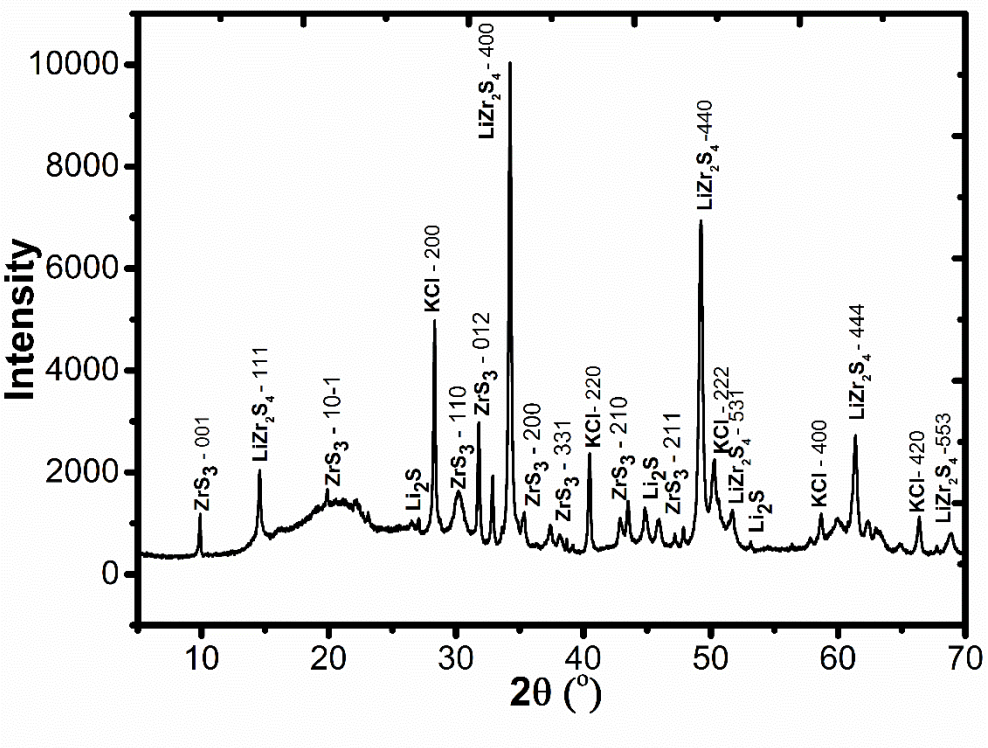

Figure 5.11. PXRD data of the cathode electrode after discharge. There are some peaks from the starting material ZrS_3, some peaks of the electrolyte KCl and some sharp peaks of the new cubic phase $LiZr_2S_4$ [6]

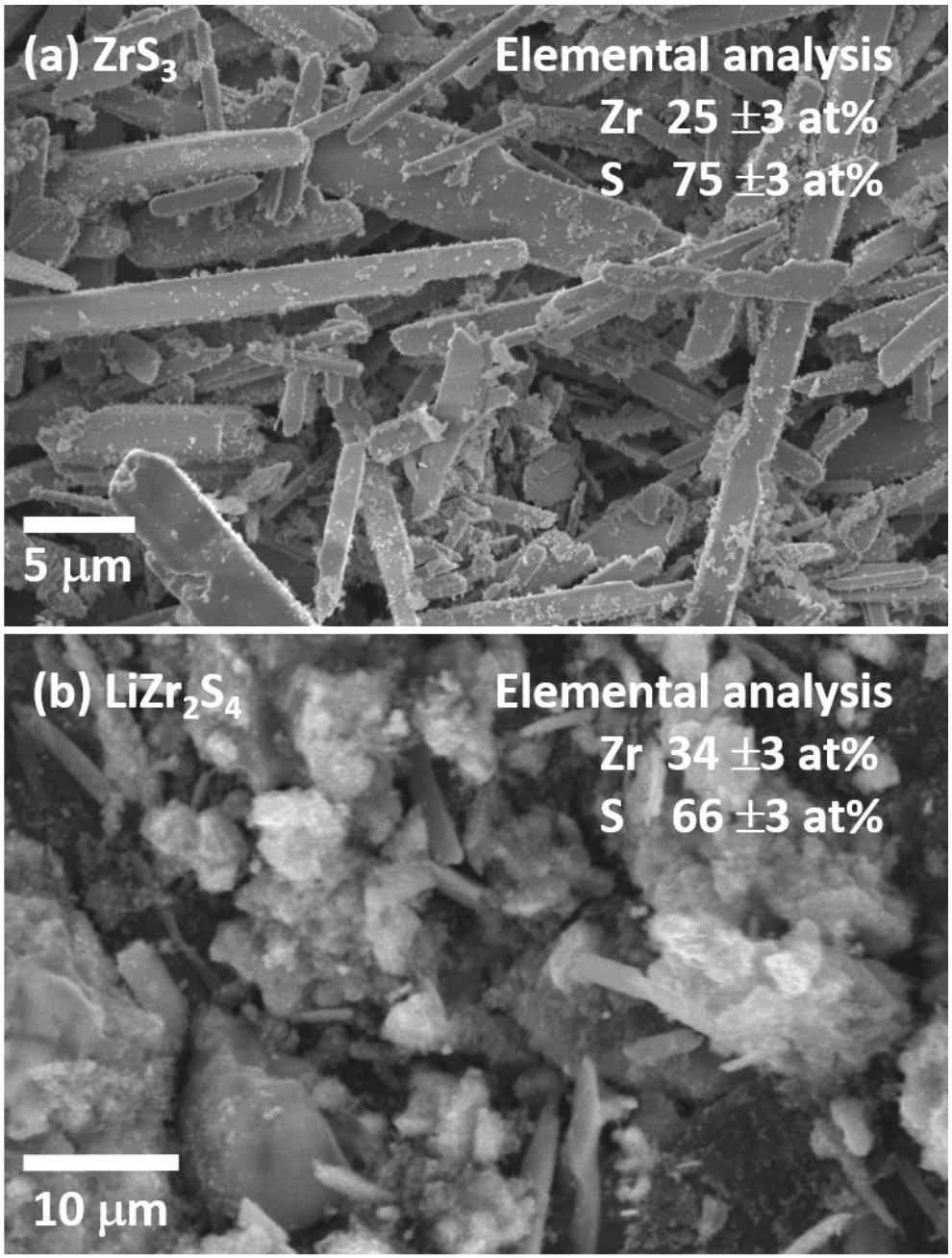

Figure 5.12. SEM image of cathode electrode before (a) and after (b) discharge [6]

ZrS_3 has an orange/red color as shown in Figure 3.1, so 25 wt% Super P Carbon was added to the cathode electrode to increase the electronic conductivity of the sample. According to the electrochemical process in Figure 5.9 the result is

$$2ZrS_3 + 5Li \Rightarrow 2Li_2S + LiZr_2S_4 \quad [5.1]$$

This result is in agreement with PXRD data and SEM/EDX analysis of the cathode after testing.

PXRD data were collected on the cathode after discharge and the diffraction pattern shows peaks from a number of different phases due to the difficulty in separating the cathode from the electrolyte/separator after battery testing as shown in Figure 5.11.

On the diffraction pattern there are a number of peaks which could not be assigned to any known crystalline phase in the PDF database. These peaks could be indexed to a cubic unit cell, with cell parameters a = 10.452(8) Å and space group $Fd\bar{3}m$ and suggests a spinel structure, which means a new phase with a cubic structure forms during discharge.

The SEM image of the cathode after electrochemical testing shows that the crystallites are not needles, indicating a morphology very different to that observed before electrochemical testing. EDX analysis can confirm a new phase with a composition of zirconium 34 $\pm$3 at% and sulfur 66 $\pm$3 at% as shown in Figure 5.12 [6].

5.3 **Summary**

In the past a low temperature $Li_{0.5}ZrS_2$ phase was formed by Li insertion to ZrS_2 with a different polymorph structure [9].

Compared to MS_2 cathodes such as FeS_2, NiS_2 or CoS_2, the ZrS_3 has a good voltage profile, a good thermal stability, a high capacity of 357 mA h g^{-1} and most importantly a single flat voltage plateau at 1.70 V vs $Li_{13}Si_4$ at 500 °C. These properties of ZrS_3 are suitable for thermal battery applications.

Moreover, the Table 5.2 shows the comparison of thermal stability, capacity, lithiated products and voltages of ZrS_3 to the transition metal disulfides.

Table 5.2. Thermal stability, capacity, lithiated products or not, and voltages of ZrS_3 compared to FeS_2, CoS_2 or NiS_2

Sulfides	**Capacity (mA h g^{-1})**	**Thermal decomposition**	**Products and Voltages against $Li_{13}Si_4$ at 500 °C**
FeS_2	558 [10]	FeS_2 => FeS + ½ S_2 at 580 °C [11 - 12]	$Li_3Fe_2S_4$ at 1.77 V Li_2FeS_2 at 1.64 V Fe at 1.13 V [15]
CoS_2	598 [10]	3 CoS_2 => Co_3S_4 + S_2 at 650 °C [13]	Co_3S_4 at 1.75 V Co_9S_8 at 1.40 V Co at 1.25 V [15]
NiS_2	545 [10]	NiS_2 => NiS + ½ S_2 at 600 °C [14]	NiS at 1.76 V Ni_7S_6 at 1.60 V Ni_3S_2 at 1.40 V Ni at 1.25 V [15]
ZrS_3	357[6]	ZrS_3 => ZrS_2 + ½ S_2 at 700 °C [6]	$LiZr_2S_4$ at 1.70 V [6]

The work in Chapter 5 has been published titled as: *Zirconium Trisulfide as a Promising Cathode Material for Li Primary Thermal Batteries* at Journal of The Electrochemical Society [6].

5.4 **References**

[1] S. Srivastava *et al.*, *Journal of Materials Science,* 27 (1992), 3693-3705

[2] Furuseth S. *et al.*, *Acta Chemica Scandinavica Series A,* (28, 1974) (29, 1975), 623-631

[3] S.G. Patel *et al.*, *Physica Status Solidi,* A, 140 (1993), 207

[4] W. Schairer *et al.*, *Physica Status Solidi,* A, 17 (1973), 181

[5] F. Levy *et al.*, *Journal of Crystal Growth,* 61 (1983), 61

[6] Kyriakos Giagloglou *et al.*, *Journal of the Electrochemical Society,* 163, (14) (2016), A3126-A3130

[7] J. Rasneur *et al.*, *Comptes Rendus Chimie*, 280 (1975), 301-304

[8] Sieber K. Fotouhi, *Materials Research Bulletin,* 18 (1983), 1477-1484

[9] J.R. Levy-Clement *et al.*, *Solid State Communications,* 50, (2) (1984), 101-104

[10] S.K. Preto *et al.*, *Journal of the Electrochemical Society,* 130 (1983), 264

[11] M.C. Hash *et al.*, *Proceedings of the 8th International Symposium on Molten Salts*, (1992), 228

[12] I.C. Hoare *et al.*, *Journal of the Chemical Society Faraday Transactions*, 184, (9) (1988), 3071

[13] H. Rau, *Journal of Physics and Chemistry Solids*, 37 (1976), 931

[14] R.A. Guidotti *et al.*, *Proceedings of the 40th Power Sources Conference*, (2002), 250

[15] Patrick J.M. *et al.*, *Journal of Power Sources,* 178 (2008), 456-466

Chapter 6: Transition Metal Chloride Cathodes

Chapter 6: Transition Metal Chloride Cathodes

6.1 Material Characterisation of Transition Metal Chlorides

6.1.1 $KNiCl_3$

$KNiCl_3$ was analysed by powder X-ray diffraction and the resulting diffraction pattern is presented in Figure 6.1. $KNiCl_3$ was identified as the main phase but there is also a KCl impurity (a = 6.280(25) Å) from the starting material, which did not react during the synthesis. $KNiCl_3$ crystallises in hexagonal perovskite $P6_3mc$ with cell dimensions ($a = b$ = 11.800(11) Å and c = 5.926(4) Å) as shown in Figure 6.2. $NiCl_6$ face-sharing octahedra form linear chains along the c-axis and they are also arranged triangularly in the ab-plane. The face-sharing octahedra compared to corner-sharing octahedra provide 3D structure and better conductivity. This is due to the fact that in the case of face-sharing octahedra conductivity is improved by closer metal-metal distances. The phase diagram, as shown in Figure 6.3, shows that the melting point of $KNiCl_3$ is 645 °C [1 - 2].

$KNiCl_3$ exhibits two structural phase transitions during cooling to room temperature, according to the literature [3 - 5]. The first phase transition takes place at 490 °C and the second one takes place at 287 °C. The first phase is hexagonal and the second phase is orthorhombic. However, in our experiments with respect this phase transition could not be obtained.

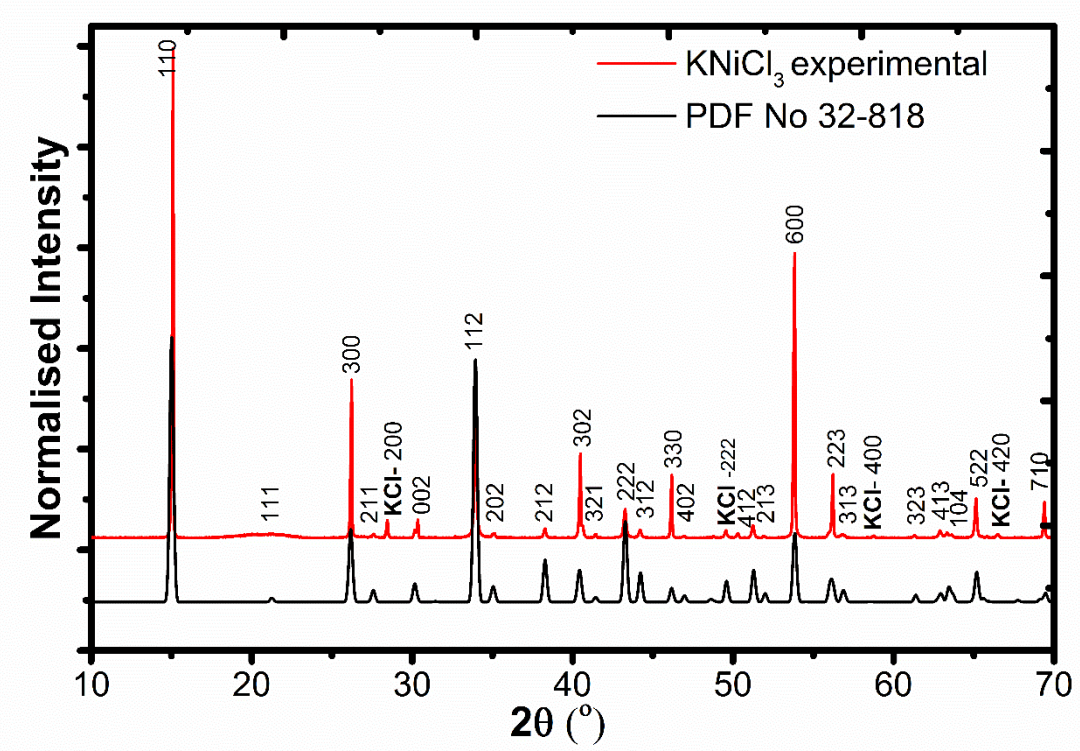

Figure 6.1. PXRD data of $KNiCl_3$ at room temperature. Experimental pattern is shown by the red line and the simulated diffraction pattern using published crystallographic model [6] is shown by the black line. Impurity is KCl

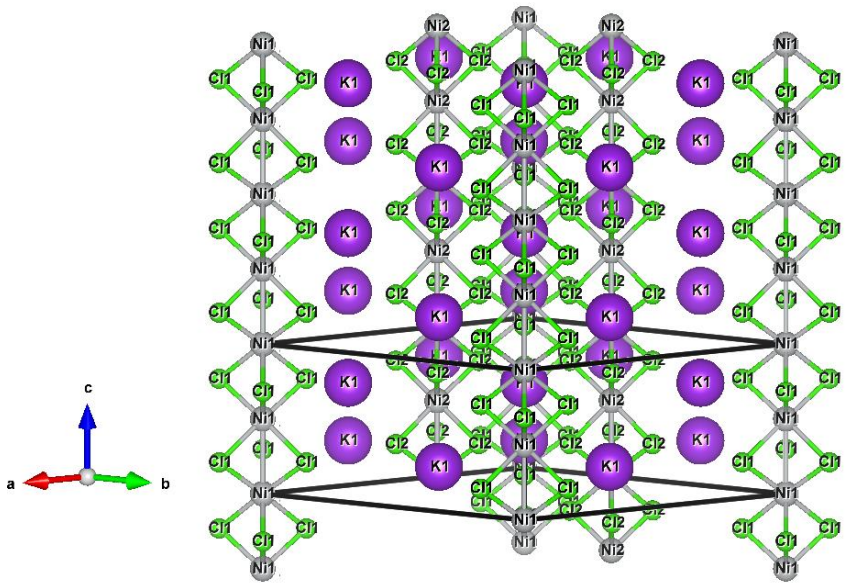

Figure 6.2. Crystal structure of $KNiCl_3$. Purple atoms are potassium, green atoms are chlorine, grey atoms are nickel

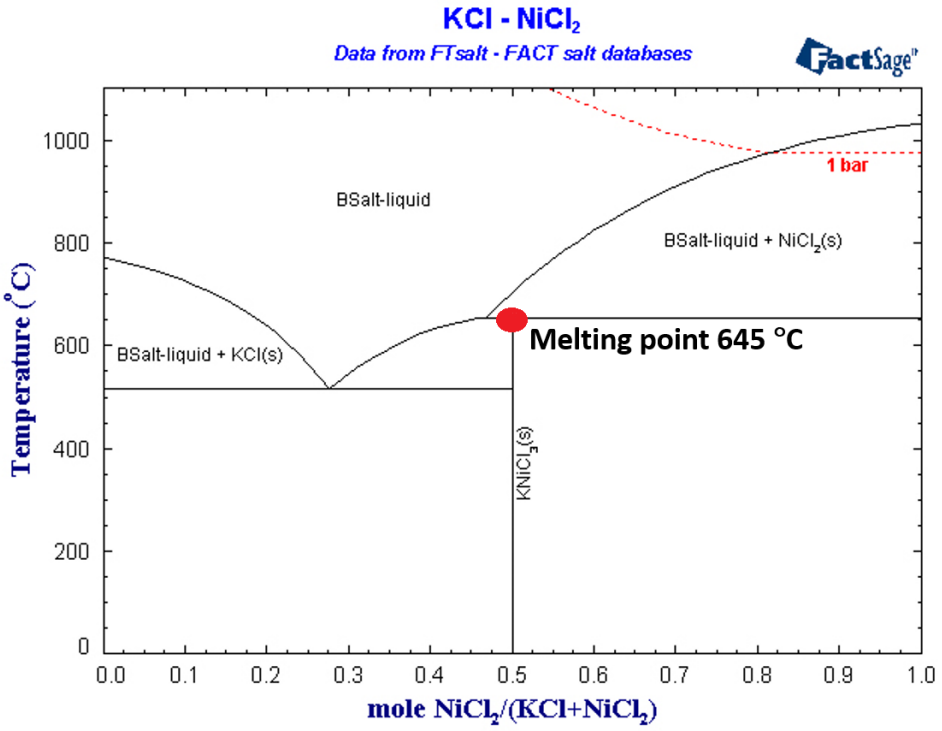

Figure 6.3. Phase diagram of $NiCl_2$ – KCl system [1-2]

The morphology of $KNiCl_3$, before and after discharge, was studied by SEM as shown in Figures 6.4a and 6.4b. The size of the crystallites is bigger than 50 μm before testing and smaller than 50 μm after the discharge. EDX confirms K 19 ±1 at%, Ni 19 ±1 at% and Cl 62 ±1 at% as expected for $KNiCl_3$ before it being tested as a cathode in a Li thermal battery as shown in Figure 6.4a. The elemental analysis of $KNiCl_3$ cathode electrode after testing is K 14 ±2 at%, Ni 5 ±2 at% and Cl 81 ±2 at% (Figure 6.4b) and this means that the metals have been reduced, producing species such as Ni metal, KCl and LiCl. These products will be investigated at a later stage by powder X-ray diffraction.

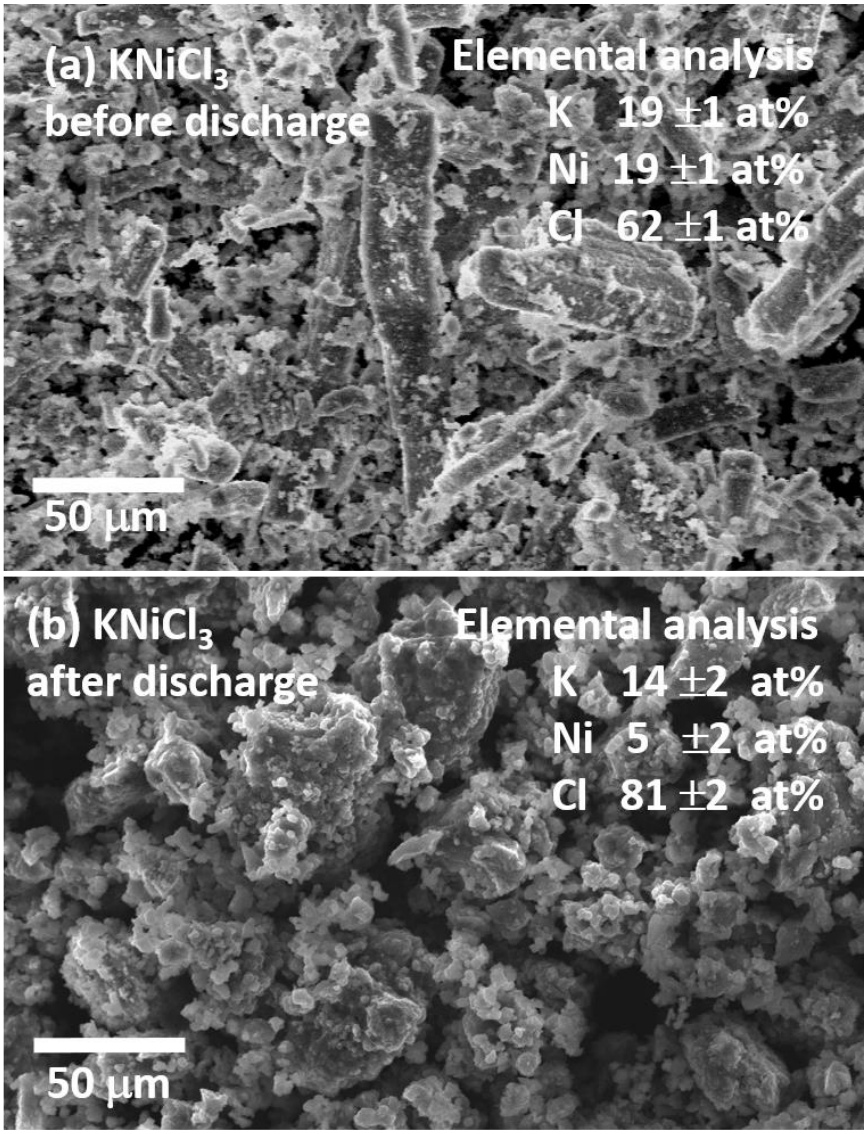

Figure 6.4. SEM images of $KNiCl_3$ before (a) and after (b) discharge

6.1.2 **Li_2MnCl_4**

Li_2MnCl_4 was analysed by powder X-ray diffraction and the diffraction pattern is shown in Figure 6.5. Li_2MnCl_4 was identified as the main phase but there is also a LiCl impurity (a = 5.140(10) Å) from the starting material, which did not react during the synthesis. Li_2MnCl_4 crystallises in cubic $Fd\bar{3}m$ with unit cell parameters (a = 10.495(7) Å), as shown in Figure 6.6. Li_2MnCl_4 adopts an inverse spinel structure with half of the lithium ions tetrahedrally coordinated by chlorine ions and the remaining Li atoms, together with the Mn ions, are distributed statistically over the occupied octahedral sites [7 - 8]. The phase diagram, as shown in Figure 6.7, shows the melting point of Li_2MnCl_4 at 575 °C [9].

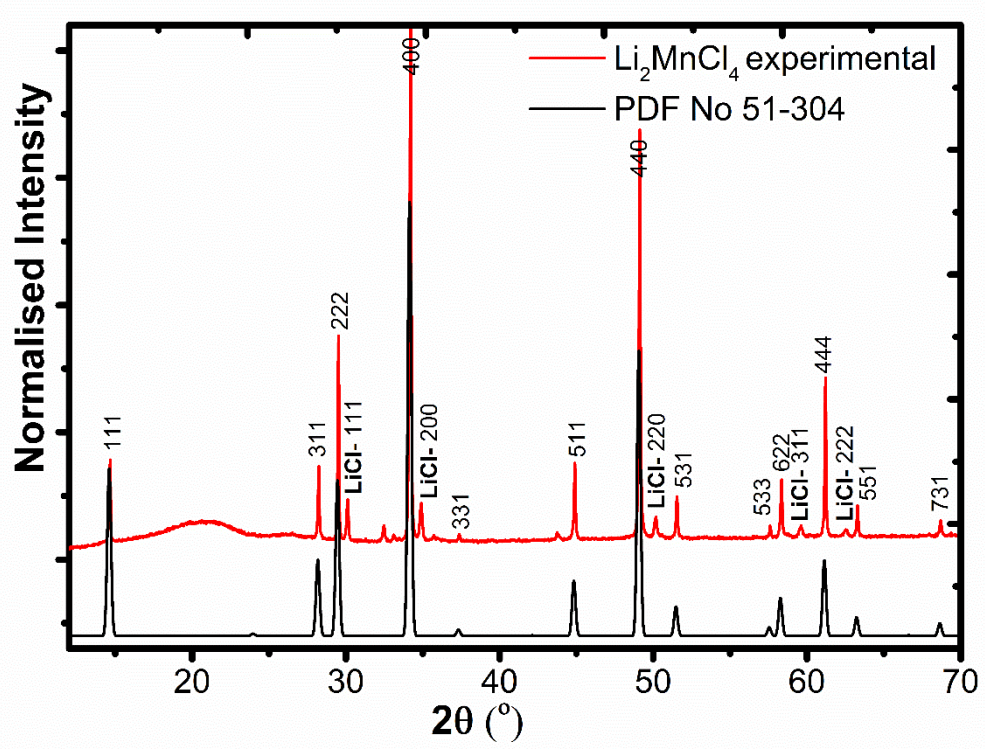

Figure 6.5. PXRD data of Li_2MnCl_4 at room temperature. Experimental pattern is shown by the red line and the simulated diffraction pattern using published crystallographic model [10] is shown by the black line. Impurity is LiCl

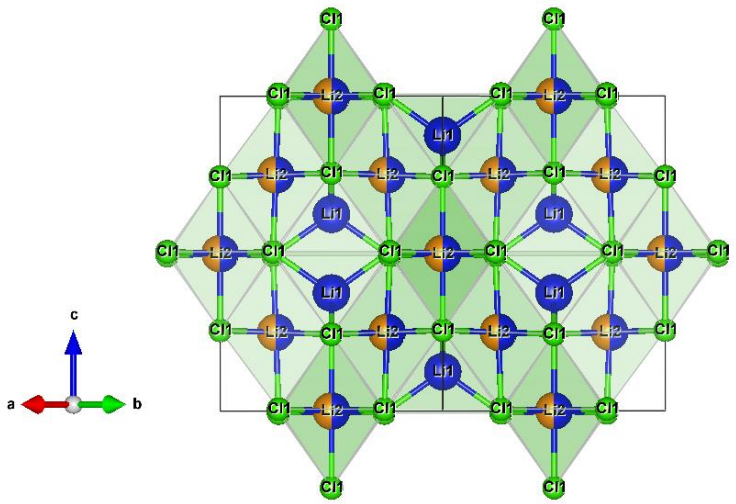

Figure 6.6. Crystal structure of Li_2MnCl_4. Green atoms are chlorine, blue atoms are lithium, orange atoms are manganese

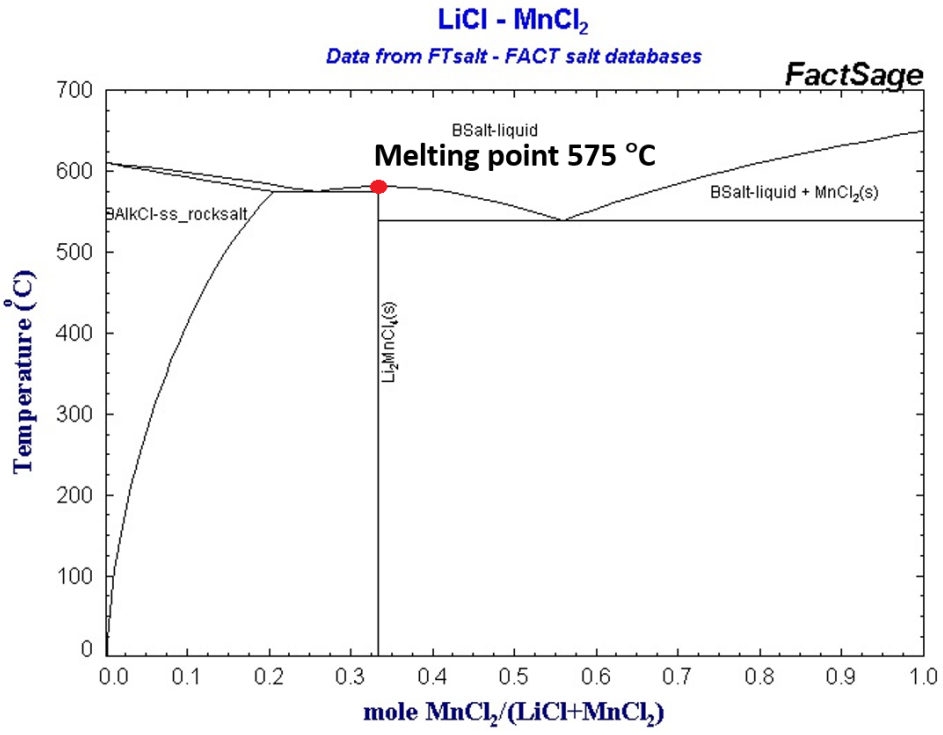

Figure 6.7. Phase diagram of $MnCl_2$ – LiCl system [9]

The morphology of Li_2MnCl_4 was investigated by SEM before and after discharge and images are shown in Figures 6.8a and 6.8b. The SEM images show that the morphology has been changed after the discharge. However, there is no difference that could be observed in the size of the crystallites.

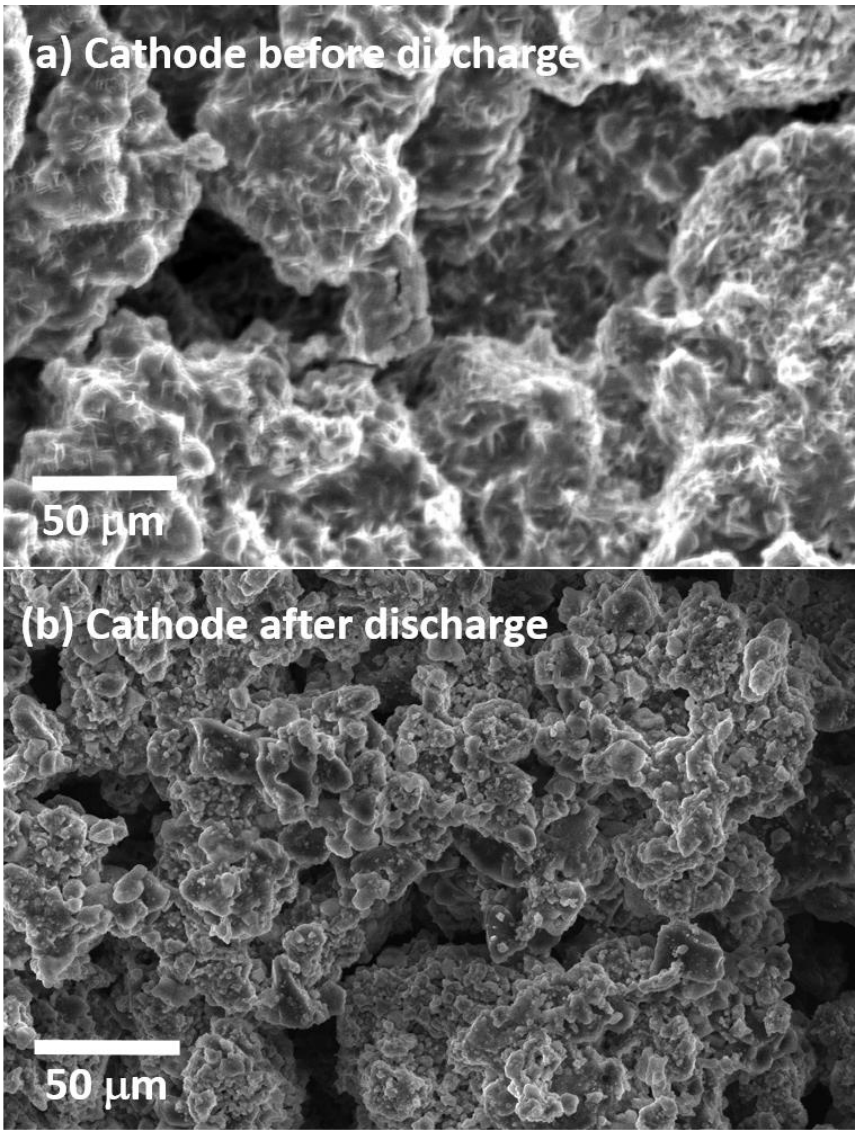

Figure 6.8. SEM images of Li_2MnCl_4 before (a) and after (b) discharge

6.1.3 **Li_6VCl_8**

The diffraction pattern is shown in Figure 6.9. In the synthesis of Li_6VCl_8 the main phase corresponded to Li_6VCl_8 but there is also a V_2O_3 impurity (a = 4.948(7) Å, c = 13.989(20) Å). As the synthesis of Li_6VCl_8 was in a sealed quartz tube this work suggests that the V_2O_3 arises as an impurity in the synthesis of the VCl_2 reagent during the decomposition VCl_3 to VCl_2. Li_6VCl_8 crystallises in cubic $Fm\bar{3}m$ with cell parameter (a = 10.294(5) Å) as shown in Figure 6.10. The phase diagram, as shown in Figure 6.11, shows the melting point of Li_6VCl_8 at 763 °C [11].

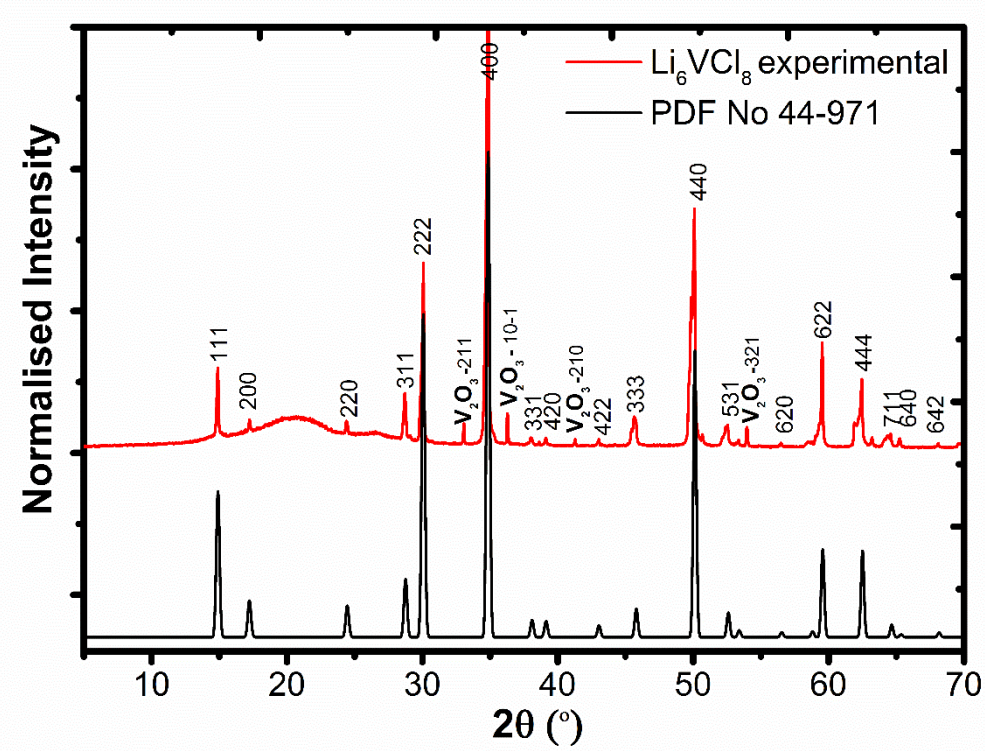

Figure 6.9. PXRD data of Li_6VCl_8 at room temperature. Experimental pattern is shown by the red line and the simulated diffraction pattern using published crystallographic model [11] is shown by the black line. Impurity is V_2O_3

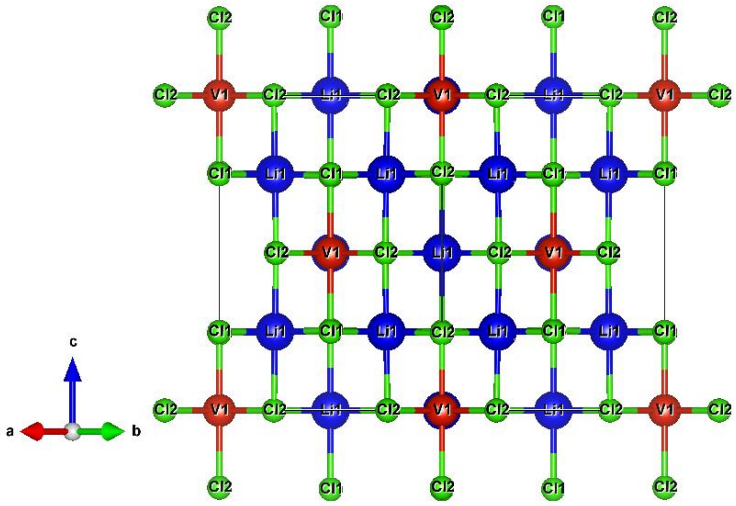

Figure 6.10. Crystal structure of Li_6VCl_8. Green atoms are chlorine, blue atoms are lithium and red atoms are vanadium

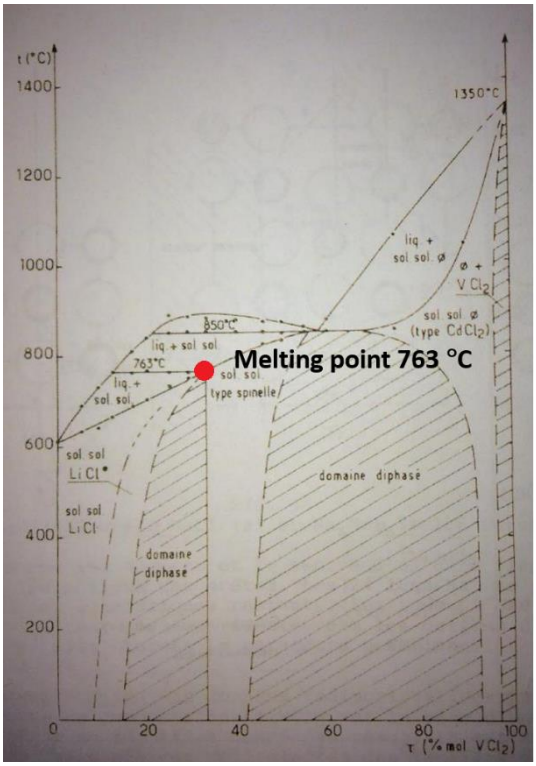

Figure 6.11. Phase diagram of VCl_2 – LiCl system

(permission by Hanebali L, Machej T, Cros C and Hagenmuller P) [11]

The morphology of Li_6VCl_8 was studied by SEM before and after discharge and results are presented in Figures 6.12a and 6.12b. SEM images show that the morphology has been changed after the discharge and the size of the crystallites differs. The size of the crystallites is bigger than 50 μm before the discharge. However, the size of the crystallites is smaller than 50 μm after the discharge.

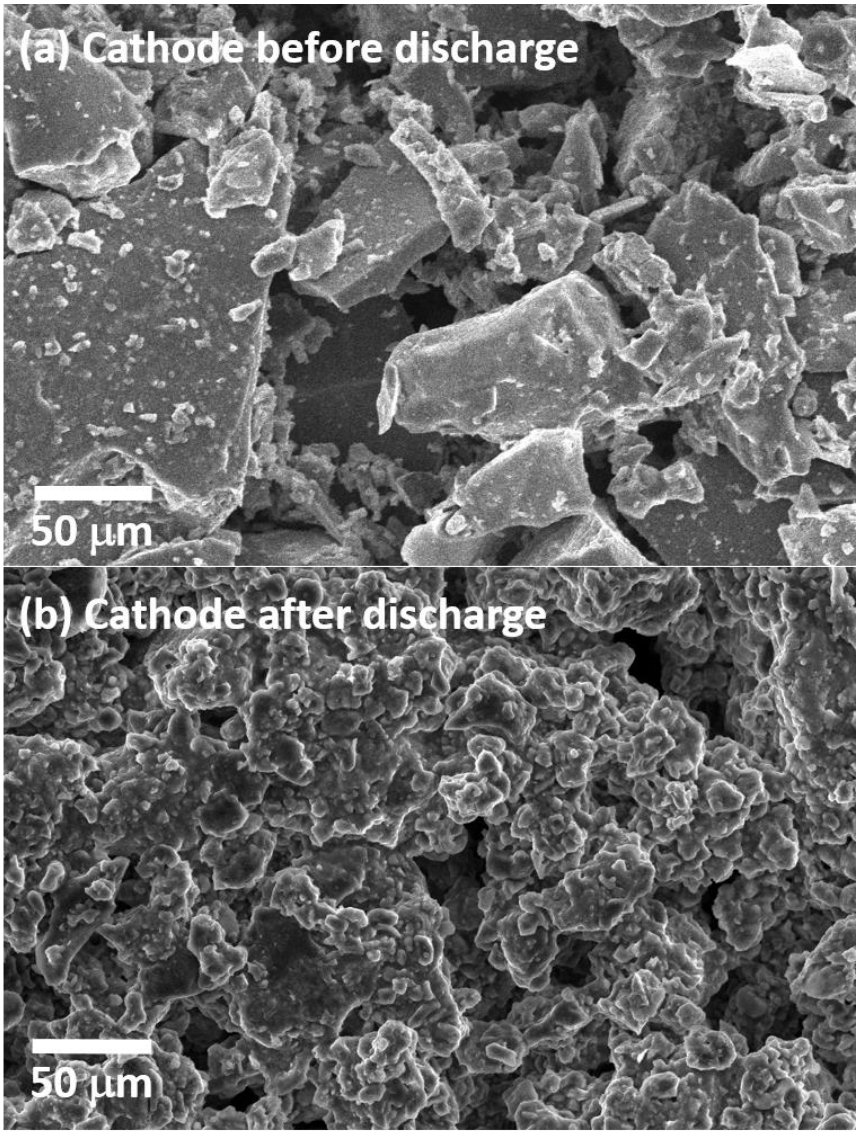

Figure 6.12. SEM images of Li_6VCl_8 before (a) and after (b) discharge

All the samples were studied electrochemically with the impurities (LiCl and KCl) as the electrolyte LiCl-KCl eutectic which is used, consists of KCl and LiCl.

6.1.4 **$NiCl_2$**

$NiCl_2$ (Alfa Aesar, 99%) was analysed by powder X-ray diffraction and the resulting diffraction pattern is presented in Figure 6.13. $NiCl_2$ was identified as the main phase and crystallises in trigonal $R\bar{3}m$ with cell dimensions ($a = b = 3.468(21)$ Å and $c = 17.30(7)$ Å). $NiCl_2$ adopts a layer structure, in which each Ni^{2+} is coordinated to six Cl^- and each chloride is bonded to three Ni as shown in Figure 6.14 [12]. The $NiCl_6$ octahedra are shared with other octahedra in such a way as to form layers along *c*-axis. The melting point of $NiCl_2$ is 1030 °C [13].

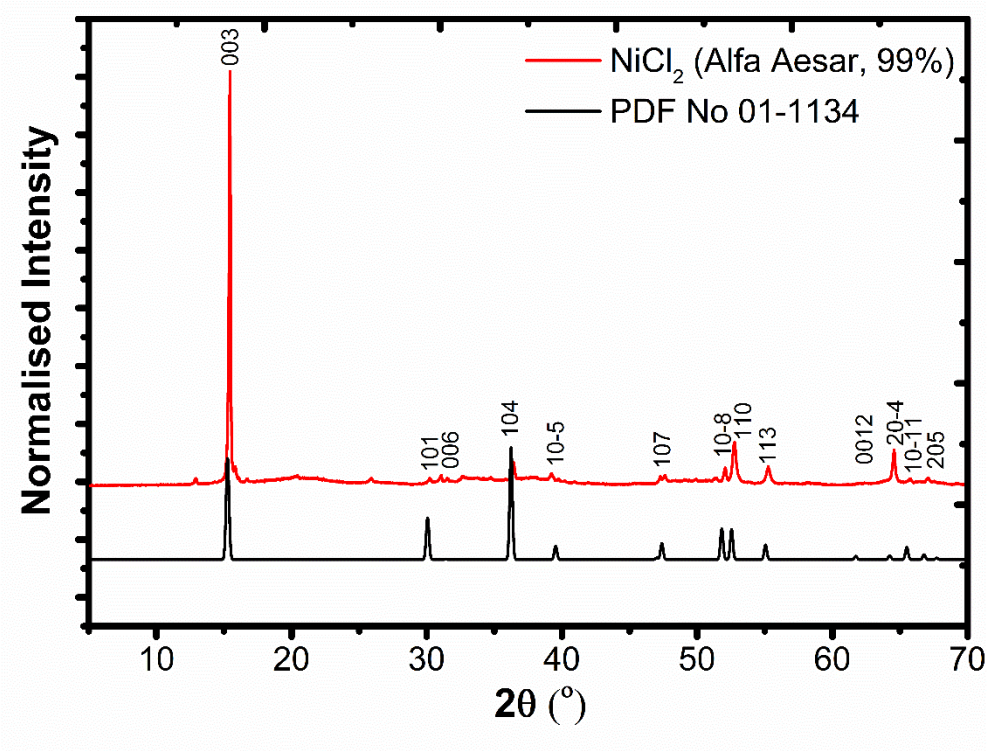

Figure 6.13. PXRD data of $NiCl_2$ at room temperature. Experimental pattern is shown by the red line and the simulated diffraction pattern using published crystallographic model [14] is shown by the black line

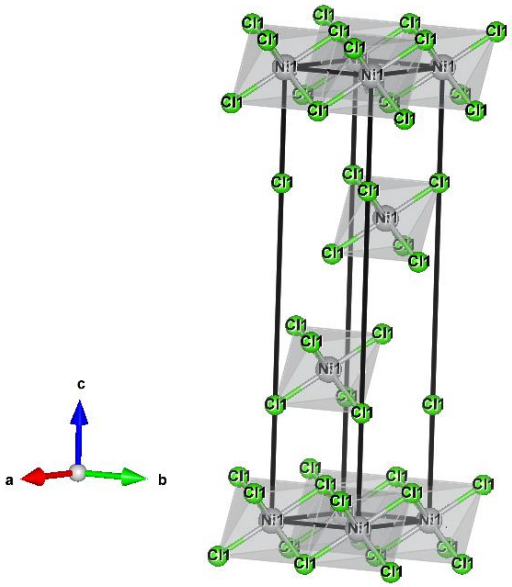

Figure 6.14. Crystal structure of $NiCl_2$. Green atoms are chlorine and grey atoms are nickel

SEM images, as shown in Figures 6.15a and 6.15b, show the morphology and the size of crystallites before and after testing. EDX confirms Ni 30 ±2 at% and Cl 70 ±2 at% as expected for $NiCl_2$ before it being tested as a cathode in a Li thermal battery, as shown in Figure 6.15a. The elemental analysis of $NiCl_2$ cathode electrode after testing is Ni 62 ±1 at% and Cl 38 ±1 at% (Figure 6.15b) and this means different products of the electrochemical mechanism are formed, such as Ni metal and LiCl. These products will be investigated at a later stage by powder X-ray diffraction.

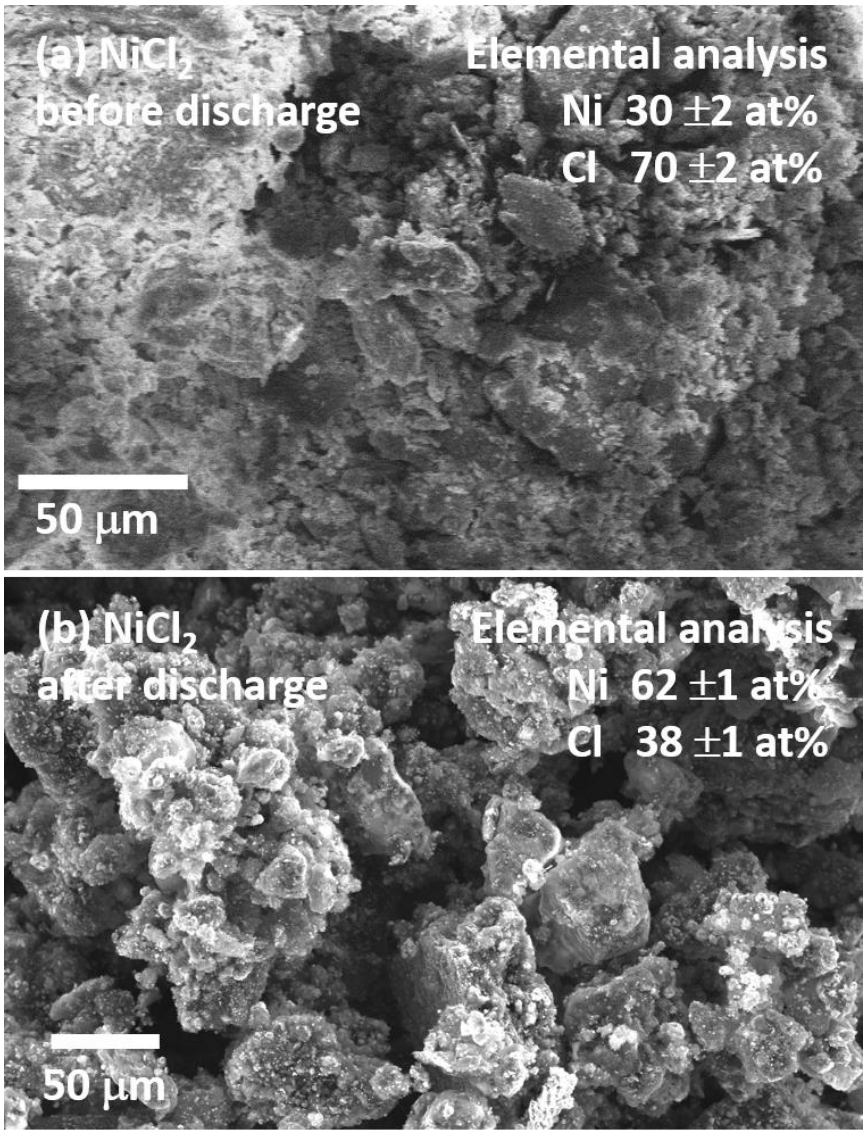

Figure 6.15. SEM images of $NiCl_2$ before (a) and after (b) discharge

6.1.5 **$CoCl_2$**

$CoCl_2$ (Alfa Aesar, 99.7 %) was analysed by powder X-ray diffraction and the resulting diffraction pattern is presented in Figure 6.16. $CoCl_2$ was identified as the main phase and crystallises in hexagonal $R\bar{3}m$ with cell dimensions ($a = b = 3.55(7)$ Å and $c = 17.36(9)$ Å). $CoCl_2$ adopts the same structure as $NiCl_2$, as shown in Figure 6.17. The melting point of $CoCl_2$ is 740 °C [15].

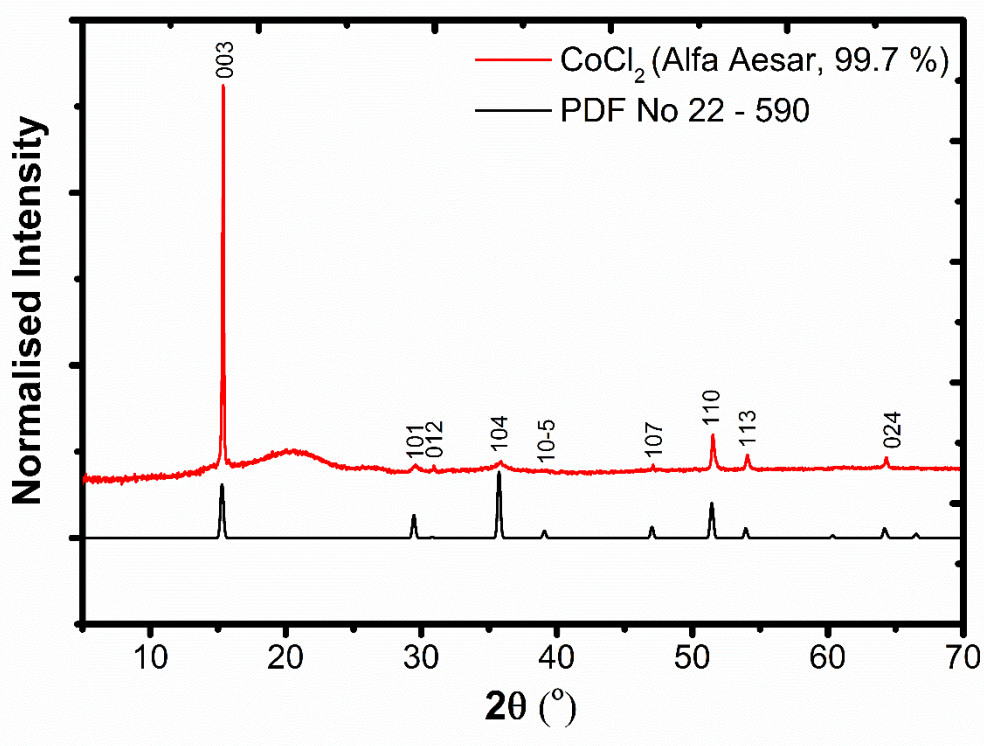

Figure 6.16. PXRD data of $CoCl_2$ at room temperature. Experimental pattern is shown by the red line and the simulated diffraction pattern using published crystallographic model [16] is shown by the black line

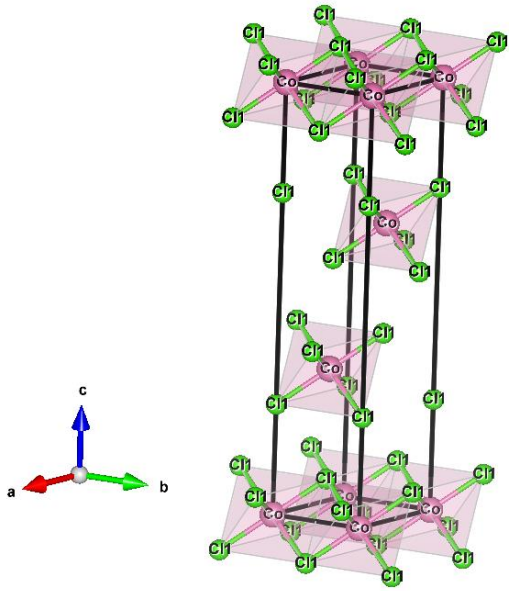

Figure 6.17. Crystal structure of $CoCl_2$. Green atoms are chlorine and pink atoms are cobalt

The morphology and the size of crystallites of $CoCl_2$ was studied by SEM as shown in Figures 6.18a and 6.18b. The morphology and the size of the crystallites have been changed after the discharge. EDX confirms Co 32 ±2 at% and Cl 68 ±2 at% as expected for $CoCl_2$ before it being tested as a cathode in a Li thermal battery, as shown in Figure 6.18a. The elemental analysis of $CoCl_2$ cathode electrode after testing is Co 8 ±1 at% and Cl 92 ±1 at% (Figure 6.18b) and this means different products of the electrochemical mechanism are formed, such as Co metal and LiCl. These products will be investigated at a later stage by powder X-ray diffraction.

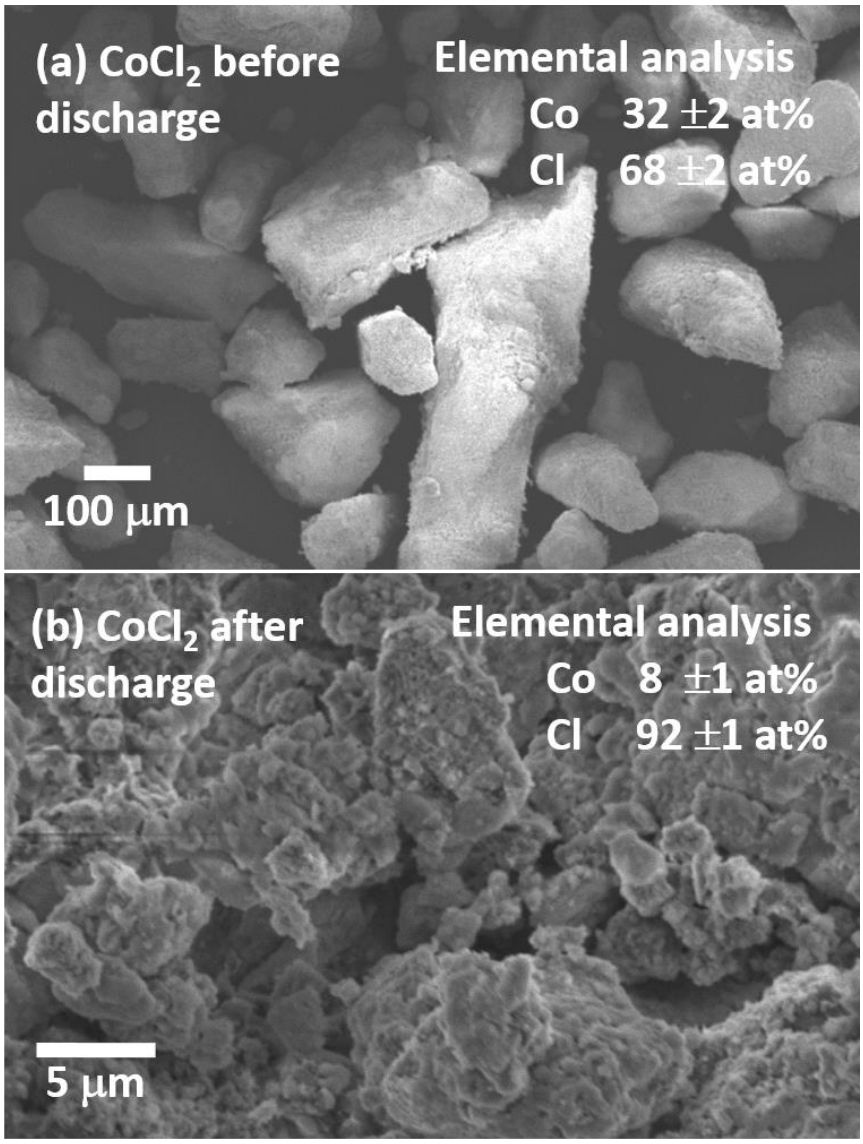

Figure 6.18. SEM images of $CoCl_2$ before (a) and after (b) discharge

6.2 **Electrochemical Investigation of Transition Metal Chlorides**

All transition metal chlorides were studied electrochemically by galvanostatic discharge and galvanostatic intermittent titration technique.

6.2.1 **$KNiCl_3$**

Galvanostatic discharge curves for measurements carried out at 425 °C for $KNiCl_3$ are presented in Figure 6.19. Galvanostatic discharge was performed at different current densities from 15 mA/cm^2 to 75 mA/cm^2 and the voltage cut-off was 1 V. At current densities of 15, 30 and 60 mA/cm^2 there is a high cell voltage (2.30 V) but a flat voltage plateau could not be obtained. At current densities of 68 and 75 mA/cm^2 the cell voltage is lower which is probably due to a higher cell resistance as confirmed at a later stage by GITT. A capacity of 262 mA h g^{-1} was measured for $KNiCl_3$ and this corresponds to a value of x = 2 for the number of lithium atoms transferred during the discharge process. The electrochemical mechanism corresponds to:

$$KNiCl_3 + 2\ Li \Rightarrow KCl + 2\ LiCl + Ni \quad [6.1]$$

This electrochemical reaction [6.1] is expected as it is analogous to the system $Na/NaAlCl_4/NiCl_2$ [17]. Capacities of 259, 220, 210 and 150 mA h g^{-1} were measured at a current densities of 30, 60, 68 and 75 mA/cm^2, respectively. The amount of active anode (0.15 g) corresponds to 73 mA h for the discharge plateau from $Li_{13}Si_4$ to Li_7Si_3 which is 0.157 V vs Li. The measured capacity of the cathode is 39.3 mA h which keeps the discharge as being performed against the 0.157 V Li plateau.

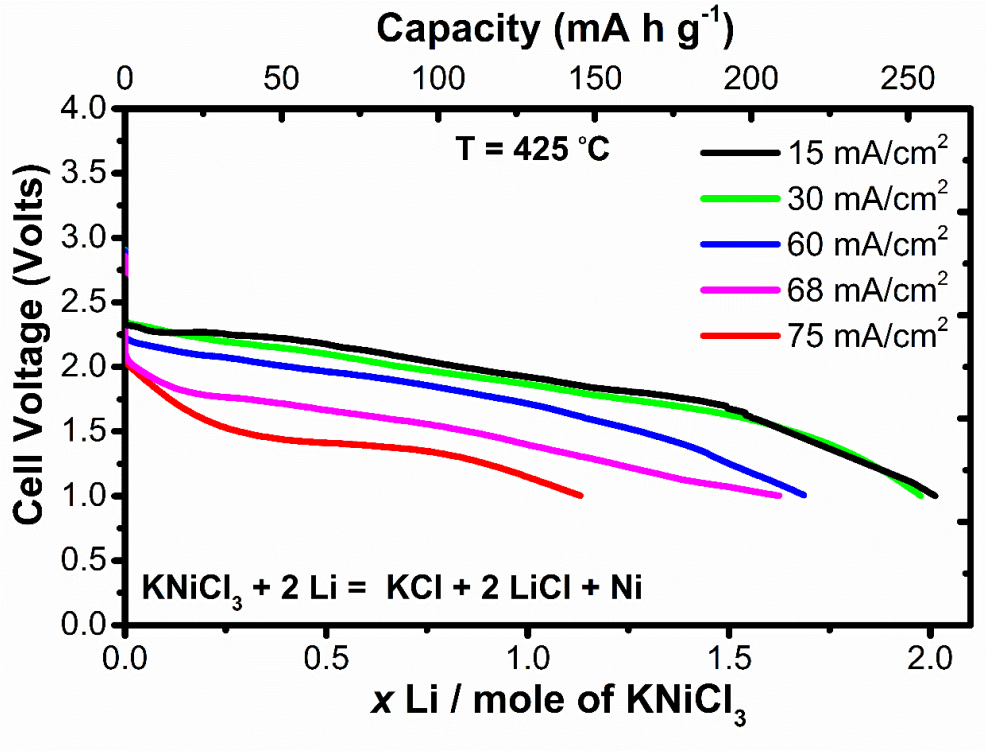

Figure 6.19. Galvanostatic discharge of $KNiCl_3$ at current densities of 15, 30, 60, 68 and 75 mA/cm^2 at 425 °C

Galvanostatic intermittent titration technique curve for a measurement at 425 °C of $KNiCl_3$ is shown in Figure 6.20. The galvanostatic intermittent titration technique measurements (GITT) show the IR drop is 125 mV at the beginning of discharge and 375 mV at the end of the measurement, which indicates that the cell resistance is increasing during the reduction of the cathode, from a resistance of 16 Ω at the beginning of the measurement to 50 Ω after the cell discharge, which suggests that it is more difficult for the lithium ions to transfer from the anode to the cathode electrode. The voltage profile is still high at 2.5 V at a current density of 7.5 mA/cm^2.

The chemical diffusion coefficient D = 3.82 10^{-6} cm^2 s^{-1} for $KNiCl_3$ can be calculated from equation [3.1] where n_m = 0.000979 (mol), V_m = 71.88 (cm^3 / mol), ΔE_s = 0.060 (V) and ΔE_t = 0.075 (V).

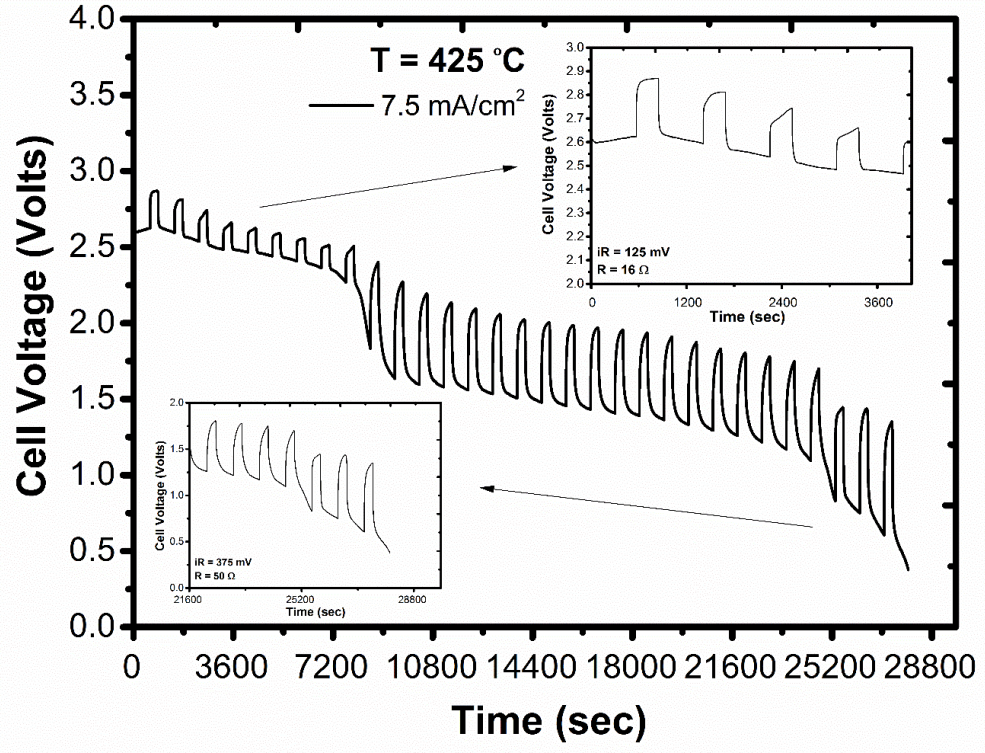

Figure 6.20. Galvanostatic intermittent titration technique of $KNiCl_3$ at current density of 7.5 mA/cm^2 at 425 °C

6.2.2 Li_2MnCl_4

Galvanostatic discharge curves for measurements carried out at 400 °C for Li_2MnCl_4 are presented in Figure 6.21. Galvanostatic discharge was performed at different current densities from 15 mA/cm^2 to 75 mA/cm^2 and the voltage cut-off was 1 V. At a current density of 15 mA/cm^2 there is a high cell voltage (2.50 V) similar to $KNiCl_3$ but again a flat voltage plateau could not be obtained. At current densities of 30, 45 and 75 mA/cm^2 the cell voltage is lower which is probably due to a higher cell resistance as confirmed at a later stage by GITT. Li_2MnCl_4 exhibits a maximum capacity of 254 mA h g^{-1} and the electrochemical mechanism corresponds to:

$$Li_2MnCl_4 + 2\ Li \Rightarrow 4\ LiCl + Mn \quad [6.2]$$

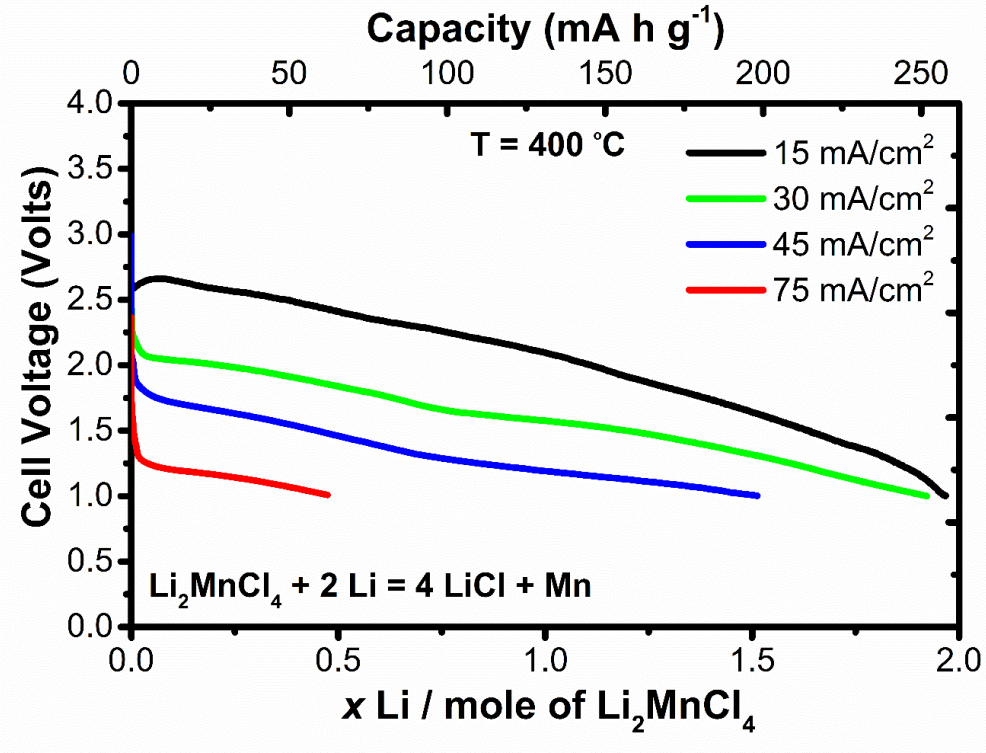

Figure 6.21. Galvanostatic discharge of Li_2MnCl_4 at current densities of 15, 30, 45 and 75 mA/cm^2 at 400 °C

Capacities of 250, 200 and 65 mA h g^{-1} were measured at a current densities of 30, 45 and 75 mA/cm^2, respectively. The amount of active anode (0.15 g) corresponds to 73 mA h for the discharge plateau from $Li_{13}Si_4$ to Li_7Si_3 which is 0.157 V vs Li. The measured capacity of the cathode is 38.1 mA h which keeps the discharge as being performed against the 0.157 V Li plateau.

Galvanostatic intermittent titration technique curve for measurements carried out at 400 °C for Li_2MnCl_4 is presented in Figure 6.22. The IR drop is 100 mV at the beginning of discharge and 625 mV at the end of the measurement, which indicates that the cell resistance is increasing from a resistance of 13 Ω at the beginning of the measurement to 83 Ω after the cell discharge. However, the voltage profile is still high at 2.75 V at a current density of 7.5 mA/cm^2. The chemical diffusion coefficient D = 1.18 10^{-5} cm^2 s^{-1} for Li_2MnCl_4 can be calculated from equation [3.1] where n_m = 0.000949 (mol), V_m = 87.03 (cm^3 / mol), ΔE_s = 0.060 (V) and ΔE_t = 0.050 (V).

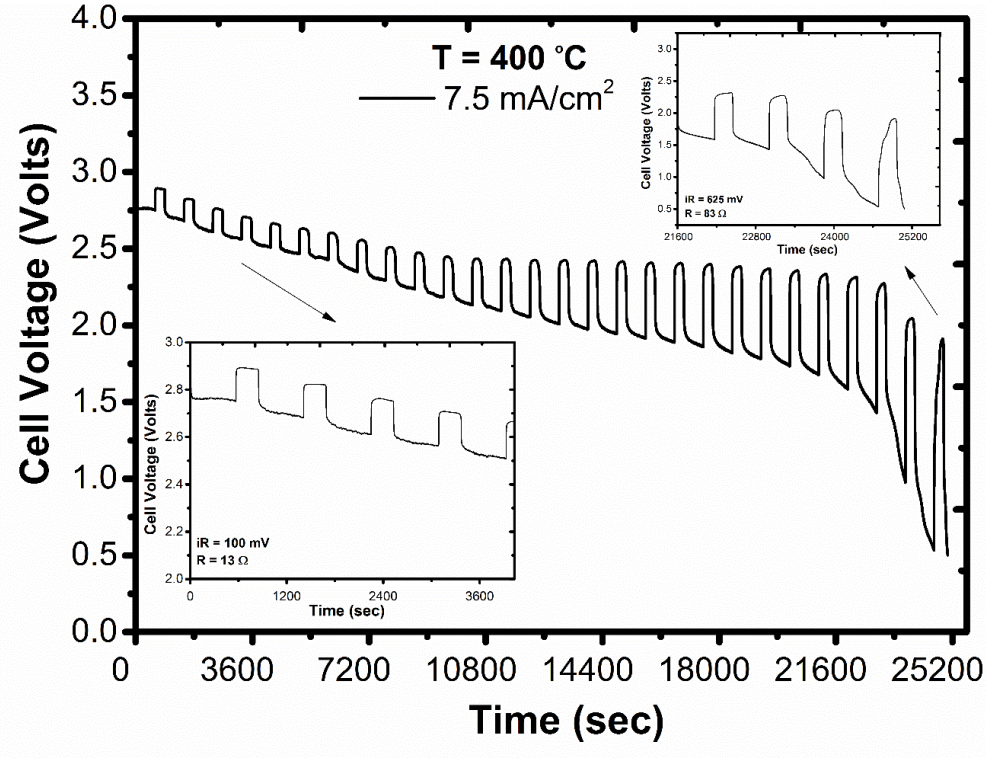

Figure 6.22. Galvanostatic intermittent titration technique of Li_2MnCl_4 at current density of 7.5 mA/cm^2 at 400 °C

6.2.3 **Li_6VCl_8**

Galvanostatic discharge curves for measurements carried out at 500 °C for Li_6VCl_8 are presented in Figure 6.23. Galvanostatic discharge was performed at different current densities from 7.5 mA/cm^2 to 45 mA/cm^2 and the voltage cut-off was 1 V. At a current density of 7.5 mA/cm^2 there is a flat voltage plateau at 1.80 V and a capacity of 145 mA h g^{-1} was achieved. At current densities of 23 and 30 mA/cm^2, Li_6VCl_8 shows a lower but again flat voltage plateau at 1.50 V. However, at a current density of 45 mA/cm^2 a flat voltage plateau could not be obtained. The electrochemical mechanism corresponds to:

$$Li_6VCl_8 + 2\ Li \Rightarrow 8\ LiCl + V \quad [6.3]$$

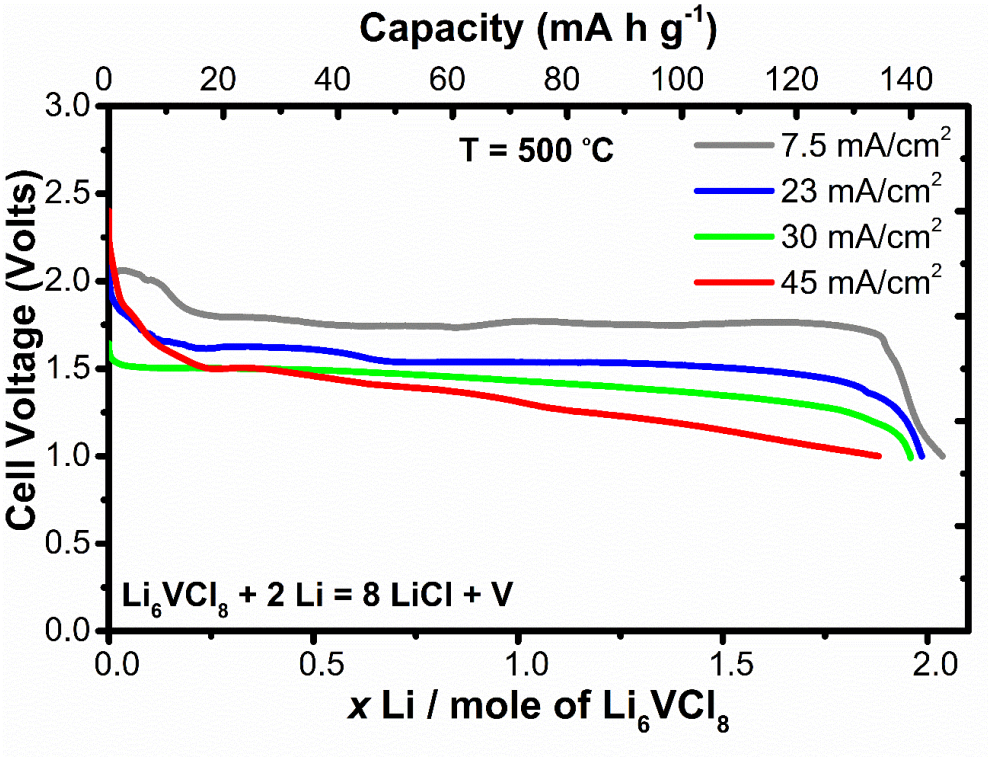

Figure 6.23. Galvanostatic discharge of Li_6VCl_8 at current densities of 7.5, 23, 30 and 45 mA/cm^2 at 500 °C

Capacities of 140, 138 and 135 mA h g^{-1} were measured at a current densities of 23, 30 and 45 mA/cm^2, respectively. The amount of active anode (0.15 g) corresponds to 73 mA h for the discharge plateau from $Li_{13}Si_4$ to Li_7Si_3 which is 0.157 V vs Li. The measured capacity of the cathode is 21.75 mA h which keeps the discharge as being performed against the 0.157 V Li plateau.

Galvanostatic intermittent titration technique curve for a measurement carried out at 500 °C for Li_6VCl_8 is presented in Figure 6.24. The cell resistance increases during the reduction of the cathode from 6 Ω at the beginning to 33 Ω at the end of discharge.

The chemical diffusion coefficient D = 5.74 10^{-7} cm^2 s^{-1} for Li_6VCl_8 can be calculated from equation [3.1] where n_m = 0.000531 (mol), V_m = 164.28 (cm^3 / mol), ΔE_s = 0.025 (V) and ΔE_t = 0.100 (V).

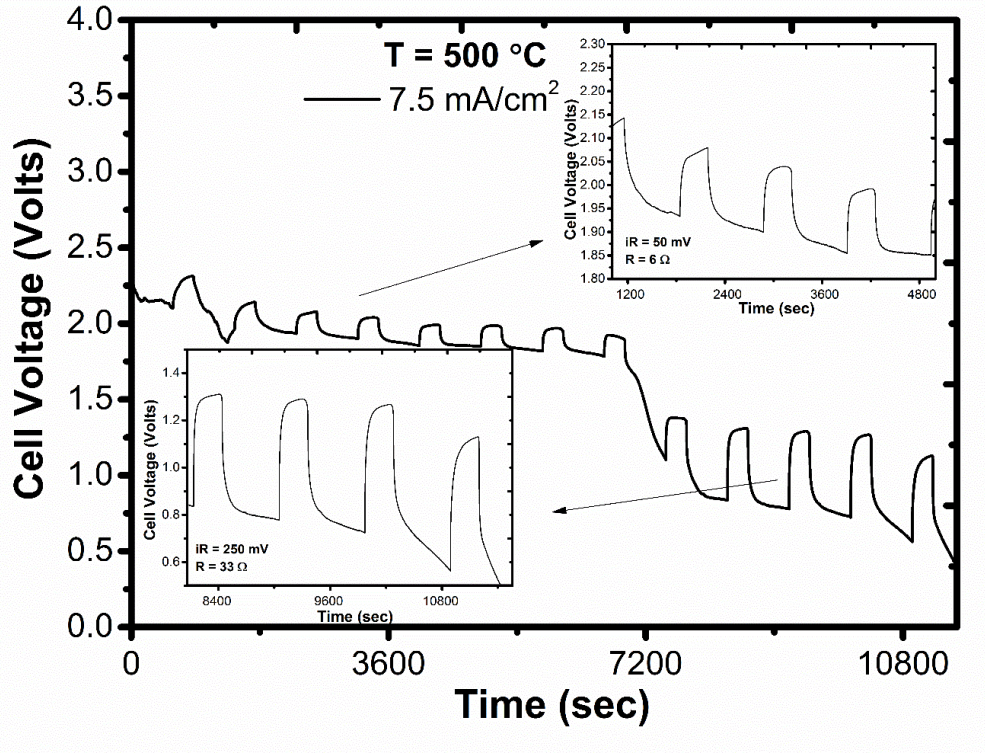

Figure 6.24. Galvanostatic intermittent titration technique of Li_6VCl_8 at current density of 7.5 mA/cm^2 at 500 °C

6.2.4 **$NiCl_2$**

Galvanostatic discharge curves for measurements carried out at 500 °C for $NiCl_2$ are presented in Figure 6.25. Galvanostatic discharge was performed at different current densities from 22 mA/cm^2 to 75 mA/cm^2 and the voltage cut-off was 1 V. At current densities of 22, 38 and 60 mA/cm^2 there is a high cell voltage over than 2 V and a voltage plateau could be obtained. At current densities of 75 mA/cm^2 the cell voltage is lower which is probably due to a higher cell resistance as confirmed at a later stage by GITT. $NiCl_2$ exhibits a capacity of 360 mA h g^{-1} and the electrochemical mechanism corresponds to:

$$NiCl_2 + 2\ Li \Rightarrow 2\ LiCl + Ni \quad [6.4]$$

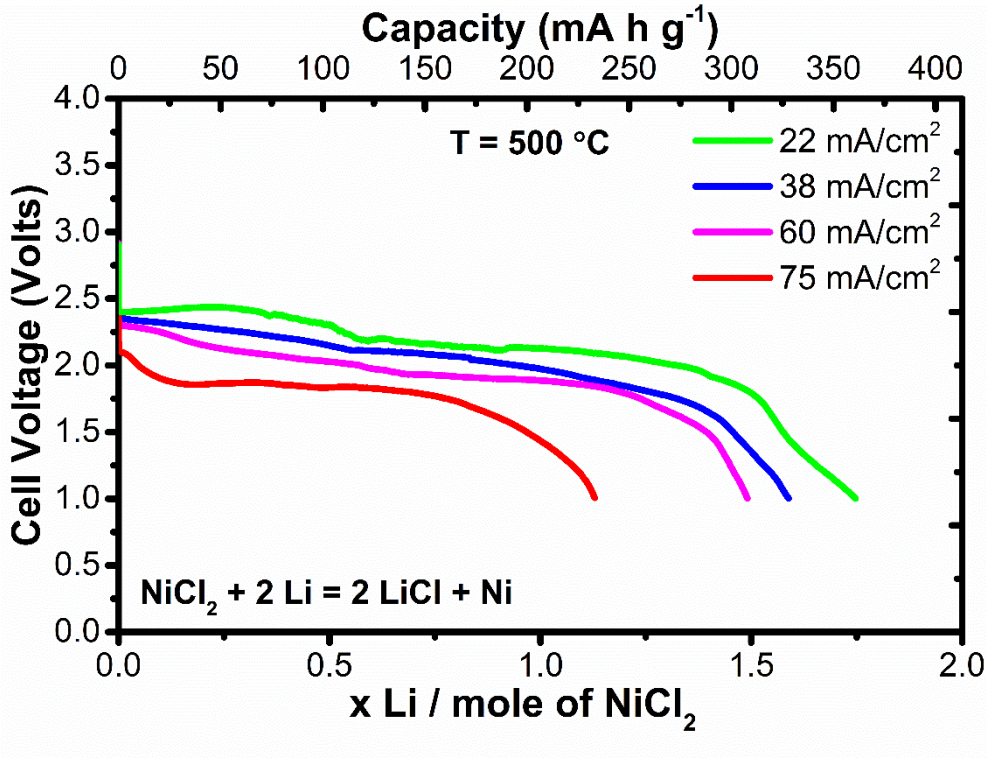

Figure 6.25. Galvanostatic discharge of $NiCl_2$ at current densities of 22, 38, 60 and 75 mA/cm^2 at 500 °C

Capacities of 325, 310 and 230 mA h g^{-1} were measured at a current densities of 38, 60 and 75 mA/cm^2, respectively. The amount of active anode (0.15 g) corresponds to 73 mA h for the discharge plateau from $Li_{13}Si_4$ to Li_7Si_3 which is 0.157 V vs Li. The measured capacity of the cathode is 54 mA h which keeps the discharge as being performed against the 0.157 V Li plateau.

Galvanostatic intermittent titration technique curve for a measurement at 500 °C of $NiCl_2$ is shown in Figure 6.26. The galvanostatic intermittent titration technique measurements (GITT) show the IR drop is 100 mV at the beginning of discharge and 250 mV at the end of the measurement, which indicates that the cell resistance is increasing during the reduction of the cathode, from a resistance of 13 Ω at the beginning of the measurement to 33 Ω after the cell discharge, which suggests that it is more difficult for the lithium ions to transfer from the anode to the cathode electrode.

The chemical diffusion coefficient D = 8.23 10^{-6} cm^2 s^{-1} for $NiCl_2$ can be calculated from equation [3.1] where n_m = 0.0015 (mol), V_m = 36.71 (cm^3 / mol), ΔE_s = 0.075 (V) and ΔE_t = 0.050 (V).

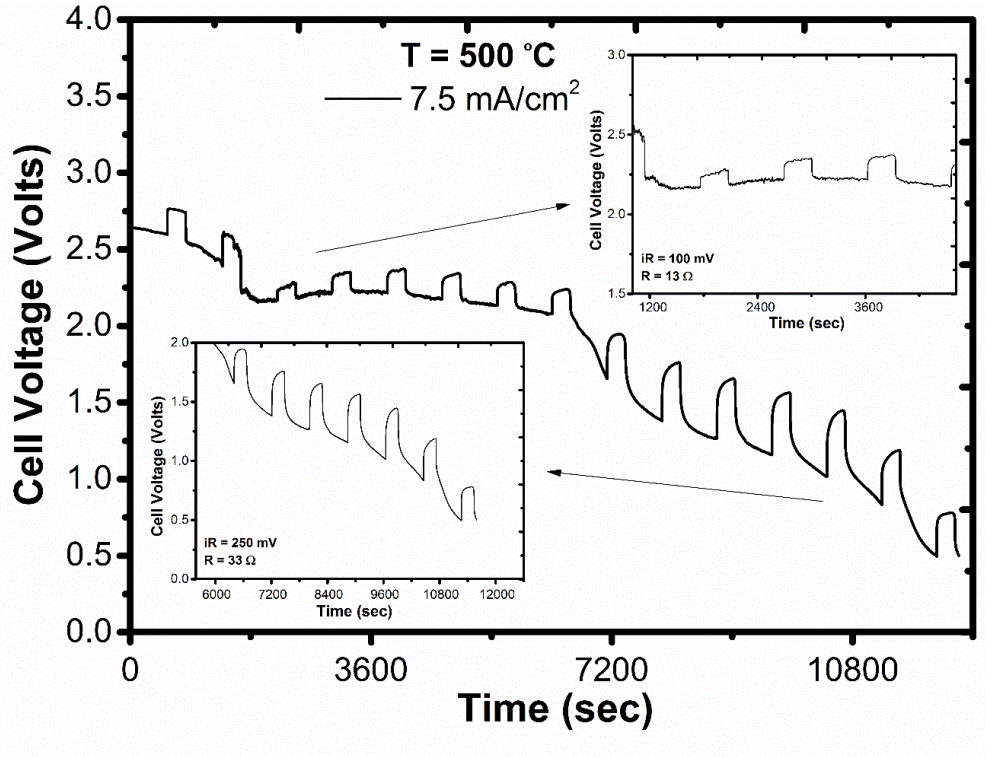

Figure 6.26. Galvanostatic intermittent titration technique of $NiCl_2$ at current density of 7.5 mA/cm^2 at 500 °C

6.2.5 **$CoCl_2$**

Galvanostatic discharge curves for measurements carried out at 500 °C for $CoCl_2$ are presented in Figure 6.27. Galvanostatic discharge was performed at different current densities from 15 mA/cm^2 to 75 mA/cm^2 and the voltage cut-off was 1 V. At current densities of 15 and 45 mA/cm^2 there is a high cell voltage around 2 V but a flat voltage plateau could not be obtained. At current densities of 60 and 75 mA/cm^2 the cell voltage is still high but again there is no flat voltage plateau. $CoCl_2$ exhibits a capacity of 330 mA h g^{-1} and the electrochemical mechanism corresponds to:

$$CoCl_2 + 2\ Li \Rightarrow 2\ LiCl + Co \quad [6.5]$$

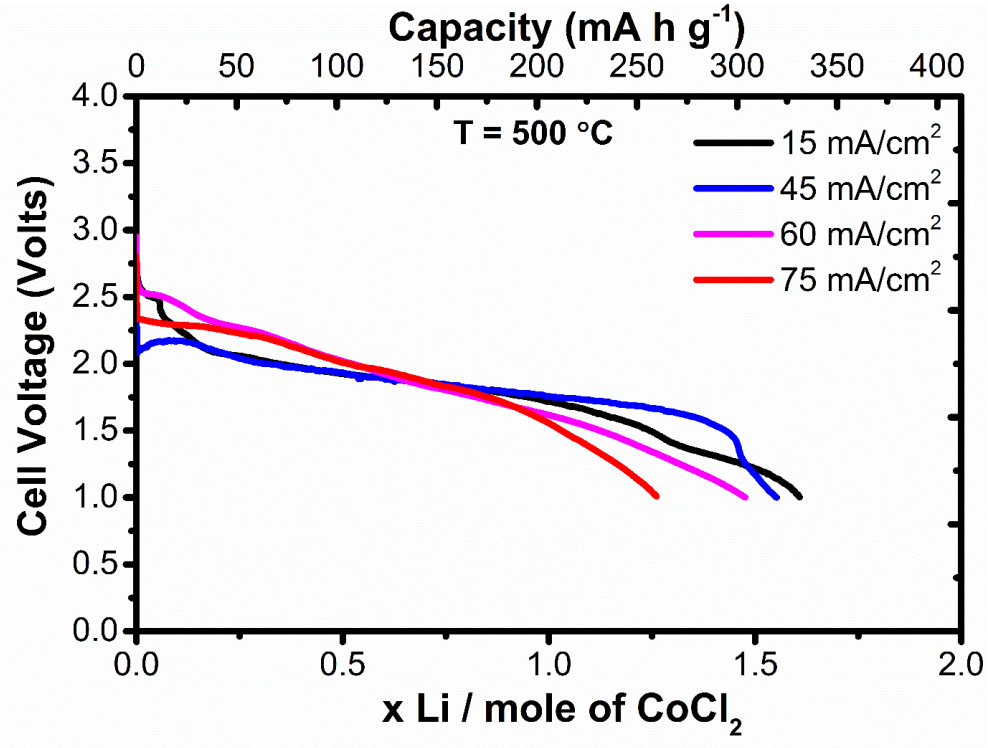

Figure 6.27. Galvanostatic discharge of $CoCl_2$ at current densities of 15, 45, 60 and 75 mA/cm^2 at 500 °C

Capacities of 325, 310 and 260 mA h g^{-1} were measured at a current densities of 45, 60 and 75 mA/cm^2, respectively. The amount of active anode (0.15 g) corresponds to 73 mA h for the discharge plateau from $Li_{13}Si_4$ to Li_7Si_3 which is 0.157 V vs Li. The measured capacity of the cathode is 50 mA h which keeps the discharge as being performed against the 0.157 V Li plateau.

Galvanostatic intermittent titration technique curve for a measurement at 500 °C of $CoCl_2$ is shown in Figure 6.28. The galvanostatic intermittent titration technique measurements (GITT) show the IR drop is 50 mV at the beginning of discharge and 200 mV at the end of the measurement, which indicates that the cell resistance is increasing during the reduction of the cathode, from a resistance of 6 Ω at the beginning of the measurement to 26 Ω after the cell discharge, which suggests that it is more difficult for the lithium ions to transfer from the anode to the cathode electrode. $CoCl_2$ compared to $NiCl_2$ is more conductive.

The chemical diffusion coefficient D = 1.58 10^{-5} cm^2 s^{-1} for $CoCl_2$ can be calculated from equation [3.1] where n_m = 0.0015 (mol), V_m = 38.18 (cm^3 / mol), ΔE_s = 0.050 (V) and ΔE_t = 0.025 (V).

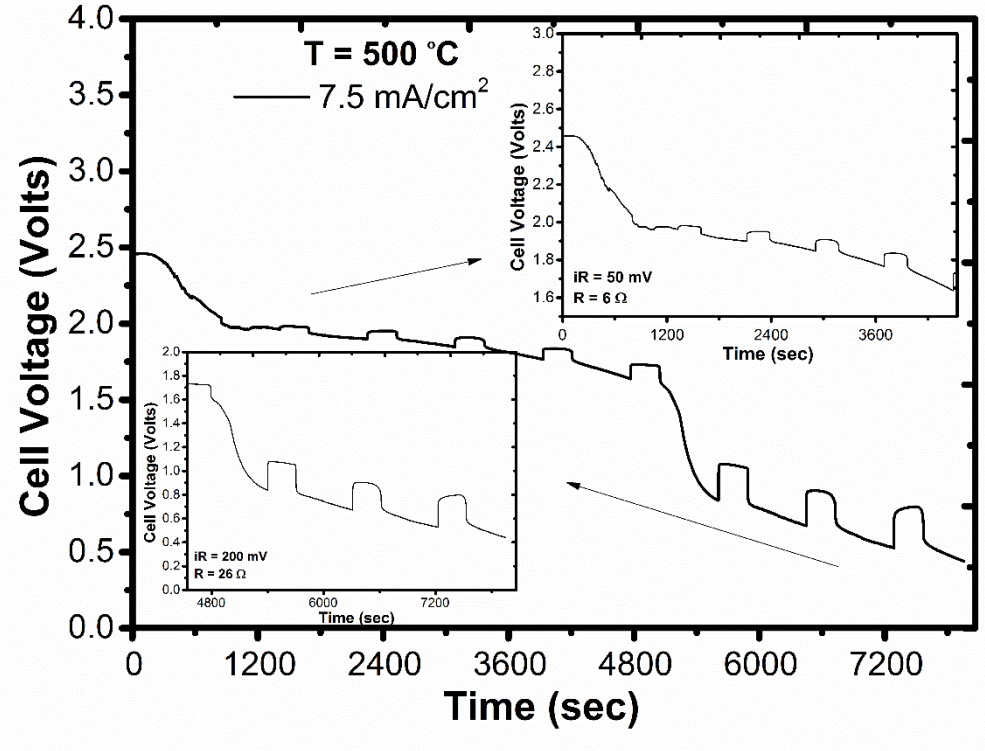

Figure 6.28. Galvanostatic intermittent titration technique of $CoCl_2$ at current density of 7.5 mA/cm^2 at 500 °C

PXRD data were collected after discharge for all of the cathodes as shown in Figures 6.29 and 6.30.

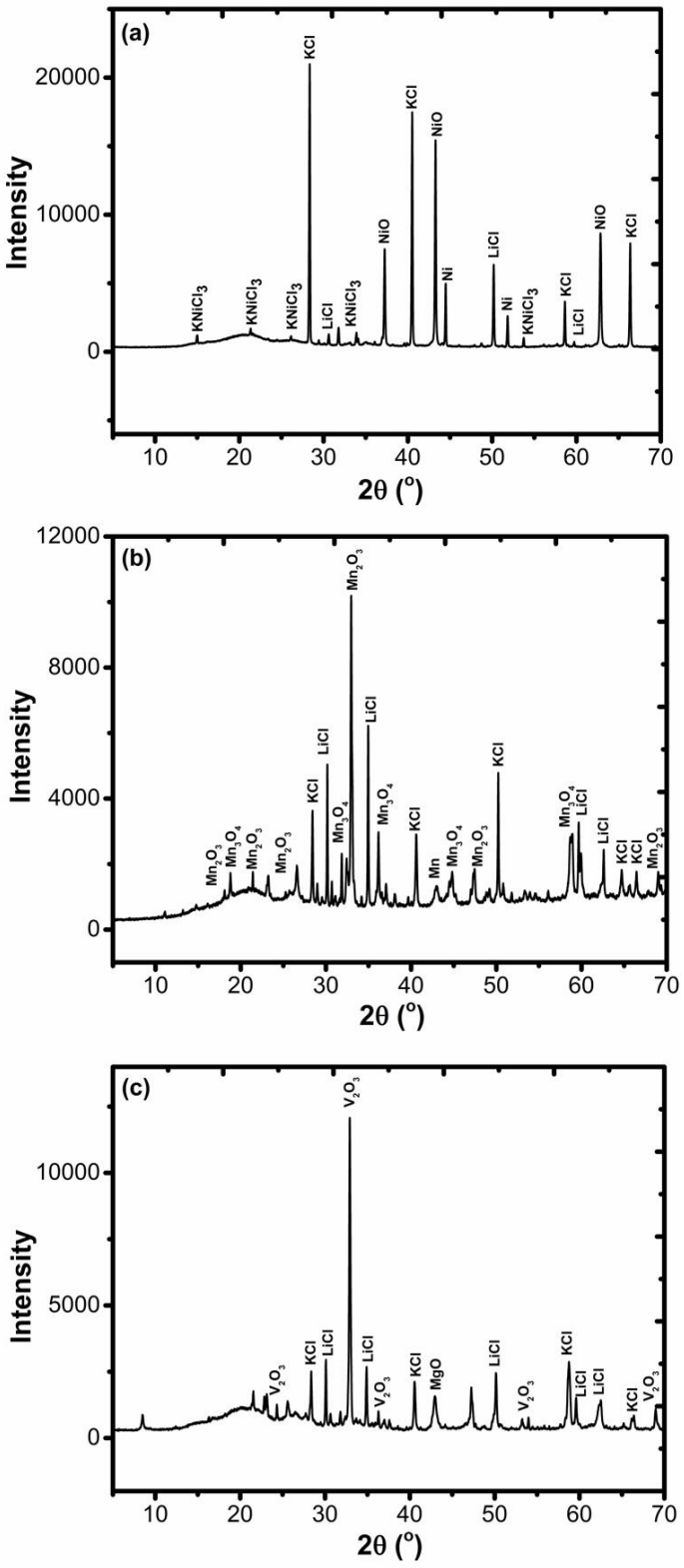

Figure 6.29. PXRD data of the cathode after galvanostatic discharge of (a) $KNiCl_3$, (b) Li_2MnCl_4, and (c) Li_6VCl_8

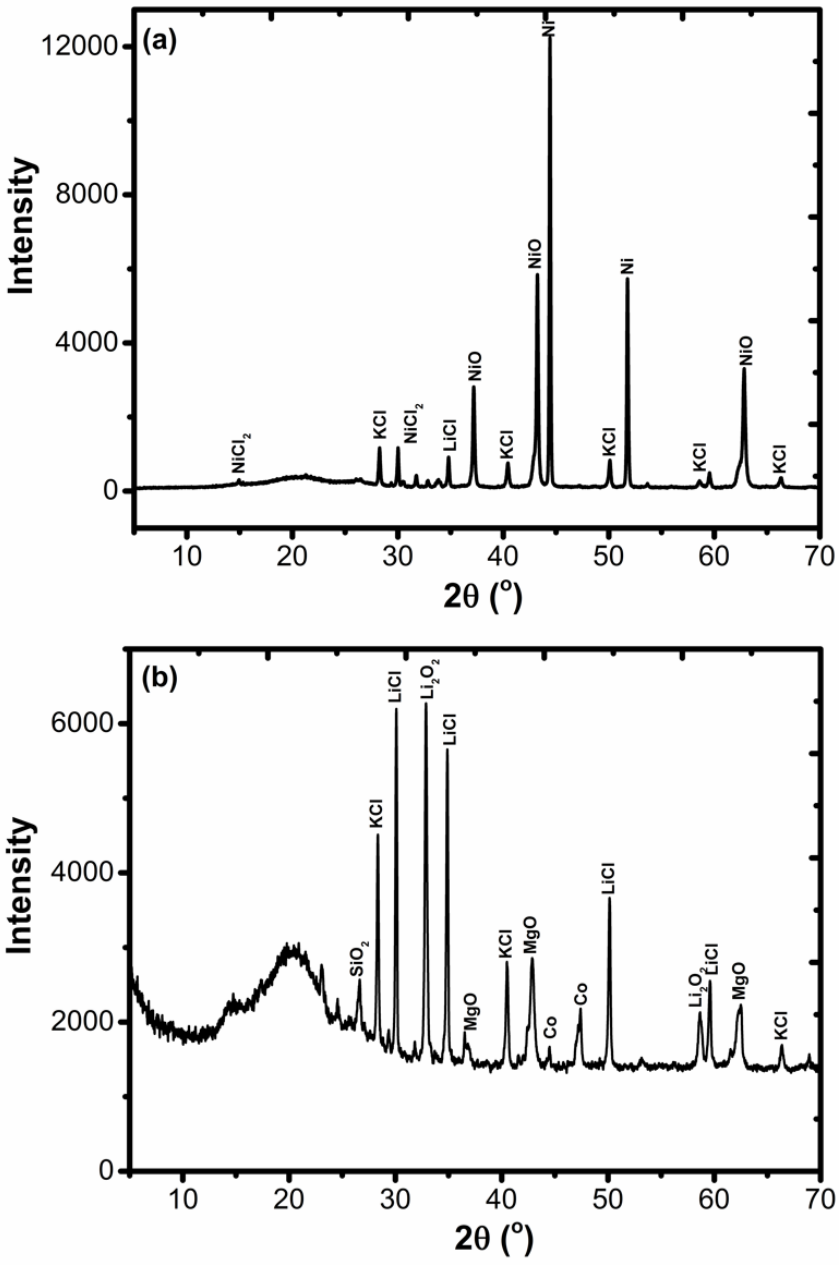

Figure 6.30. PXRD data of the cathode after galvanostatic discharge of (a) $NiCl_2$ and (b) $CoCl_2$

PXRD confirms that the product of the electrochemical reaction of $KNiCl_3$ is KCl (*a* = 6.292(3) Å), Ni metal (*a* = 3.524(7) Å) and LiCl as shown in Figure 6.29a. There are some peaks of the starting material $KNiCl_3$ (*a* = 11.805(4) Å and *c* = 5.935(12) Å) and some peaks of NiO (*a* = 4.177(4) Å).

The product of the electrochemical reaction of Li_2MnCl_4 is LiCl (*a* = 5.142(17) Å) and Mn metal *(a* = 8.948(2) Å) as shown in Figure 6.29b. There are some peaks of the electrolyte KCl and peaks of Mn_2O_3 *(a* = 9.44(5) Å, *b* = 9.55(4) Å and *c* = 9.28(3) Å) and Mn_3O_4 *(a* = 5.747(3) Å and *c* = 9.444(6) Å).

The product of the electrochemical reaction of Li_6VCl_8 is LiCl (*a* = 5.139(12) Å) and V_2O_3 (*a* = 4.944(15) and *c* = 14.020(4) Å) as shown in Figure 6.29c. Also there are peaks of KCl (*a* = 6.289(3) Å) and MgO (*a* = 4.209(12) Å) and some other peaks that were difficult to identified and indexed to the known PDF database.

The product of the electrochemical reaction of $NiCl_2$ is LiCl (*a* = 5.129(5) Å) and Ni metal (*a* = 3.524(7) Å) as shown in Figure 6.30a. There are some peaks of the starting material $NiCl_2$ (*a* = 3.468(21) Å and *c* = 17.302(7) Å), some peaks of NiO (*a* = 4.180(12) Å) and some peaks of KCl (*a* = 6.299(18) Å).

PXRD confirms that the product of the electrochemical reaction of $CoCl_2$ is LiCl (*a* = 5.142(19) Å) and Co metal (*a* = 2.50(18) Å, *c* = 4.10(26) Å) as shown in Figure 6.30b. There are some peaks of KCl (*a* = 6.300(6) Å), MgO (*a* = 4.215(10) Å), Li_2O_2 (*a* = 3.140(6) Å, *c* = 7.658(15) Å) and SiO_2 (*a* = 4.90(6) Å, *c* = 5.40(15) Å).

There is a small amount of oxide impurity in each of the diffraction patterns after discharge to a small amount of oxidation of the sample prior to and during the collection of PXRD data.

6.3 **Summary**

This chapter focuses on $NiCl_2$, $KNiCl_3$, Li_6VCl_8, Li_2MnCl_4 and $CoCl_2$ as cathode materials for use in Li thermal batteries. These materials have not been reported as cathodes until now against $Li_{13}Si_4$.

$CoCl_2$, $KNiCl_3$ and Li_2MnCl_4 do not exhibit a flat voltage plateau as there is an insertion reaction rather than a conversion reaction. Thermal batteries prefer a flat voltage plateau as they have a better voltage control during the discharge reaction.

Therefore, at low current densities, the behaviour of both Li_6VCl_8 and $NiCl_2$ is different to that of Li_2MnCl_4, $KNiCl_3$ and $CoCl_2$, as Li_6VCl_8 and $NiCl_2$ are the only materials which exhibit a flat voltage plateau in the discharge profiles.

$NiCl_2$ exhibits the highest capacity of 360 mA h g^{-1} compared to other transition metal chlorides, such as $CoCl_2$, $KNiCl_3$, Li_2MnCl_4 and Li_6VCl_8. However, $CoCl_2$ exhibits the lowest cell resistance compared to the others.

Transition metal chlorides exhibit higher voltages against $Li_{13}Si_4$ compared to transition metal disulfides, such as FeS_2, NiS_2 or CoS_2. However, these sulfides exhibit higher capacities compared to transition metal chlorides.

All the electrochemical mechanisms and the products after discharge were confirmed by PXRD data.

6.4 **References**

[1] http://www.factsage.cn/fact/documentation/ftsalt/KCl-NiCl2.jpg

[2] Belyaev I.N. *et al.*, *Journal of Inorganic Chemistry,* 15, (1970), 430-431

[3] D. Visser *et al.*, *Physica B,* 276-278, (2000), 300-301

[4] J.L. Manes *et al.*, *Physical review B*, 26, (1) (1982), 250

[5] O.A. Petrenko *et al.*, *Journal of Physics Condensed Matter,* 8, (1996), 10899–10906

[6] D. Visser *et al.*, *Acta Crystallographica,* B, 36 (1980), 28-34

[7] Ch. Wickel *et al.*, *Zeitschrift anorganische allgemeine Chemie,* 620 (1994), 1537-1542

[8] R. Kanno *et al.*, *Solid State Ionics,* 28-30 (1988), 1276-1281

[9] http://www.crct.polymtl.ca/fact/phase_diagram.php?file=LiCl MnCl2.jpg

[10] C.J.J. Van Loon *et al.*, *Acta Crystallographica,* B, 31 (1975), 2549

[11] Hanebali L. *et al.*, *Materials Research Bulletin*, 16, (1981), 887-901

[12] Wells A.F., *Structural Inorganic Chemistry*, Oxford Press, Oxford, United Kingdom, (1984)

[13] George Y. Lai, *High-Temperature Corrosion and Materials Applications,* (2007)

[14] Ferrari A. *et al.*, *Acta Crystallographica* (1, 1948 - 23, 1967), 16, (1963), 846-847

[15] Dale L. Perry, *Handbook of Inorganic Compounds, Second Edition*, CRC Press, (2011)

[16] Wilkinson M. *et al.*, *Physical Review,* (1, 1893 - 132, 1963/141, 1966-188, 1969) 113 (1959), 497-507

[17] R.C. Galloway, *Journal of the Electrochemical Society,* 134, (1) (1987), 256

Chapter 7: Transition Metal Fluoride Cathodes

Chapter 7: Transition Metal Fluoride Cathodes

7.1 Material Characterisation of Transition Metal Fluorides

7.1.1 CuF_2

CuF_2 (Alfa Aesar, 99.5%) was analysed by powder X-ray diffraction and the resulting diffraction pattern is presented in Figure 7.1. CuF_2 was identified as the main phase, but there is also a $CuF_2 \cdot 2H_2O$ impurity with cell parameters (a = 6.415(16) Å, b = 7.407(17) Å and c = 3.319(7) Å). CuF_2 crystallises in monoclinic $P2_1/c$ with cell dimensions (a = 3.302(7) Å, b = 4.563(4) Å and c = 5.354(5) Å) as shown in Figure 7.2. The monoclinic structure of CuF_2 is formed by octahedra of fluorine surrounding Cu cations and each fluorine anion is coordinated by three Cu cations [1]. The melting point of CuF_2 is 836 °C [2].

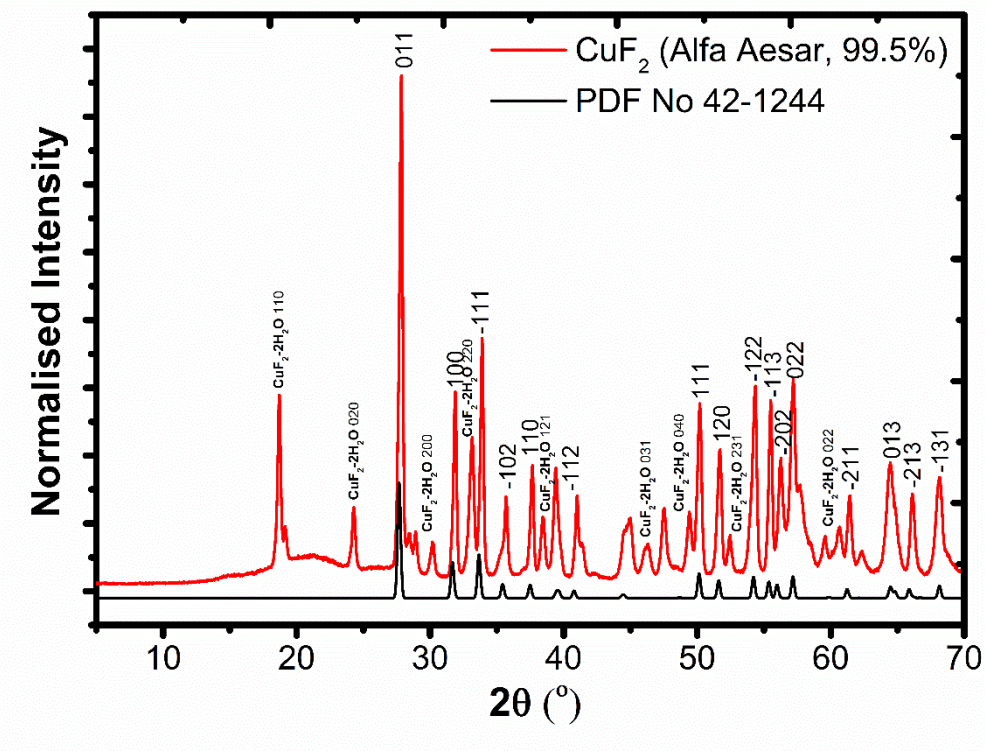

Figure 7.1. PXRD data of CuF_2 at room temperature. Experimental pattern is shown by the red line and the simulated diffraction pattern using published crystallographic model [3] is shown by the black line. Impurity is CuF_2-$2H_2O$

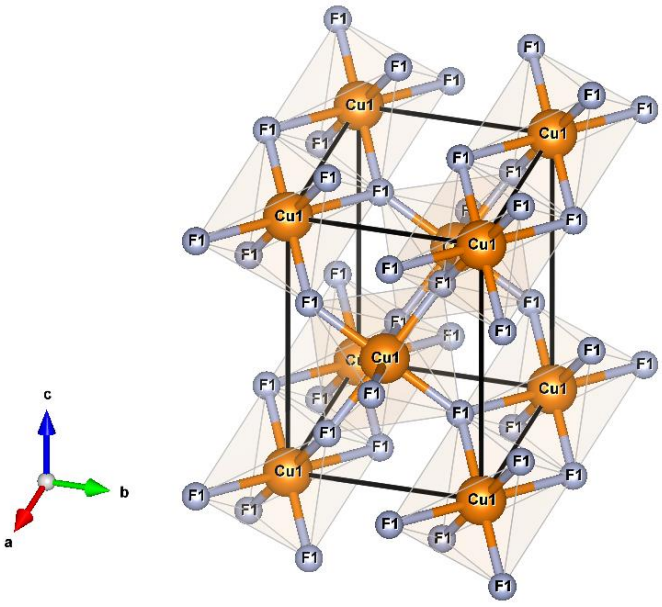

Figure 7.2. Crystal structure of CuF_2. Orange atoms are copper and grey atoms are fluorine

The SEM images of CuF_2, as shown in Figures 7.3a and 7.3b, show the size of the crystallites before and after the discharge. Crystallites are bigger than 50 μm, before testing and become smaller than 10 μm, after testing. EDX confirms Cu 42 ±2 at% and F 58 ±2 at% as expected for CuF_2 before it being tested as a cathode in a Li thermal battery as shown in Figure 7.3a. The elemental analysis of CuF_2 cathode electrode after the discharge is Cu 72 ±3 at% and F 28 ±3 at% (Figure 7.3b) and this means that different products of the electrochemical mechanism are formed, such as Cu metal and LiF. These products will be confirmed at a later stage by powder X-ray diffraction.

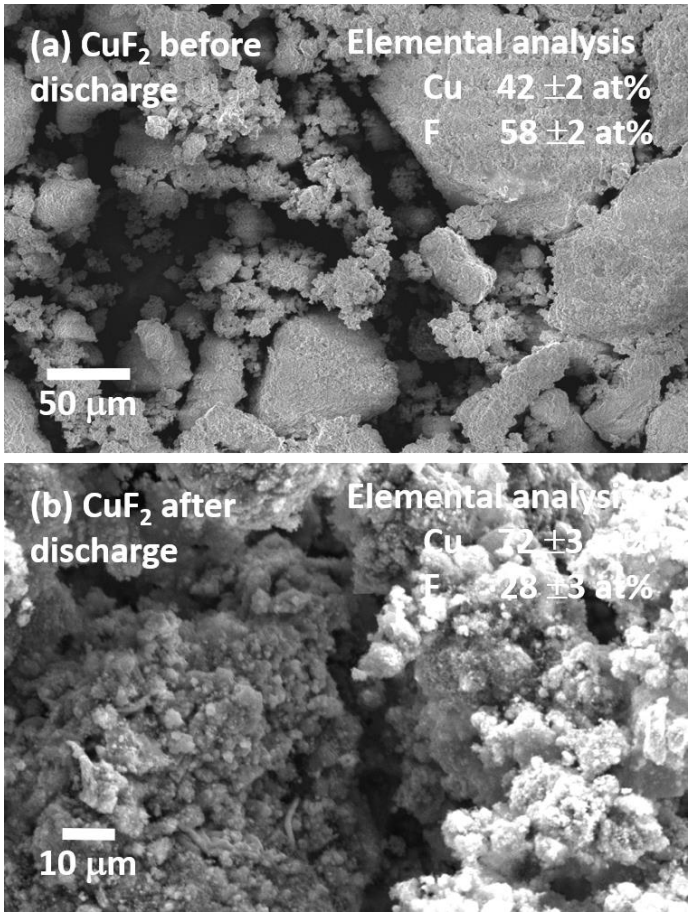

Figure 7.3. SEM images of CuF_2 before (a) and after (b) discharge

7.1.2 **PbF_2**

PbF_2 (BDH Chemicals, 99%) was analysed by powder X-ray diffraction and the diffraction pattern is shown in Figure 7.4. PbF_2 was identified as the main phase and crystallises in orthorhombic *Pmnb* with unit cell parameters (a = 3.9027(4) Å, b = 6.4468(5) Å and c = 7.6552(7) Å). This orthorhombic phase transforms to a cubic phase $Fm\bar{3}m$ with unit cell parameters (a = 5.9395(6) Å) at 337 °C [4]. This phase transformation of PbF_2 was obtained in our experiments after the electrochemical test. The orthorhombic structure of PbF_2 has twelve ions, four lead ions and eight fluorine ions as shown in Figure 7.5 [5]. The melting point of PbF_2 is 855 °C [6].

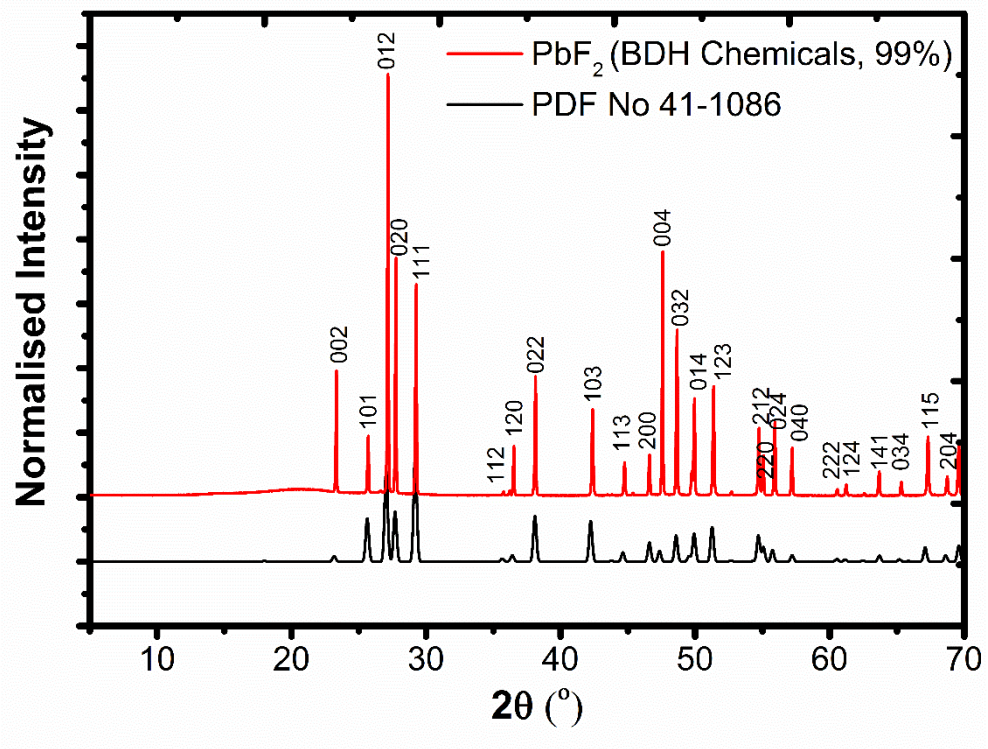

Figure 7.4. PXRD data of PbF_2 at room temperature. Experimental pattern is shown by the red line and the simulated diffraction pattern using published crystallographic model [7] is shown by the black line

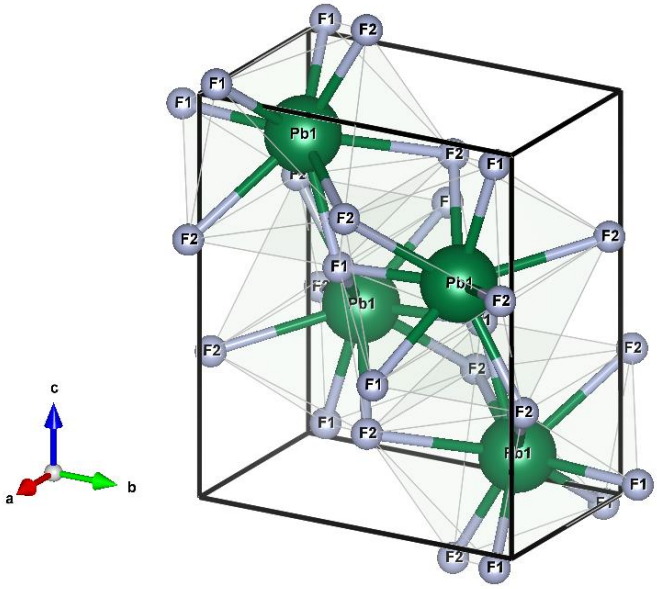

Figure 7.5. Crystal structure of PbF_2. Green atoms are lead and grey atoms are fluorine

The morphology of PbF_2 was investigated by SEM before and after discharge and images are shown in Figures 7.6a and 7.6b. The SEM images show that the morphology has been changed after the discharge and the size of the crystallites differs. EDX confirms Pb 33 ±1 at% and F 67 ±1 at% as expected for PbF_2 before being tested as a cathode in a Li thermal battery as shown in Figure 7.6a. The elemental analysis of PbF_2 cathode electrode after testing is Pb 15 ±1 at% and F 85 ±1 at% (Figure 7.6b) and this means that different products of the electrochemical mechanism are formed, such as Pb metal and LiF. Once again, these products will be confirmed at a later stage by powder X-ray diffraction.

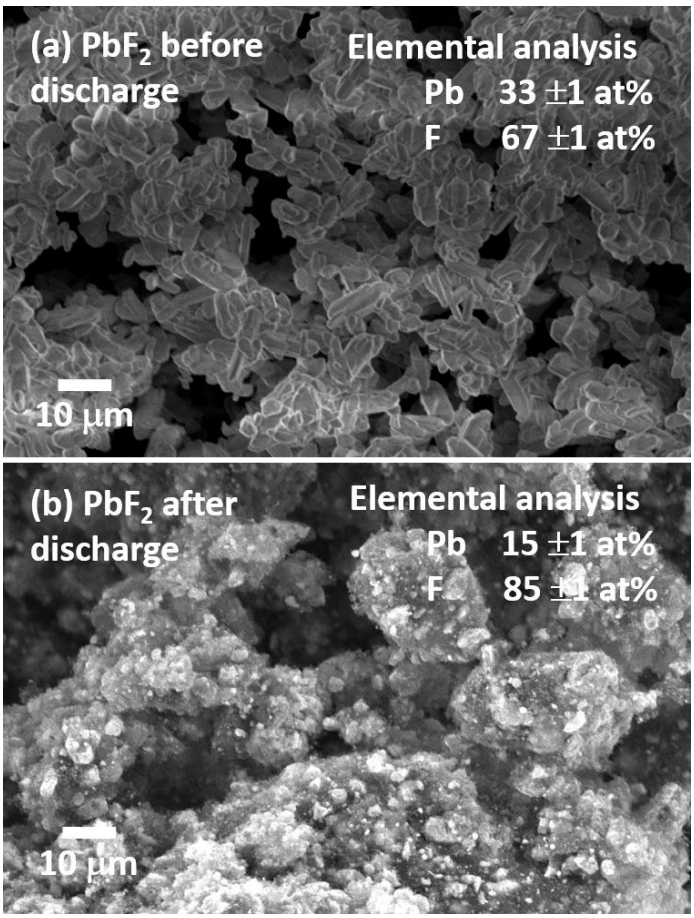

Figure 7.6. SEM images of PbF_2 before (a) and after (b) discharge

7.2 **Electrochemical Investigation of Transition Metal Fluorides**

Both transition metal fluorides were studied electrochemically by galvanostatic discharge and PbF_2 was also studied by galvanostatic intermittent titration technique.

7.2.1 **CuF_2**

Galvanostatic discharge curve for measurements carried out at 500 °C for CuF_2 is presented in Figure 7.7. Galvanostatic discharge was performed at a current density of 22 mA/cm^2 and the voltage cut-off was 0.25 V as shown in Figure 7.7. There is a high cell voltage (2.25 V) but a flat voltage plateau could not be obtained. A capacity of 120 mA h g^{-1} was measured for CuF_2 and this corresponds to a value of x = 0.5 for the number of lithium atoms transferred during the discharge process. The electrochemical mechanism was expected to be as:

$$CuF_2 + 2\ Li \Rightarrow Cu + 2\ LiF \quad [7.1]$$

The observed value of x = 0.5 does not match to the theoretical value of x = 2, because the grain size of the powder CuF_2 is in the range of microns. CuF_2 was used as a cathode material at room temperature Li ion batteries and exhibited a voltage profile of 3 V. However, the powder of CuF_2 was ball milled in different conditions [8]. Therefore, a macro-composite of CuF_2 exhibited a capacity of 100 m Ah g^{-1} [9] and this is similar to 120 m Ah g^{-1}, which was measured in our experiments.

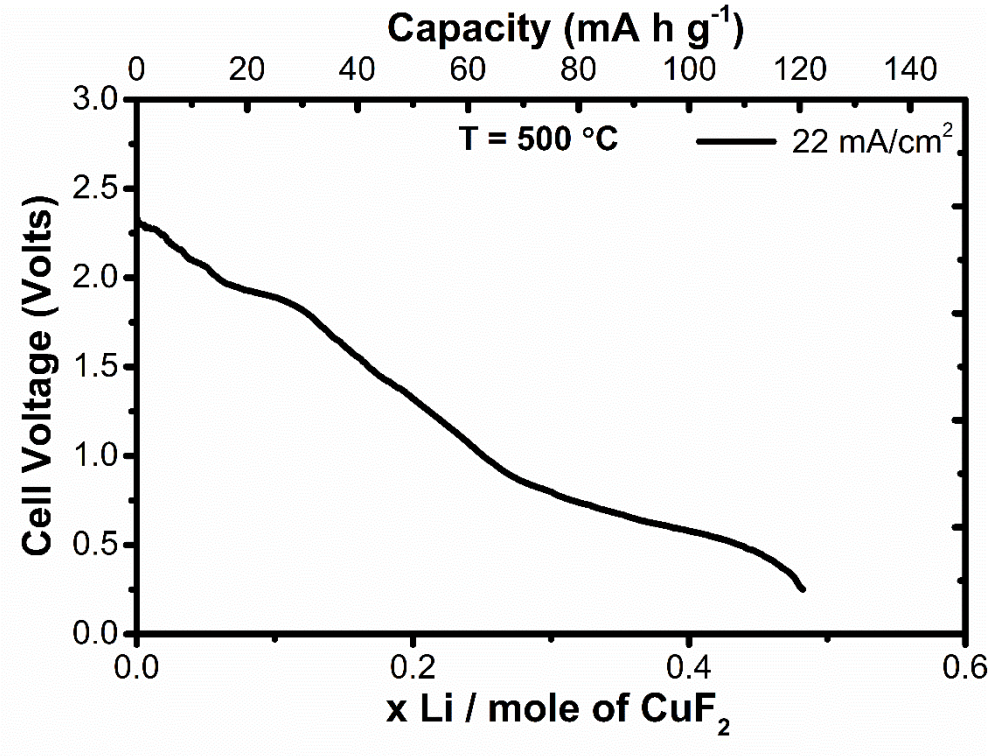

Figure 7.7. Galvanostatic discharge of CuF_2 at a current density of 22 mA/cm^2 at 500 °C

7.2.2 PbF_2

Galvanostatic discharge curves for measurements carried out at 500 °C for PbF_2 are presented in Figure 7.8. Galvanostatic discharge was performed at current densities of 15, 30 and 45 mA/cm^2. The voltage cut-off was 0.25 V as shown in Figure 7.8, and the voltage of PbF_2 drops quickly after 1 V is reached, at a current density of 15 mA/cm^2. Moreover, there is a single flat voltage plateau at 1.25 V at a current density of 15 mA/cm^2. A capacity of 260 mA h g^{-1} was achieved and this corresponds to a value of x = 2.5. At higher current densities of 30 and 45 mA/cm^2 a flat voltage plateau could not be obtained due to the decomposition of PbF_2. Capacities of 245 mA h g^{-1} and 219 mA h g^{-1} were measured at current densities of 30 and 45 mA/cm^2, respectively. The electrochemical mechanism corresponds to:

$PbF_2 + 2\ Li \Rightarrow Pb + 2\ LiF$ [7.2]

PbF_2 was used as an electrolyte in thin film solid state galvanic cells [10]. PbF_2 was also tested as a cathode material at room temperature in Li ion batteries. The electrochemical reaction of PbF_2 was completed in two steps between 2.4 and 1.5 V against Li metal. The product of the discharge mechanism was 2LiF per formula unit and this corresponded to 360 mA h g^{-1} [11]. We suggest that PbF_2 exhibits different electrochemical behaviour at high temperature batteries as the observed value of x = 2.5 does not match to the theoretical value of x = 2. However, the single plateau of 1.25 V appears from value of x = 0.5 to value of x = 2.5 and this range corresponds to value of x = 2.0 as expected.

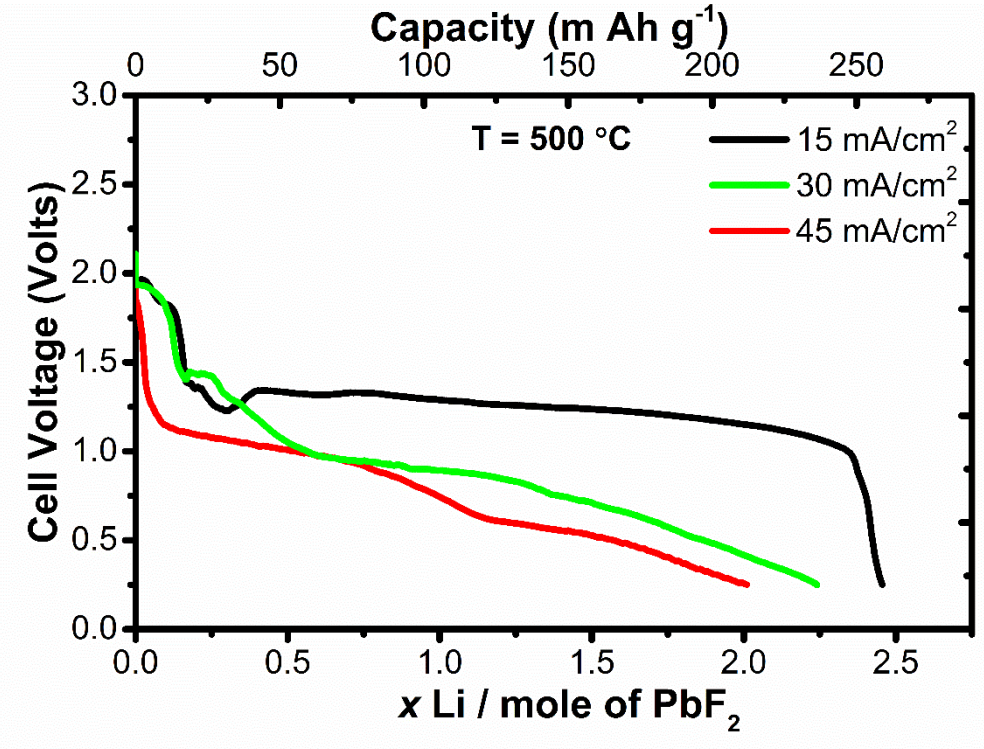

Figure 7.8. Galvanostatic discharge of PbF_2 at current densities of 15, 30 and 45 mA/cm^2 at 500 °C

The galvanostatic intermittent titration technique measurement (GITT) of PbF_2 at 500 °C is shown in Figure 7.9. The IR drop is 100 mV at the beginning of discharge and 160 mV at the end of the measurement, which indicates that the cell resistance is increasing during the reduction of the cathode, from a resistance of 13 Ω at the beginning of the measurement to 21 Ω after the cell discharge. A single voltage plateau at 1.25 V at a current density of 7.5 mA/cm^2 is also obtained.

The chemical diffusion coefficient D = 1.05 10^{-8} cm^2 s^{-1} for PbF_2 can be calculated from equation [3.1] where n_m = 0.000815 (mol), V_m = 29.01 (cm^3 / mol), ΔE_s = 0.050 (V) and ΔE_t = 0.400 (V).

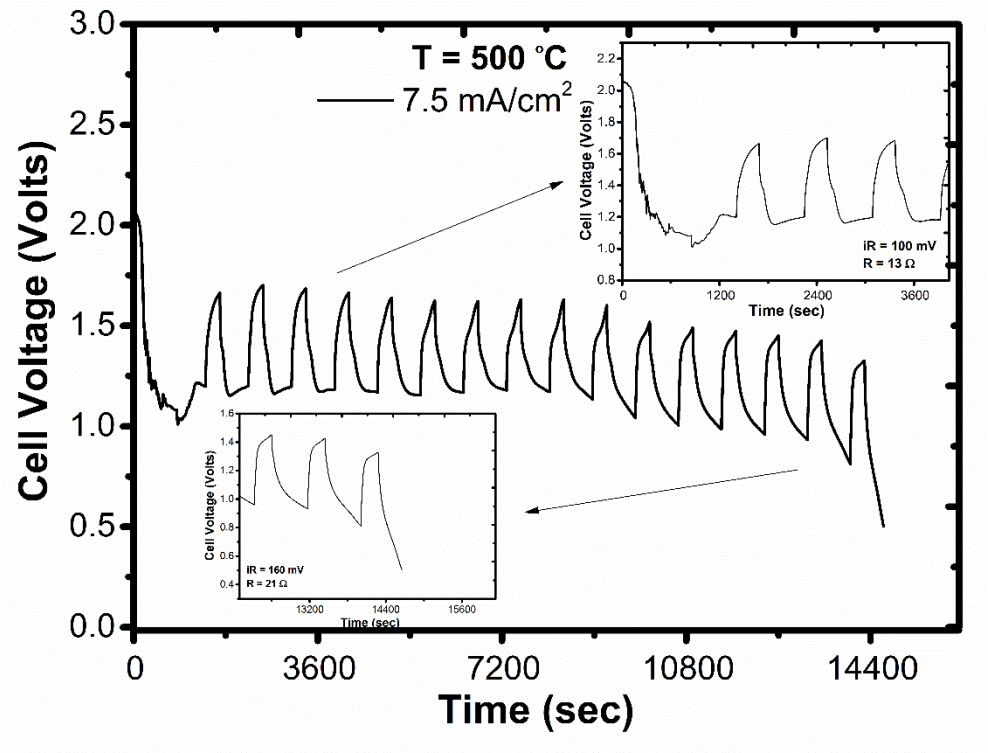

Figure 7.9. Galvanostatic intermittent titration technique of PbF_2 at a current density of 7.5 mA/cm^2 at 500 °C

PXRD data were collected after discharge for both of the cathodes as shown in Figure 7.10.

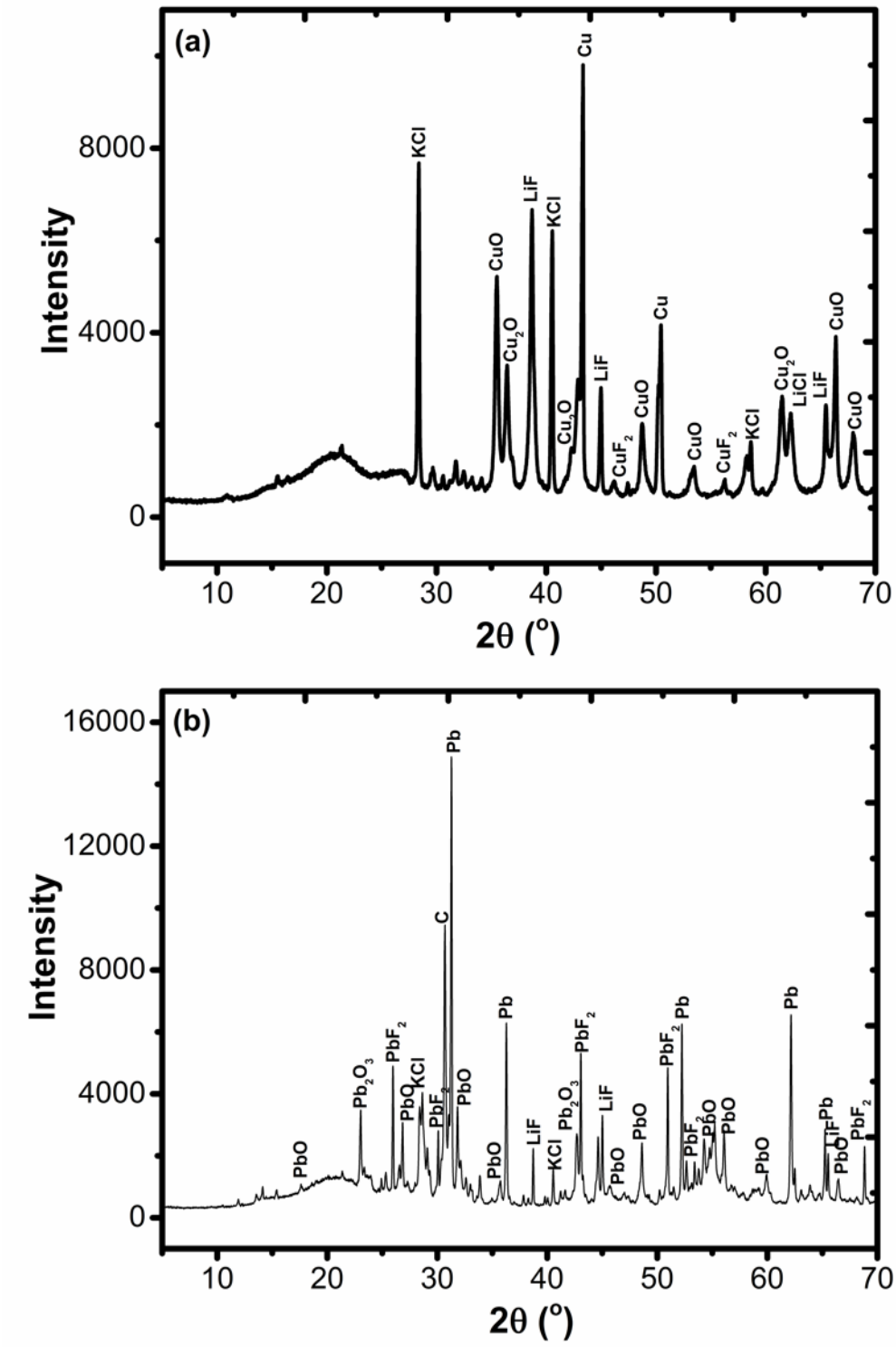

Figure 7.10. PXRD data of the cathode after galvanostatic discharge of (a) CuF_2 and (b) PbF_2

PXRD data confirm that the product of the electrochemical reaction of CuF_2 is Cu metal (a = 3.60(6) Å) and LiF (a = 3.99(23) Å) as shown in Figure 7.10a. There are some peaks of copper oxides, such as CuO and Cu_2O and some peaks of KCl. The present amount of KCl causes low capacity of the cathode PbF_2 compared to the expected as we suggest that PbF_2 dissolves into KCl.

The product of the electrochemical reaction of PbF_2 is Pb metal (a = 4.951(19) Å) and LiF (a = 4.025(6) Å) as shown in Figure 7.10b. There are some peaks of the electrolyte KCl and some peaks of lead oxides, such as PbO and Pb_2O_3.

There is a small amount of oxide impurity in each of the diffraction patterns after discharge to a small amount of oxidation of the sample prior to and during the collection of PXRD data.

7.3 **Summary**

This chapter focuses on CuF_2 and PbF_2 as cathode materials for use in Li thermal batteries. These materials have not been reported as cathodes against $Li_{13}Si_4$ until now.

CuF_2 does not exhibit a single flat voltage plateau compared to that of PbF_2 which exhibits a single flat voltage plateau at 1.25 V. This single plateau of PbF_2 exists only at low current densities of 7.5 and 15 mA/cm^2.

These electrochemical properties (low capacity and low voltage) of CuF_2 and PbF_2 are not suitable for lithium thermal battery applications. This is due to the fact that thermal batteries require as cathodes materials with high voltage and high capacity.

7.4 **References**

[1] Y. Zheng *et al.*, *Solid State Communications*, 152, (2012), 1703-1706

[2] Dale L. Perry, *Handbook of Inorganic Compounds*, CRC press, (1995)

[3] Fischer P. *et al.*, *Journal of Physics and Chemistry Solids*, 35, (1974), 1683-1689

[4] Henry E. *et al.*, *Solid State Physics*, 38, Academic press, (1984)

[5] A.V. Bazhenov *et al.*, *Physics of the Solid State*, 42, (1) (2000), 41–50

[6] C.C. Sorrell *et al.*, *Materials for Energy Conversion Devices*, CRC press, (2005)

[7] Bystroem A. *et al.*, *Mineralogi och Geologi A*, 24, (3) (1947), 1-18

[8] Xiao Hua *et al.*, *Journal of Physical Chemistry C*, 118, (28) (2014), 15169-15184

[9] F. Badway *et al.*, *Chemistry of Materials,* 19, (2007), 4129-4141

[10] John H. Kennedy *et al.*, *Journal of the Electrochemical Society,* 123, (1) (1976), 10-14

[11] L.L Garza Tovar *et al.*, *Journal of Power Sources*, 97-98, (2001), 258-261

Chapter 8: General Conclusions

Chapter 8: General Conclusions

8.1 General Conclusions

In this work, ten novel materials ($CoNi_2S_4$, $NiCo_2S_4$, ZrS_3, $NiCl_2$, $CoCl_2$, $KNiCl_3$, Li_2MnCl_4, Li_6VCl_8, CuF_2 and PbF_2) were studied and tested as cathodes for use in Li thermal batteries.

$CoNi_2S_4$ was synthesized by an improved and shorter solid state reaction with a pure phase being synthesized at 550 °C in just two firing steps. The structure was probed by powder X-ray diffraction, while the Co^{2+}/Ni^{3+} cation order and thermal stability of $CoNi_2S_4$ were studied using powder neutron diffraction. SEM showed the morphology and the shape of crystallites of $CoNi_2S_4$ around 5 μm and EDX confirmed the elemental composition as the expected.

The high temperature electrochemical performance of $CoNi_2S_4$ was characterised by galvanostatic discharge and galvanostatic intermittent titration technique (GITT). At a temperature of 500 °C, the value of the working voltage plateau was recorded at different current densities from 15 to 60 mA/cm^2 and a capacity of 350 mA h g^{-1} was achieved. A voltage value of 1.75 V [x = 4/3 Li] and of 1.50 V [x = 8/3 Li] vs $Li_{13}Si_4$ for $CoNi_2S_4$ was found at 500 °C. GITT showed an increase in the cell resistance from 13 Ω to 23 Ω during the reduction of the cathode electrode.

This material could be a promising candidate for Li thermal battery applications as it exhibits a similar behaviour to the most commonly used sulfides FeS_2, NiS_2 or CoS_2.

$NiCo_2S_4$ was synthesised by a solid state reaction with a small amount of impurity Co_9S_8 at 550 °C in just two firing steps. The structure was studied by powder X-ray diffraction. SEM showed the morphology and the shape of crystallites of $NiCo_2S_4$ ranges 1 to 10 μm and EDX confirmed the elemental composition as the expected.

The high temperature electrochemical performance of $NiCo_2S_4$ was characterised by galvanostatic discharge and galvanostatic intermittent titration technique (GITT). At a temperature of 500 °C, the value of the working voltage plateau was recorded at

different current densities from 7.5 to 60 mA/cm^2 and a capacity of 290 mA h g^{-1} was achieved. A voltage value of 1.70 V [x = 2/3 Li] and of 1.50 V [x = 8/3 Li] vs $Li_{13}Si_4$ for $NiCo_2S_4$ was obtained at 500 °C. GITT showed an increase in the cell resistance from 13 Ω to 20 Ω during the reduction of the cathode electrode. This material has a lower voltage and a less capacity compared to $CoNi_2S_4$. The products of the discharge mechanism of both $CoNi_2S_4$ and $NiCo_2S_4$ were NiS, Co_3S_4 and Co_9S_8.

Zirconium trisulfide (ZrS_3) was synthesised as a pure phase by a shorter solid state reaction in sealed quartz tube at 730 °C. The structure of the sample was studied by powder X-ray diffraction, the morphology was studied by SEM and the crystals of ZrS_3 are shaped needles.

The high temperature discharge behaviour of ZrS_3 at 500 °C was investigated by galvanostatic discharge and galvanostatic intermittent titration technique (GITT). The value of the working voltage plateau was measured for different current densities of 7.5, 11, 15, 19, 23 and 75 mA/cm^2. The GITT method showed that the cell resistance increased during the discharge from 6 Ω to 16 Ω.

A new cubic phase $LiZr_2S_4$ was found after discharge with cell parameter a = 10.452(8) Å and EDX confirmed the elemental composition.

The value of the single voltage plateau at 1.70 V with a capacity of 357 mA h g^{-1} can define ZrS_3 as a promising candidate material for Li thermal batteries.

$KNiCl_3$ was synthesised by a solid state reaction in sealed quartz tube at 675 °C for 1 week. It was found a small amount of impurity KCl as the starting material. The structure was probed by powder X-ray diffraction and the morphology was studied by SEM. EDX confirmed the elemental composition as was expected.

$KNiCl_3$ exhibits a high cell voltage 2.30 V at 425 °C vs $Li_{13}Si_4$ but not a flat voltage profile and a capacity of 262 mA h g^{-1} was achieved. The products of the discharge mechanism were Ni metal, KCl and LiCl. The cell resistance was increased from 15 Ω at the beginning of the measurement to 26 Ω after the cell discharge.

Li_2MnCl_4 was synthesised at 600 °C for 1 week but not as a pure phase. LiCl impurity was found as a starting material. Li_2MnCl_4 was tested at 400 °C and a capacity of 254 mA h g^{-1} was achieved. The cell resistance was measured at 13 Ω at the beginning of the

discharge to 66 Ω at the end of the discharge. Mn metal and LiCl were formed after the cell discharge.

Li_6VCl_8 was synthesised at 800 °C for 1 week with a small amount of impurity V_2O_3. A flat voltage plateau of 1.80 V at a current density of 7.5 mA/cm^2 with capacity of 145 mA h g^{-1} was obtained. The cell resistance increased from 6 Ω to 33 Ω at the end of the measurement.

$NiCl_2$ was tested as a commercial compound at 500 °C and a high voltage profile of 2.25 V at a current density of 22 mA/cm^2 with capacity of 360 mA h g^{-1} was obtained. Ni metal and LiCl were formed at the end of discharge. Cell resistance of 13 Ω at the beginning and 33 Ω at the end of discharge was obtained.

$CoCl_2$ was tested as a commercial compound at 500 °C and a lower voltage profile compared to $NiCl_2$ was obtained. Co metal and LiCl were formed at the end of discharge as expected. The cell resistance of 6 Ω at the beginning of the discharge to 26 Ω at the end, characterises Co as more conductive than Ni.

CuF_2 was tested as a commercial compound at 500 °C but decomposed quickly to Cu metal and LiF at a current density of 22 mA/cm^2 and a capacity of 120 mA h g^{-1} was obtained.

PbF_2 was tested as a commercial compound at 500 °C and a single voltage plateau at 1.25 V at a current density of 15 mA/cm^2 with capacity of 260 mA h g^{-1} was obtained. Pb metal and LiF were formed as expected. The cell resistance was 13 Ω at the beginning of the measurement and 21 Ω at the end of discharge. However, PbF_2 seems to be more stable than CuF_2.

Clearly a full understanding of all the chemical compositions and crystalline phases that are presented in post electrochemical testing is extremely important as it can lead to the discovery of new crystalline phases, whilst also providing an insight into the electrochemical processes occurring during discharge.

Finally, Table 8.1 shows the comparison between the novel cathodes and the well-known transition metal disulfides.

Table 8.1. Thermal stability, overall capacity, voltages vs $Li_{13}Si_4$, and discharge products of Novel Cathodes compared to that of transition metal disulfides FeS_2, CoS_2 and NiS_2

Materials	**Thermal stability (°C)**	**Capacity (mA h g^{-1})**	**Voltages (V) vs $Li_{13}Si_4$**	**Discharge Products**
FeS_2	550 [1, 2]	558 [3]	1.77, 1.64, 1.13 [4]	Fe and Li_2S [4]
CoS_2	650 [5]	598 [3]	1.75, 1.40, 1.25 [4]	Co and Li_2S [4]
NiS_2	600 [6]	545 [3]	1.76, 1.60, 1.40, 1.25 [4]	Ni and Li_2S [4]
ZrS_3	700 [7]	357 [7]	1.70 [7]	$LiZr_2S_4$ [7]
$CoNi_2S_4$	550 [8]	350 [8]	1.75, 1.50 [8]	Co_3S_4, NiS and Co_9S_8 [8]
$NiCo_2S_4$	550	290	1.70, 1.50	Co_3S_4, NiS and Co_9S_8
$KNiCl_3$	675	262	2.30	Ni, KCl and LiCl
$NiCl_2$	500	360	2.25	Ni and LiCl
$CoCl_2$	500	330	2.00	Co and LiCl
Li_2MnCl_4	600	254	2.50	Mn and LiCl
Li_6VCl_8	800	145	1.80	V and LiCl
PbF_2	500	260	1.25	Pb and LiF
CuF_2	500	120	2.25	Cu and LiF

8.2 **References**

[1] M.C. Hash *et al.*, *Proceedings of the 8th International Symposium on Molten Salts*, 228, (1992)

[2] I.C. Hoare *et al.*, *Journal of Chemical Society Faraday Transactions*, 184, (9) (1988), 3071

[3] S.K. Preto *et al.*, *Journal of the Electrochemical Society*, 130, (1983), 264

[4] Patrick J.M. *et al.*, *Journal of Power Sources,* 178, (2008), 456

[5] H. Rau, *Journal of Physics and Chemistry Solids*, 37, (1976), 931

[6] R.A. Guidotti *et al.*, *Proceedings of the 40th Power Sources Conference*, 250, (2002)

[7] Kyriakos Giagloglou *et al., Journal of the Electrochemical Society*, 163, (14) (2016), A3126-A3130

[8] Kyriakos Giagloglou *et al.*, *Journal of the Electrochemical Society,* 164, (9) (2017), A1-A5